



Universitat Autònoma de Barcelona

**ADVERTIMENT.** L'accés als continguts d'aquesta tesi doctoral i la seva utilització ha de respectar els drets de la persona autora. Pot ser utilitzada per a consulta o estudi personal, així com en activitats o materials d'investigació i docència en els termes establerts a l'art. 32 del Text Refós de la Llei de Propietat Intel·lectual (RDL 1/1996). Per altres utilitzacions es requereix l'autorització prèvia i expressa de la persona autora. En qualsevol cas, en la utilització dels seus continguts caldrà indicar de forma clara el nom i cognoms de la persona autora i el títol de la tesi doctoral. No s'autoritza la seva reproducció o altres formes d'explotació efectuades amb finalitats de lucre ni la seva comunicació pública des d'un lloc aliè al servei TDX. Tampoc s'autoritza la presentació del seu contingut en una finestra o marc aliè a TDX (framing). Aquesta reserva de drets afecta tant als continguts de la tesi com als seus resums i índexs.

**ADVERTENCIA.** El acceso a los contenidos de esta tesis doctoral y su utilización debe respetar los derechos de la persona autora. Puede ser utilizada para consulta o estudio personal, así como en actividades o materiales de investigación y docencia en los términos establecidos en el art. 32 del Texto Refundido de la Ley de Propiedad Intelectual (RDL 1/1996). Para otros usos se requiere la autorización previa y expresa de la persona autora. En cualquier caso, en la utilización de sus contenidos se deberá indicar de forma clara el nombre y apellidos de la persona autora y el título de la tesis doctoral. No se autoriza su reproducción u otras formas de explotación efectuadas con fines lucrativos ni su comunicación pública desde un sitio ajeno al servicio TDR. Tampoco se autoriza la presentación de su contenido en una ventana o marco ajeno a TDR (framing). Esta reserva de derechos afecta tanto al contenido de la tesis como a sus resúmenes e índices.

**WARNING.** The access to the contents of this doctoral thesis and its use must respect the rights of the author. It can be used for reference or private study, as well as research and learning activities or materials in the terms established by the 32nd article of the Spanish Consolidated Copyright Act (RDL 1/1996). Express and previous authorization of the author is required for any other uses. In any case, when using its content, full name of the author and title of the thesis must be clearly indicated. Reproduction or other forms of for profit use or public communication from outside TDX service is not allowed. Presentation of its content in a window or frame external to TDX (framing) is not authorized either. These rights affect both the content of the thesis and its abstracts and indexes.



**Universitat Autònoma de Barcelona**

**Facultat de Biociències**

Departament de Bioquímica i Biologia Molecular

**PROTEOMIC QUANTITATIVE STUDY OF  
DORSAL ROOT GANGLIA AND SCIATIC  
NERVE IN TYPE 2 DIABETIC MICE**

**Marc Leal Julià**

**ACADEMIC DISSERTATION**

To obtain the Degree of PhD in Neurosciences by  
the Universitat Autònoma de Barcelona

Directed by:

Assumpció Bosch Merino

Tutored by:

Xavier Navarro Acebes

Bellaterra, 2022



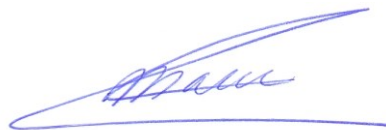
The research described in this thesis was conducted at the Department of Biochemistry and Molecular Biology and Institute of Neurosciences (INc), at the Universitat Autònoma de Barcelona (UAB) in the Group of Gene therapy for Neurometabolic Disorders, directed by Dr. Assumpció Bosch i Merino.

All the studies were financially supported by the FI-AGAUR fellowship (2019FI\_B2 00061) and the Fundació Marató TV3 grant (201607.10).



Supervisor:

ASSUMPCIÓ BOSCH MERINO



PhD candidate:

MARC LEAL JULIÀ







## AGRAÏMENTS

Estic acabant d'escriure la tesi i encara no acabo de processar haver arribat al final d'una etapa que fa uns anys veia lluny, molt lluny, gairebé impossible. Si soc sincer, sempre he estat una persona una mica insegura que no sabia gestionar ni els errors ni els fracassos i bé, és evident que aquest camí anava a estar ple de tot això. Així doncs, que millor que començar els agraïments, reconeixent el que ha fet el doctorat per mi, ja no com a científic sinó com a persona. Potser molts dirien que el canvi és subtil i, de fet, encara he de treballar molt per prendre'm la vida de forma més tranquil·la, però bé, aquesta etapa sense dubte ha contribuït a que tingui més paciència i saber gestionar que les coses no surtin a la primera (ni a la segona, etc.), sempre buscar alternatives i tornar més fort.

Vull agrair a la Dra. Assumpció Bosch per haver confiat en mi en tot moment i a motivar-me quan les coses no sortien durant tots aquests anys. Al Dr. Miguel Chillón per sempre estar disposat a ajudar-me en els conceptes més abstractes i matemàtics i per anar aportant el seu gra de sorra en els lab meetings. Evidentment un especial agraïment al Dr. Xavier Navarro, sense el qual aquesta tesi no hagués estat possible, per haver-me ajudat enormement a nivell científic i tècnic, i per haver-me motivat, a la seva peculiar manera, a llegir més, pensar més críticament i ser millor científic.

A tots els companys del CBATEG i en especial al laboratori d'en Jesús Ruberte on hi treballa gent estupenda sempre disposada a ajudar. A tot el laboratori de la 5a planta, a les cares velles i a les noves incorporacions. A la Txell i el Javi per la seva inestimable ajuda en tot el que fes falta.

A les ànimes d'UPV, al Jose, la Cristina i la Susana, gent magnífica, treballadora i incombustible. Un referent de dedicació màxima i estima pel que fan. Al Jose agrair-li que les hores de cultiu en el P2 fossin molt millors a ritme de rock. A la Cristina per les tardes de xerrada i cotilleos. I a la vitalitat i esforç de la Susana perquè sense ella la 5a planta no seria igual.

A les noves cares d'UPV, i en especial a la Laia, la meva compi d'ordinador dels últims anys que va prendre el rol oficial de comunicadora de salseo, tant necessari a les tardes avorrides davant l'ordinador. Malgrat la teva gran habilitat per posar-me dels nervis a vegades, gràcies per sempre tenir un somriure a la cara i irradiar felicitat.

A la xarreta del Joan, i al seu vocabulari a vegades castellanenc a vegades inventat que han ocupat el 50% de les converses d'aquest laboratori. Fora bromes, gràcies pel teu bon humor, els piques i el teu esperit crític i constructiu.

A l'Ángela per ser la nostre postdoc, per ajudar-nos en tot el que necessitàvem i formar-nos com a científics.

Al Sergi per ser un exemple de perseverança al que segur li espera una gran carrera científica. Trobaré a faltar les nostres xerrades que s'allargaven fins la vesprada. Gràcies perquè amb les teves reflexions de segur he pogut treure molt més suc als meus resultats.

A l'Andrea, amb qui he compartit llargues, però llargues hores fent bolos d'intratecals com a bons surgeons professionals que som. Gràcies per les fotos de gatets pel matí, les xerrades d'esport i les poses ultrarares de ioga que ens donava per practicar al laboratori entre experiment i experiment. També gràcies per haver-me

descobert l'escalada i per haver promogut que fem una activitat tots junts fora del laboratori. Així serà molt més fàcil que us pugui continuar veient les cares!

Gràcies a tots vosaltres per no només ser companys de feina, sinó amics amb els que he pogut gaudir aquesta etapa sovint tant dura. Heu estat tot el suport que necessitava.

Als meus amics del Prat, per compartir amb mi la passió de volar baix, per tocar música junts i fer-me oblidar dels problemes de la setmana. Heu estat vitals en la meva vida tots aquests anys i, per mi, sou família.

Als meus pares, el meu model de tot el que es pot aconseguir si treballes dur. Gràcies per tot el suport i l'estima incondicional que m'heu donat i que ha fet possible arribar on he arribat. A la meva germana, l'artista de la família amb un talent innat, gràcies de tot cor per sempre intentar que sigui més feliç amb mi mateix, que gaudeixi més de la vida i estar al meu costat quan no he pogut més.

Per descomptat a la meva companya d'equip, la Laia, amb qui he compartit gairebé 10 anys de vivències, amb qui he après a ser millor persona i amb qui he format un projecte comú perfecte. Gràcies per aguantar-me, que no sempre és fàcil, per escoltar-me i per motivar-me a acabar sempre que deia que volia desistir. No podria imaginar-me un millor escenari que acabar el doctorat a la vegada i iniciar, junts, els nous reptes i projectes que ens esperen ara.



# ***CONTENTS***



<b>ABBREVIATIONS</b>	<b>1</b>
<b>INTRODUCTION</b>	<b>5</b>
1. Diabetes	7
1.1. Type 2 diabetes	10
2. Diabetic neuropathy	15
2.1. Structure and function of the peripheral nervous system	15
2.1.1. Neural control of sweat secretion	24
2.2. Somatic nervous system and diabetes	26
2.3. Sudomotor function and diabetes	28
2.4. Classification of diabetic neuropathy	28
2.5. Diabetic neuropathy pathophysiology	30
2.5.1. Oxidative stress	30
2.5.2. Polyol pathway	32
2.5.3. Advanced glycation end products	33
2.5.4. Hexosamine pathway	33
2.5.5. ROS-mediated modification of biomolecules	34
2.5.6. Oxidative metabolism under diabetic conditions	35
2.5.7. Role of dyslipidaemia in diabetic neuropathy	36
2.5.8. Role of mitochondria and endoplasmic reticulum	38
2.5.9. Insulin and IGF-1 resistance	40
2.6. Animal models of diabetic neuropathy	41
2.7. Current treatments of diabetic neuropathy	44
3. Gene therapy	46
3.1. Adeno-associated viral vectors	47



3.2. Gene therapy approaches targeting PNS	51
3.2.1. Gene therapy for diabetic neuropathy	52
<b>OBJECTIVES</b>	<b>53</b>
<b>RESULTS</b>	<b>57</b>
1. Metabolic profile of BKS- <i>Lepr<sup>db/db</sup></i> mice	59
2. Neuropathy evaluation in BKS- <i>Lepr<sup>db/db</sup></i> mice	61
3. Analysis of DRG and sciatic nerve proteome	71
4. <i>In vitro</i> and <i>in vivo</i> study of MUP function in PNS	103
5. AAV9-KI as a therapeutic approach for DN	108
<b>DISCUSSION</b>	<b>117</b>
<b>CONCLUSIONS</b>	<b>133</b>
<b>MATERIALS AND METHODS</b>	<b>137</b>
1. <i>In vitro</i> cell culture	139
1.1. Cell lines	139
1.2. Cell transfection	140
1.3. Oxidative stress assay	140
1.4. MTT assay	141
1.5. Preparation of BSA-conjugated palmitate	141
2. Cloning	142
2.1. <i>Mup</i> cloning	142
2.2. shRNA design and cloning	143
3. Viral vectors production	143
4. Animal procedures	145
4.1. Murine models	145

4.2. Surgical procedures	146
4.2.1. Anaesthesia and euthanasia	146
4.2.2. Intrathecal administration	147
4.3. Functional evaluation	148
4.3.1. Electrophysiological testing	148
4.3.2. Sweating test	149
5. Histological analysis	150
5.1. Morphometry of tibial nerve	150
5.2. Immunohistochemistry	151
5.2.1. DRG and SCN	151
5.2.2. Cutaneous innervation	151
6. Molecular techniques	153
6.1. TMT-LC/MS/MS and bioinformatics analysis	153
6.2. Real-Time PCR	154
6.3. <i>Xbp1</i> alternative splicing	155
6.4. Western blot	155
7. Statistical analysis	157
<b>REFERENCES</b>	<b>159</b>
<b>ANNEX</b>	<b>191</b>



# ***ABBREVIATIONS***



<b>AAV</b>	Adeno-associated virus
<b>AGEs</b>	Advanced glycation end products
<b>BMI</b>	Body mass index
<b>bp</b>	Base pairs
<b>BSA</b>	Bovine serum albumin
<b>CAG</b>	Synthetic promoter (CMV enhancer, chicken $\beta$ -actin promoter, and rabbit $\beta$ -globin splice acceptor)
<b>CMAP</b>	Compound muscle action potential
<b>CMV</b>	Cytomegalovirus promoter
<b>CNAP</b>	Compound nerve action potential
<b>CNS</b>	Central nervous system
<b>CSF</b>	Cerebrospinal fluid
<b>DCFDA</b>	2',7' -dichlorofluorescein diacetate
<b>DIO</b>	Diet-induced obesity
<b>DM</b>	Diabetes mellitus
<b>DMEM</b>	Dulbecco's Modified Eagle Medium
<b>DN</b>	Diabetic neuropathy
<b>DRG</b>	Dorsal root ganglia
<b>dsDNA</b>	Double-stranded DNA
<b>ER</b>	Endoplasmic reticulum
<b>FBS</b>	Fetal bovine serum
<b>FFA</b>	Free fatty acids
<b>Fwd</b>	Forward primer
<b>GFP</b>	Green fluorescent protein
<b>GlcNac</b>	Uridine 5-diphosphate-N-acetylglucosamine
<b>GO</b>	Gene Ontology database
<b>Hba1c</b>	Glycated haemoglobin
<b>HFD</b>	High-fat diet
<b>HRP</b>	Horseradish peroxidase
<b>IDF</b>	International Diabetes Federation
<b>IENFD</b>	Intraepidermal nerve fibre density

<b>IGF-1</b>	Insulin-like growth factor 1
<b>ITR</b>	Inverted terminal repeats
<b>MDA</b>	Malondialdehyde
<b>MNCV</b>	Motor nerve conduction velocity
<b>MTT</b>	Methylthiazolyldiphenyl-tetrazolium bromide
<b>NCV</b>	Nerve conduction velocity
<b>P/S</b>	Penicillin-streptomycin
<b>PBS</b>	Phosphate-buffered saline
<b>PCR</b>	Polymerase chain reaction
<b>PEG</b>	Polyethylene glycol
<b>PEI</b>	Polyethyleneimine
<b>PFA</b>	Paraformaldehyde
<b>PNS</b>	Peripheral nervous system
<b>qPCR</b>	Quantitative polymerase chain reaction
<b>RAGE</b>	Receptor for advanced glycation end products
<b>ROS/RNS</b>	Reactive oxygen/ nitrogen species
<b>Rv</b>	Reverse primer
<b>SCN</b>	Sciatic nerve
<b>shRNA</b>	Short hairpin RNA
<b>SNCVd</b>	Distal sensory nerve conduction velocity
<b>ssDNA</b>	Single-stranded DNA
<b>STZ</b>	Streptozotocin
<b>sWAT</b>	Subcutaneous white adipose tissue
<b>T2DM</b>	Type 2 diabetes mellitus
<b>tBHP</b>	tert-Butyl hydroperoxide
<b>TBS-T</b>	Tris-buffered saline with tween-20
<b>TCA</b>	Tricarboxylic acid cycle
<b>UPR</b>	Unfolded protein response
<b><i>uXbp1/sXbp1</i></b>	Unspliced/ spliced <i>Xbp1</i>
<b>wt</b>	Wild-type

# ***INTRODUCTION***





## 1. DIABETES

A rare disease that caused patients to lose weight and urinate frequently was described in an Egyptian papyrus dating around 1552 BC. The term “diabetes”, which in Greek means siphon, was presumably coined by the physician Demetrius of Apameia (1<sup>st</sup> or 2<sup>nd</sup> century BC) in relation to the excessive urine output observed in patients. Eventually, the report of Thomas Willis in 1674 that the urine from diabetic patients was sweet, gave the disease its current name “diabetes mellitus” (DM) [1; 2].

Findings of the current 9<sup>th</sup> edition of the Diabetes Atlas from International Diabetes Federation (IDF) confirm that diabetes is one of the fastest growing global Health emergencies of the 21st century. In 2019, it is estimated that 463 million adults aged 20-79 years have diabetes and this number is predicted to reach 578 million by 2030, and 700 million by 2045. Other concerning facts about diabetes reported by IDF are related to clinical and economic burden. The number of deaths resulting from diabetes and its complications in 2019 is estimated to be 4.2 million. Moreover, annual global health expenditure on diabetes is estimated to be more than €620 billion with alarming increasing tendency [3].

Diabetes mellitus is a multifactorial long-term disease that comprises a group of metabolic disorders characterised by abnormally raised glucose levels in blood (hyperglycaemia) as a result of body inability to produce any or enough insulin, or reduced sensitivity of peripheral tissues despite its normal production. Insulin is an essential hormone produced by  $\beta$ -cells from the endocrine pancreas whose main role is to maintain glucose concentration in a physiological range (**Fig. 1**).

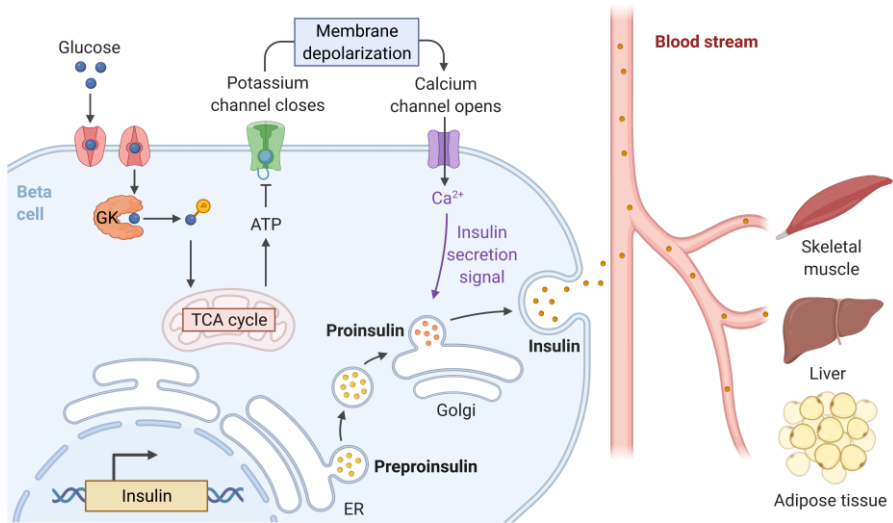


**Figure 1.** Stimulation of insulin secretion cascade in beta cells upon increase in blood glucose levels.

In response to hyperglycaemia after food intake, insulin is secreted to the bloodstream targeting peripheral tissues to stimulate glucose uptake by GLUT4 translocation to be used as energy or store as glycogen or triglycerides (**Fig. 2**).

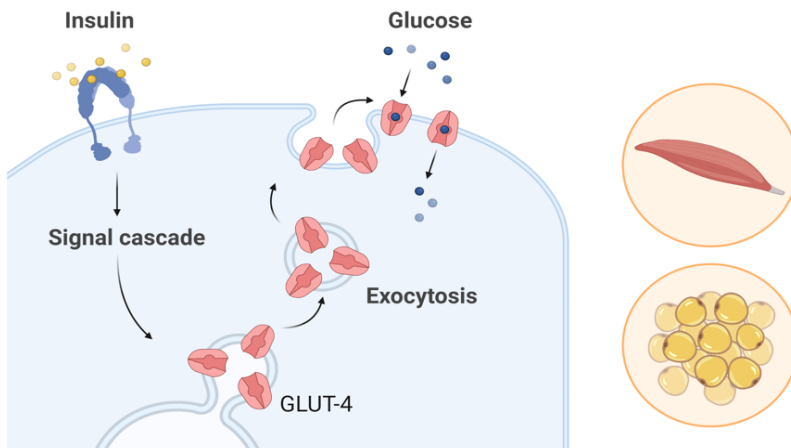


**Figure 2.** GLUT-4 translocation to the cell membrane upon insulin signalling enables glucose uptake in muscle and adipose tissue.

Typical symptomatology of diabetes includes polyuria, polydipsia, blurring of vision, fatigue, constant hunger and weight loss. In addition, lack of access to insulin treatment or delayed diagnosis may result in diabetic ketoacidosis, a common cause of death in children and young people with diabetes. Diabetes could be diagnosed if one or more of the following criteria are met: fasting plasma glucose  $\geq 7.0$  mmol/L (126 mg/dL), 2-hour post-load plasma glucose  $\geq 11.1$  mmol/L (200mg/dL), glycated haemoglobin (Hba1c)  $\geq 6.5\%$  (48 mmol/mol); or a random blood glucose  $\geq 11.1$  mmol/L (200 mg/ dl) in the presence of signs and symptoms of diabetes [3].

Several types of diabetes mellitus have been described based on the etiopathological mechanisms that lead to hyperglycaemia. Recently, World Health Organization published a report suggesting an update on diabetes mellitus classification (**Table 1**) [4].

**Table 1.** WHO classification of diabetes mellitus (2019 report).

Type 1 diabetes
Type 2 diabetes
Hybrid forms of diabetes
Slowly evolving immune-mediated diabetes of adults
Ketosis prone type 2 diabetes
Other specific types
Monogenic diabetes
Monogenic defects of $\beta$ -cell function
Monogenic defects in insulin action
Diseases of the exocrine pancreas
Endocrine disorders
Drug- or chemical-induced
Infections
Uncommon specific forms of immune-mediated diabetes

Other genetic syndromes sometimes associated with diabetes

Hyperglycaemia first detected during pregnancy

Diabetes mellitus in pregnancy

Gestational diabetes mellitus

This work will be focused on the most common type of diabetes which is type 2 diabetes mellitus (T2DM).

### 1.1. TYPE 2 DIABETES

T2DM has become a serious global health problem accounting for 90-95% of diabetes, affecting mainly middle-aged and elderly people, but also occurring increasingly frequently in children and adolescents. The risk of T2DM is determined by an interplay of genetic and environmental factors such as older age, excess body fat, unhealthy diet, physical inactivity and smoking (**Fig. 3**) [5]. Moreover, genome-wide association studies have described up to around 250 significant loci related to glucose uptake, insulin sensitivity, adipose storage, insulin secretion, etc. that increased the predisposition to T2DM [6; 7].

Overweight and obesity are the strongest risk factors for diabetes, both in terms of clearest evidence base and largest relative risk. Indeed, higher waist circumference and body mass index (BMI) are both associated with increased risk to diabetes development. Hence, several dietary practices like western diet are linked to unhealthy bodyweight and T2DM, including high intake of saturated fatty acids, sugar-sweetened beverages, or processed food. Modern life has triggered more sedentary and unhealthy lifestyles explaining the high and constant rising prevalence of T2DM.

Other factors that have been associated with diabetes development are gestational diabetes increasing the risk of offspring to develop the disease, and active smoking. In fact, risk remains elevated for about 10 years after smoking cessation [5].



**Figure 3.** Risk factors for type 2 diabetes includes genetic susceptibility, unhealthy lifestyle and obesity, and smoking.

Type 2 diabetes is characterised by a triad of metabolic alterations: insulin resistance, insulin secretory deficiency, and an increase in hepatic gluconeogenesis. Insulin resistance is the primary defect in T2DM and occurs when target tissues fail to respond normally to a given concentration of insulin [8].

As previously mentioned for T2DM, development of insulin resistance arises from the interaction between genetics and environmental factors such as obesity and unhealthy diet. In states of overnutrition, caloric intake exceeds energy expenditure leading to storage of extra calories in subcutaneous white adipose tissue (sWAT). In adulthood, sWAT primarily expands through enlargement of existing adipocytes (hypertrophy) whereas formation of new ones (hyperplasia) remains at very low rate [9]. Hyperplasia is considered

a healthy and adaptive process to storage fats. However, adipocytes hypertrophy is associated with tissue hypoxia, mechanical stress, increased lipolysis and free fatty acids (FFA) release leading to fibrosis, inflammation and insulin resistance [10]. It is hypothesized that may be a “personal fat threshold” at which adipose tissue storage capacity is overcome and ectopic fat deposition occurs in liver, muscle and viscera promoting also in those tissues an inflammatory milieu and reduced sensitivity to insulin [11]. Indeed, sWAT adipocyte size and insulin resistance correlation have been extensively reported in adults and children with obesity [12-15]. It is proposed that both inflammation and toxic metabolites (diacylglycerol, ceramides and acylcarnitines) resulting from nutrient overload cause insulin resistance by interfering in the signalling pathway of insulin receptor [16].

Initially, in response to lower insulin sensitivity, pancreatic  $\beta$ -cells increase insulin production leading to a compensatory hyperinsulinemia that maintains fasting blood glucose in near normal ranges and a mild postprandial hyperglycaemia, but below the diagnostic threshold for diabetes. This stage of impaired glucose tolerance is also known as prediabetes [8]. Progressively, endoplasmic reticulum (ER) overload due to increased insulin production [17; 18] added to glucose [19] and lipid toxicity [20] result in  $\beta$ -cell exhaustion and, eventually, in apoptosis. Therefore, endocrine pancreas begins to fail keeping on the demand of insulin, consequently leading to lower glucose uptake and increased hepatic gluconeogenesis, with a diagnose of T2DM [8]. This degenerative process typically develops through three progressive phases. Phase I: postprandial hyperglycaemia and increasingly dysfunctional  $\beta$ -cells; phase 2: fasting hyperglycaemia and significant  $\beta$ -cell atrophy;

and phase 3:  $\beta$ -cell can no longer release insulin and insulin replacement therapy is needed (**Fig. 4**).

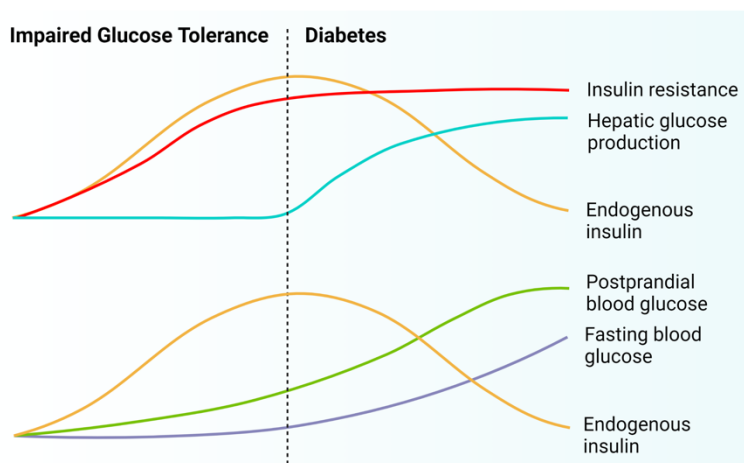


**Figure 4.** Natural history of type 2 diabetes mellitus.

IDF published in 2017 a Clinical Practice Recommendations for managing Type 2 diabetes in Primary Care [21]. Lifestyle changes, including smoking and alcohol intake avoidance, increasing physical activity and reduction of caloric intake, are recommended as the first line of treatment for T2DM. Some guidelines recommend anti-obesity drugs or bariatric surgery in those cases in whom BMI was above 27 kg/m<sup>2</sup> or 35 kg/m<sup>2</sup>, respectively.

Metformin is the preferred choice to start monotherapy when lifestyle modifications are not sufficient to control diabetes. Other glucose-lowering drugs can be used as monotherapy if metformin intolerance is observed. Combination therapy of metformin and another glucose-lowering drug could be the best treatment when HbA1c is 1% to 2% above 6.5%. In the case of unstable diabetes with symptoms of dehydration, acute weight loss, acute illness, uncontrolled hyperglycaemia and presence of ketones, most guidelines



recommend insulin administration alone or in combination with glucose-lowering drugs.

Diabetes mellitus is also associated with long-term vascular complications that can be grouped in microvascular disease which includes neuropathy, nephropathy and retinopathy, and macrovascular disease that is related with strokes and myocardial infarction (**Fig. 5**). These complications, especially peripheral neuropathy, represent the main reasons of disability, reduced life expectancy and economic cost associated with diabetes [3; 22].

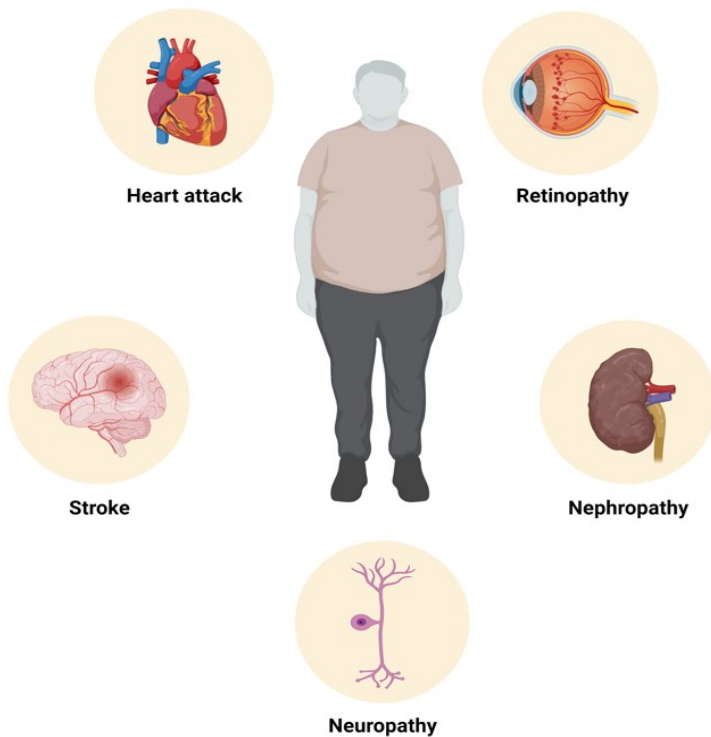


**Figure 5.** Long-term complications of diabetes mellitus.

## 2. DIABETIC NEUROPATHY

Diabetic neuropathy (DN) is the most common and debilitating complication of diabetes, affecting 50-60% of patients with T1DM and T2DM, although neurophysiological alterations are found in most patients. The development of DN is a late event and normally occurs 20 or more years after diabetes onset. DN includes a heterogeneous group of conditions with diverse clinical manifestations caused mainly by damage to the peripheral nervous system (PNS), although the spinal cord and the brain could also be affected [22].

### 2.1. STRUCTURE AND FUNCTION OF THE PERIPHERAL NERVOUS SYSTEM

PNS refers to all the nerves branching out from the brain and spinal cord (central nervous system, CNS) that innervate the rest of the body. PNS can be divided in visceral nervous system that regulates involuntary body functions to maintain homeostasis, and somatic nervous system which relays external and internal sensorial information and controls muscular movement (**Fig. 6**). Both systems comprise peripheral nerves (spinal and cranial nerves) and ganglia with the corresponding cellular and connective tissue elements.

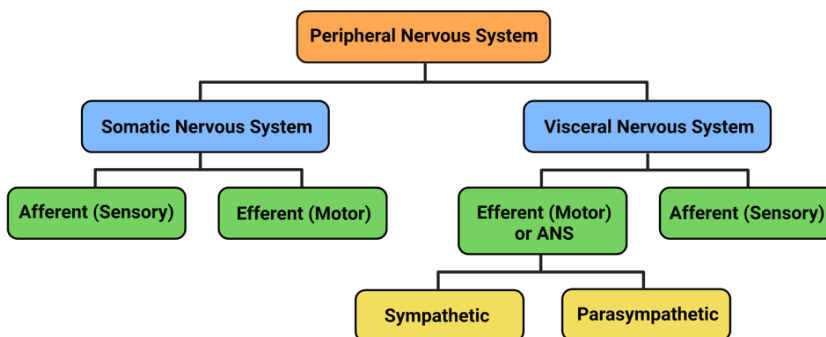


**Figure 6.** Peripheral nervous system classification.

Human spinal cord has 31 segments (8 cervical, 12 thoracic, 5 lumbar, 5 sacral and 1 coccygeal), each of which (except C1, with only a ventral root) has a pair of dorsal and ventral roots joining each pair into a spinal nerve (**Fig. 7**) [23]. Conversely, mouse spinal cord is composed of 34 segments: 8 cervical, 13 thoracic, 6 lumbar, 4 sacral and 3 coccygeal. Each spinal nerve divides into a ventral and dorsal ramus after crossing its intervertebral foramen. The dorsal ramus is a mix of sensory and motor fibres that supply the extensor muscles of the vertebral column and skull, and the overlying skin, whereas ventral ramus innervates everything else. In addition, 12 pairs of cranial nerves that emerge from brain and spinal cord cross the cranium to reach their peripheral targets [24].

The ventral root of the spinal nerve contains two types of efferent neurons, somatic and visceral. Perikarya from somatic efferent neurons are placed in the anterior (or ventral) horn of spinal cord and their axons reach the spinal nerve through ventral root. From there, the fibres from these somatic multipolar neurons travel into either the dorsal or ventral rami to innervate the skeletal muscle. Regarding cell bodies of visceral efferent neurons, those are in the intermediolateral portion of the grey matter. These fibres, known as preganglionic, also exit the spinal cord from the ventral root. Between T1 and L2, preganglionic sympathetic neurons are found, whereas preganglionic parasympathetic neurons are located between S2 and S4. The preganglionic sympathetic neurons leave the spinal nerve via white ramus communicans (between T1 and L2) to synapse with the cell bodies of multipolar postganglionic neurons located mainly in the ganglia from paravertebral sympathetic chain (except for celiac and mesenteric ganglia). Axons from postganglionic neurons join via the gray ramus communicans every spinal nerve from the C1 to the coccygeal nerve (**Fig. 7**).

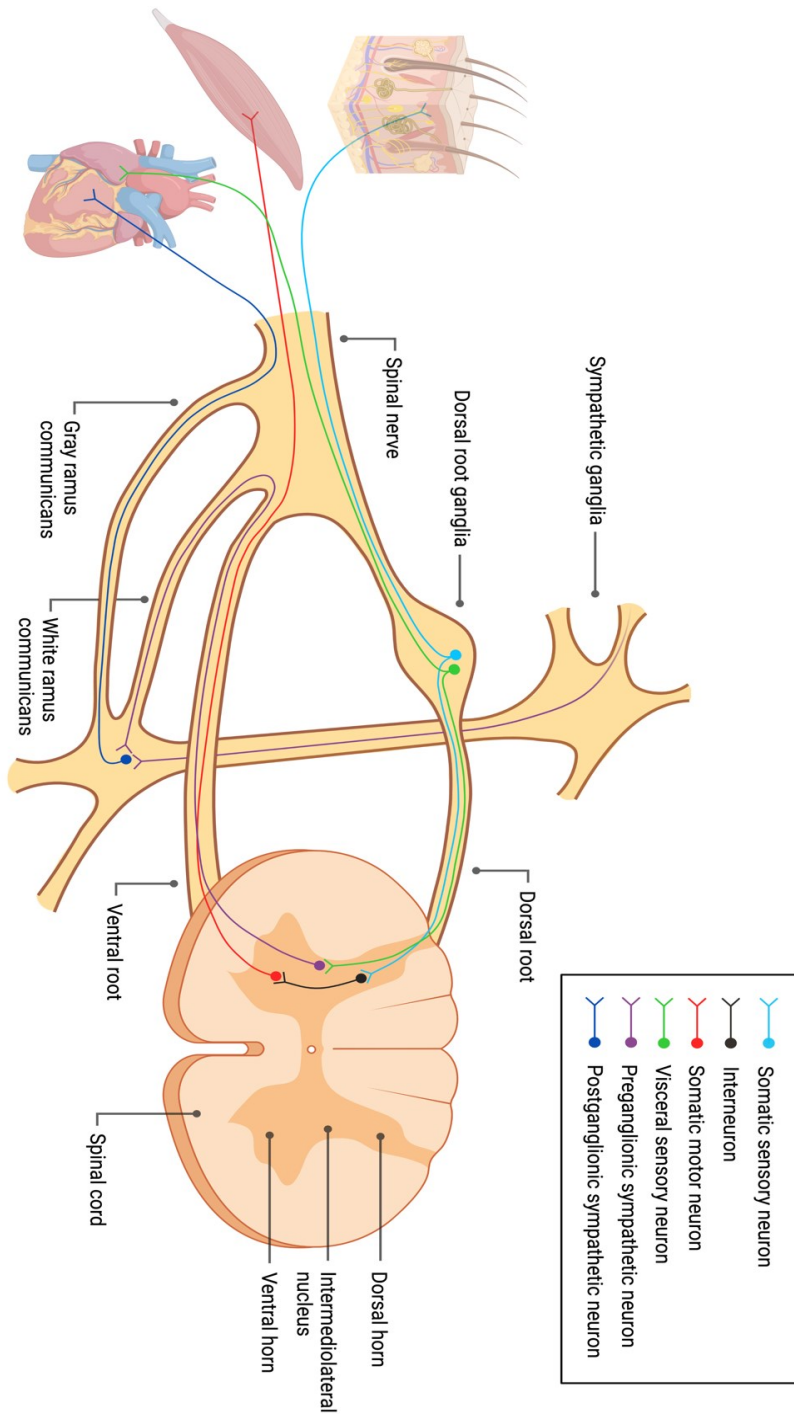


**Figure 7.** Somatic and visceral neurons outflow from the spinal cord to peripheral tissues.

Conversely, preganglionic parasympathetic neurons synapse with multipolar postganglionic neurons placed in ganglia that are close to or embedded within target organs. Sympathetic and parasympathetic neurons constitute the autonomic nervous system (ANS) which corresponds to the motor division of visceral nervous system (**Fig. 8**) [25].

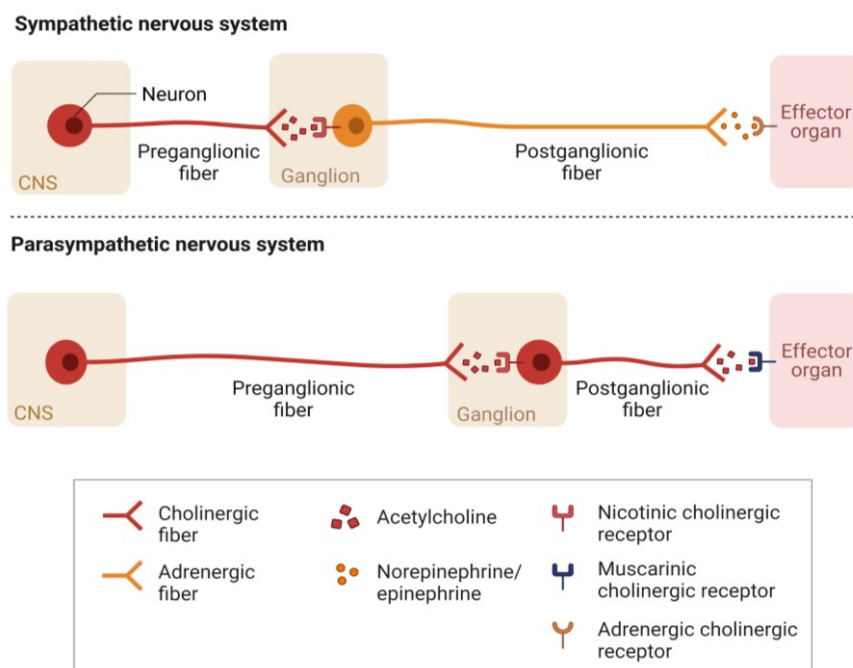


**Figure 8.** Organization of autonomic nervous system comprising sympathetic and parasympathetic divisions.

Dorsal root also contains two types of pseudo-unipolar neurons, somatic afferents, and visceral afferents, both relaying sensorial information. The perikarya from these neurons constitute a cell cluster located in a nodule-like structure found in the dorsal root outside the spinal cord. Specifically, **dorsal root ganglia (DRG)** lie in the foramen between two spinal vertebrae. Somatic afferent neurons transmit information to the CNS from body structures such

as skin, tendons, and skeletal muscles. The second group of neurons, visceral afferents, constitute the sensory division of visceral nervous system which is responsible to convey sensorial information from viscera [26]. Axons from somatic and visceral neurons enter the spinal cord via dorsal roots where synapse with interneurons or preganglionic neurons, respectively. Thus, interneurons, which are found entirely in the CNS, allow to connect somatic sensory neurons with somatic motor neurons. On the other hand, preganglionic neurons which have cell bodies inside the CNS and their axons crossing to the PNS, have the same role as somatic interneurons allowing the transmission of information from visceral sensorial neurons to visceral efferent fibres (**Fig. 7**) [25].

Sensory ganglia are surrounded by a tough collagenous capsule that is continuous with the epineurium and the perineurium of peripheral nerve [25]. In addition to neurons, DRG contain connective tissue, fibroblasts, satellite cells, capillaries (endothelial cells and vascular smooth muscle cells), lymphocytes, macrophages and myelinating and non-myelinating Schwann cells associated with neuronal axons [27]. Therefore, the dorsal sensory roots contain both myelinated and unmyelinated axons.

Spherical perikarya in DRG are completely wrapped by satellite glial cells forming a tight envelope resembling a ring. These neuron-glia units are separated by a connective tissue that is continuous with the endoneurium of the peripheral nerve. In most cases, neurons are wrapped individually by numerous satellite cells. However, in few cases, neurons form a cluster sharing a common glial envelope. To note, satellite cells are also present in sympathetic and parasympathetic ganglia.

Little is known about the role of satellite cells in DRG, but it has been described that they may modify the microenvironment of neurons by uptake and release of molecules, receive and transmit chemical signals, provide mechanical support, and control neuronal morphology. Moreover, it seems that satellite cells release pro-inflammatory cytokines after nerve damage, which may increase the excitability of neurons contributing to neuropathic pain. Interestingly, despite their particular distribution around neurons, these cells seem not to have a barrier function allowing the crossing of small neurotransmitters and macromolecules [25; 28; 29].

It is worth mentioning that while in the CNS, endothelial cells constitute a blood barrier to tightly regulate the movement of ions and molecules and protect from toxins and pathogens, in the PNS the blood-nerve barrier is relatively deficient since some of the capillaries are fenestrated. Hence, DRG neurons are more vulnerable than motor neurons to external attacks [30].

Axons from PNS are associated with **Schwann cells** defining nerve fibres. These glial cells are exclusively found in the PNS and could present a myelinating as well as non-myelinating phenotype. Myelin sheath is a complex and highly organized structure containing 70% of lipids (high levels of cholesterol and glycosphingolipids) and 30% of proteins of which P0, MBP and PMP22 account for the most abundant. Myelin arises from spiral wrapping of Schwann cell plasma membrane around the axon. However, myelination along the axon does not occur as a continuous structure but results from discrete segments of myelin (internodes) wrapping a single axon separated by nodes of Ranvier. Each internode is derived from a single Schwann cell.

**Myelin** constitutes an insulating layer that prevents depolarization to occur at any point except at nodes of Ranvier where axolemma containing high concentration of voltage-sensitive Na<sup>+</sup> channels is exposed. Therefore, the action potential appears to jump over the internodes from one node to another, a process known as saltatory conduction, dramatically increasing the nerve impulse velocity compared to unmyelinated axons. Integrity of myelin is crucial to ensure normal activity of the PNS. Indeed, pathological conditions may result from even small deviation from normal structure.

Contrary to myelinated axons in which multiple Schwann cells surround a single axon, non-myelinating Schwann cells are able to individually ensheath several small-calibre axons in Remak bundles. Therefore, Schwann cells not only have a vital role increasing conduction velocity in myelinated fibres, but also have an energy-supplying role providing nutrients to axons as well as mechanical support. Moreover, Schwann cells can phagocytose cellular debris after nerve damage [31].

As previously explained for DRG, myelinated and unmyelinated axons are surrounded by three layers of connective tissue (**Fig. 9**). The outermost layer is called epineurium and consists of dense, irregularly arranged connective tissue that envelops the entire nerve. This layer also contains considerable quantities of adipose tissue.

The perineurium layer separates fascicles of axons. In contrast to epineurium, perineurium is composed of a regular structure of laminae of modified fibroblasts alternating with collagenous sheets. Perineurium maintains a constant microenvironment in the endoneurial space and forms a barrier to diffusion between the epineurium and endoneurium.



Lastly, each axon is individually surrounded by a loose connective tissue called the endoneurium that contains fibrous collagen, fibroblasts, macrophages, and small blood vessels. Endoneurium provides mechanical strength to the fascicle and represents the microenvironment of PNS components.

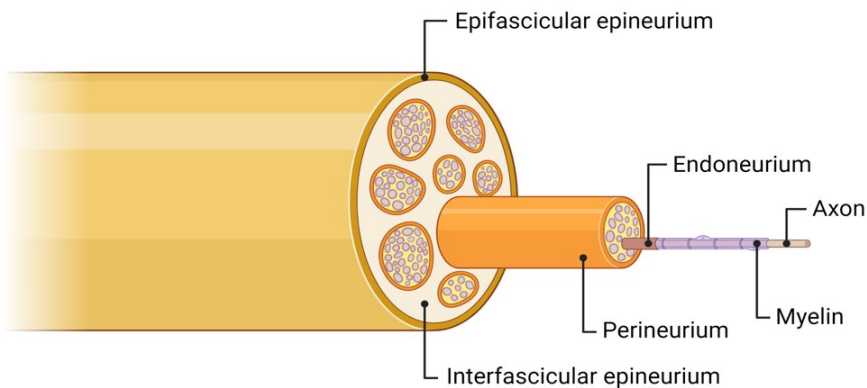


**Figure 9.** Connective layers of peripheral nerves comprising epineurium, perineurium and endoneurium.

In all vertebrates, spinal nerves are organized as branching networks of intersecting nerves known as plexuses. Thus, nerve branches distal to the plexus receive contributions from different spinal nerves. Moreover, each plexus is a mix of somatic and autonomic fibres that innervate peripheral extremities and viscera. For instance, human lumbosacral plexus is constituted by lumbosacral trunk (L4 and L5) and sacral nerves (S1 to S4). From that, arises the **sciatic nerve** (SCN), the largest nerve in the body, consisting of fibres that converge from L4, L5 and S1 to S3 ventral rami. Conversely, sciatic nerve from mouse predominantly originates from the spinal nerves L3 and L4. It extends throughout most of the thigh before dividing into the common peroneal and tibial nerves [25; 30].

Fibres in peripheral nerves present a variable calibre, ranging from very fine unmyelinated to thick myelinated fibres. The Erlanger/Gasser classification of peripheral nerve fibres subdivides fibres based on diameter and conduction velocities (**Table 2**) [32].

**Table 2.** Erlanger-Gasser classification of nerve fibres [32].

Fiber class	Nervous system classification	Numeric classification	Function	Diameter (µm)	Conduction (m/s)	Myelination
Aα	Somatic afferent	type Ia	Proprioception (muscle spindle)	12-20	70-120	+
	Somatic afferent	type Ib	Proprioception (tendon organs)	12-30	70-120	+
	Somatic efferent		Extrafusal skeletal muscle	12-20	70-120	+
Aβ	Somatic afferent	type II	Proprioception (muscle spindle), touch	5-12	30-70	+
Aδ	Somatic afferent	type III	Pain, touch, cold	2-5	12-30	+
Aγ	Somatic efferent		Muscle spindle	3-6	15-30	+
B	Autonomic		Preganglionic fibers	<3	3-14	+
C	Somatic afferent	type IV	Pain, touch, warm, cold	0,4-1,2	0,5-2	-
C	Autonomic		Postganglionic sympathetic fibers	0,3-1,3	0,7-2,3	-

Anatomically, somatic sensory fibres can also end freely or, conversely, develop an encapsulated nerve ending such as Meissner's corpuscles or Pacinian corpuscles, which are present in regions with highly developed sensitivity. In addition, sensorial impulses can be divided into exteroceptive and proprioceptive. Exteroceptive impulses arise from receptors that sense touch and pressure (mechanoreceptors), changes in temperature (thermoreceptors) and painful stimuli (nociceptors) proceeding from the external environment, whereas proprioceptive impulses derive from internal stimulus generated in joints, ligaments, fascia and muscles to perceive body's own position and movement [25].

### 2.1.1. NEURAL CONTROL OF SWEAT SECRETION

Sweating capacity allow to regulate body temperature, release waste products and respond to emotional stress. Humans present two main sweat gland types: eccrine and apocrine (**Fig. 10**). Eccrine glands are found throughout the body, accounting for 90% of the total number of sweat glands. These glands are placed in the dermis and release directly onto the skin surface an odourless, hypotonic solution and electrolytes for temperature and waste regulation.

Apocrine sweat glands are found in particular areas such as the axillae, the mons pubis, the external auditory meatus, the areolae and the circumanal area. Contrary to eccrine, apocrine glands are located in the lower dermis or the subcutaneous fat and secrete sweat into the hair follicles. This kind of sweat, mixed in the follicle with sebum, contains proteins, pheromones and steroids as well as urea, which causes its distinct odour. Sweating of apocrine glands is triggered mainly by sexual excitement and emotional stresses [33].

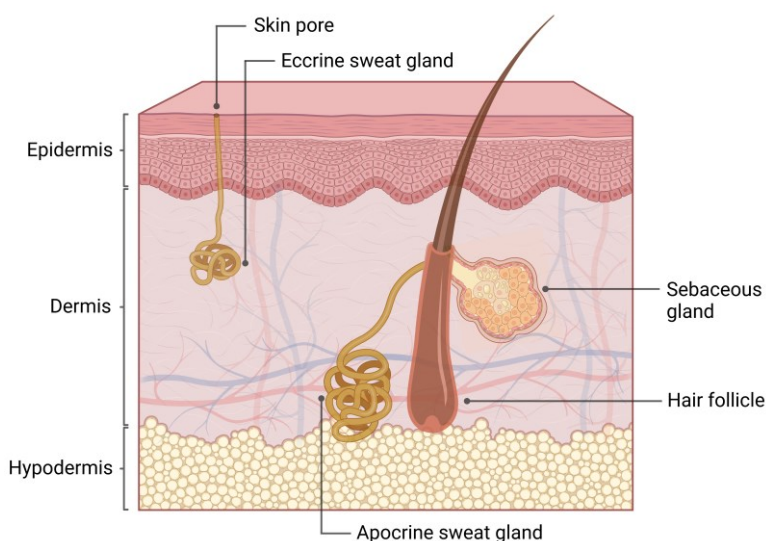


**Figure 10.** Structure of skin containing eccrine and apocrine sweat glands.

Sweating is regulated by sympathetic nervous system through acetylcholine and catecholamines (noradrenaline and adrenaline). Despite postganglionic sympathetic fibres are primarily adrenergic, eccrine glands are mainly controlled by cholinergic sympathetic neurons (**Fig. 11**). However, catecholamines may also have some effect on sweating control since adrenergic receptors are expressed in these glands. On the other hand, apocrine secretion is only regulated by the action of catecholamines [34-36].

Even though the main role of eccrine glands is to control body temperature by sweating, those placed in palms and soles are not involved in thermoregulation. Instead, these glands are activated upon emotional stresses despite do not differ morphologically, pharmacologically, or neurologically from those activated by heat [37; 38].

### Sympathetic nervous system

#### Eccrine sweat glands

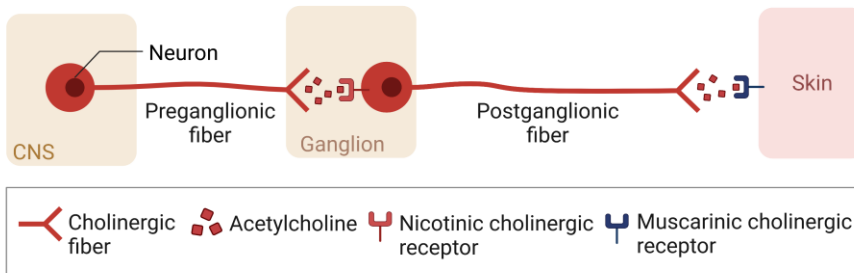


**Figure 11.** Sympathetic neurons stimulate eccrine sweat glands through acetylcholine release.

## 2.2. SOMATIC NERVOUS SYSTEM AND DIABETES

Nowadays, it is not completely clear whether diabetes affects first the Schwann cells and thus the myelin sheath, or the axons from sensory neurons. Indeed, one could expect to observe in a sural nerve biopsy from a diabetic patient a broad spectrum of axonal and myelin pathologic abnormalities comprising progressive degeneration of terminal axons towards the cell body, known as dying-back degeneration, fibre loss, abnormal regenerative sprouts, segmental demyelination and remyelination (**Fig. 12**). To note, demyelination could be primary if involves only the degeneration of myelin with intact axon (segmental demyelination), or secondary if myelin breakdown occurs after axonal atrophy.

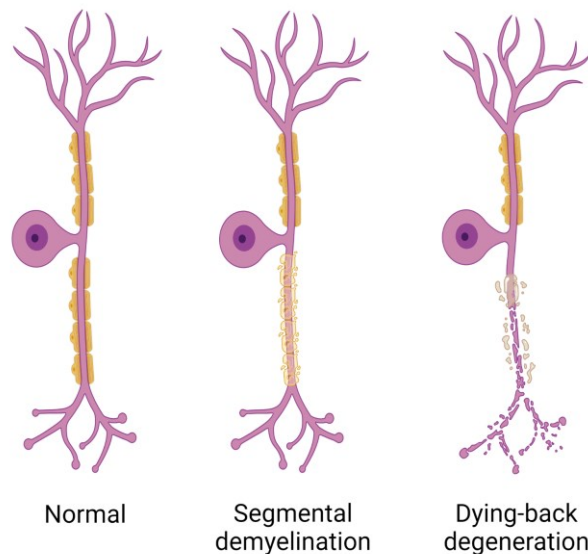


**Figure 12.** Axonal and myelin abnormalities observed in diabetic neuropathy.

Dyck et al. [39] studied sural nerve biopsies from diabetic patients observing that type of fibre abnormalities could depend on duration of diabetes and neuropathy symptomatology. Therefore, in patients with diabetes but with any sign of neuropathy, a higher frequency of

segmental demyelination and remyelination was found. Those patients that did not receive treatment and develop symptoms of DN showed both segmental demyelination and remyelination, and axonal degeneration. Conversely, axonal degeneration was the most common alteration found in treated patients that suffered longstanding neuropathy.

Another study drew similar conclusions from electrophysiological analysis of sural and peroneal nerves. Conduction velocity, but not amplitude, was slower in patients without signs of DN, whereas patients with symptomatology showed amplitudes and conduction velocities significantly lower compared to non-symptomatic patients. Therefore, they concluded that both types of patients could develop a demyelinating disease, while loss of axons was only present in symptomatic ones [40].

Malik et al. [41] studied early pathological features in sural nerves from diabetic patients with minimal evidence of neuropathy. Segmental demyelination and remyelination without axonal degeneration were described. However, they also observed features of degeneration and regeneration of unmyelinated fibres since a reduction in axonal diameter as well as an increase in their density was found. It is worth mentioning that small-diameter nerve fibres represent 70-90% of all peripheral fibres and appeared to be damaged earlier by diabetes than larger myelinated fibres resulting in neuropathic pain [42; 43].

In addition to these publications, many other studies have observed fibre loss accompanied with segmental demyelination in established diabetic neuropathy [44-46].

### 2.3. SUDOMOTOR FUNCTION AND DIABETES

Autonomic neuropathy involving the degeneration of postganglionic sudomotor axons is a common complication of diabetes mellitus that results in sweating disorders. Usually, distal anhidrosis in a glove and stocking distribution is developed accompanied by compensatory hyperhidrosis in head and trunk [47; 48].

### 2.4. CLASSIFICATION OF DIABETIC NEUROPATHY

As previously presented, DN includes a vast group of conditions that can affect different parts of nervous system with diverse clinical manifestations. Among the various forms of DN, detailed in **Table 3**, distal symmetric sensorimotor polyneuropathy is the most common and the most studied presentation of the disease.

**Table 3.** Classification for diabetic neuropathies [49]

Diabetic neuropathies
Diffuse neuropathy
Distal symmetric polyneuropathy
Primarily small-fibre neuropathy
Primarily large-fibre neuropathy
Mixed small- and large-fibre neuropathy (most common)
Autonomic
Cardiovascular
Gastrointestinal
Urogenital
Sudomotor dysfunction
Hypoglycaemia unawareness
Abnormal pupillary function
Mononeuropathy (atypical forms)
Isolated cranial or peripheral nerve

Mononeuritis multiplex

Radiculopathy or polyradiculopathy (atypical forms)

Radiculoplexus neuropathy

Thoracic radiculopathy

Nondiabetic neuropathies common in diabetes

Pressure palsies

Chronic inflammatory demyelinating polyneuropathy

Radiculoplexus neuropathy

Acute painful small-fibre neuropathies (treatment-induced)

Distal symmetric polyneuropathy manifests with a “stocking and glove” pattern characterised by a progressive distal-to-proximal degeneration of sensory fibres, early in the course of DN. Approximately half of the patients with DN develop neuropathic pain characterised most commonly by spontaneous burning sensation of the feet. Patients also develop abnormal sensory perception including paraesthesia (“pins and needles” sensation), hyperalgesia (increased sensitivity to a noxious stimulus) and allodynia (pain evoked by non-noxious stimulus). Interestingly, these positive sensory symptoms are often concomitant of reduced sensitivity to temperature and touch that, combined with poor wound healing, may eventually result in foot ulcerations and lower limb amputations, accounting for up to 15% of this type of intervention [22]. At late stages, motor fibres also become damaged by diabetes, leading to distal weakness of the toes, or in extreme cases, ankles and calves. Furthermore, diabetic nerves develop vascular abnormalities such as capillary basement membrane thickening, leading to reduced blood flow and hypoxia [50; 51].



## 2.5. DIABETIC NEUROPATHY PATHOPHYSIOLOGY

In contrast to muscle fibres or adipocytes, neurons and glia do not depend on insulin signalling to modulate glucose uptake since, unlike GLUT4, GLUT1 and GLUT3 transporters mediate basal glucose transport independently of this hormone. Thus, in diabetes, blood hyperglycaemia is associated with marked increased in intracellular glucose levels in PNS [52].

In 2001, Brownlee proposed a unifying hypothesis linking hyperglycaemia with the activation of different pathways involved in oxidative stress generation. These includes polyol pathway, advanced glycation end products (AGEs) formation and hexosamine pathway [53].

### 2.5.1. OXIDATIVE STRESS

Oxidative stress is defined as the disturbance of balance between reactive oxygen/ nitrogen species (ROS/ RNS) production and the cell capacity to counteract their action by antioxidant defences. The imbalance in cell redox state can emerge from enhanced reactive species generation or from a reduced endogenous antioxidant activity. ROS include both free radical and non-free radical oxygenated molecules. Free radicals are highly reactive atoms or molecules with one or more unpaired electron(s) in their external orbit. ROS are generated as natural by-products of normal cell activity such as mitochondrial respiration, detoxification or peroxisomal beta-oxidation.

Mitochondria are the main source of endogenous ROS resulting from oxidative ATP production, in which molecular oxygen ( $O_2$ ) is reduced to water in the electron transport chain (**Fig. 13**).

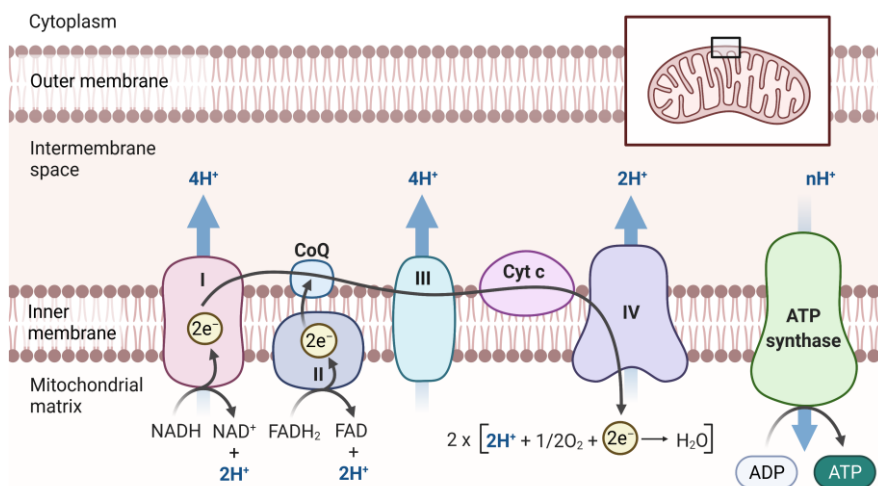
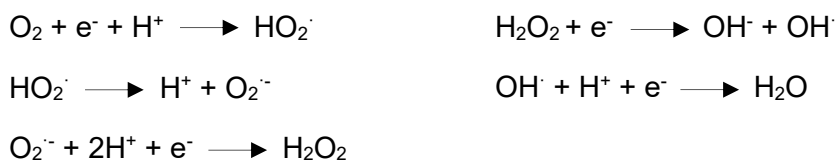


**Figure 13.** Normal electron transport chain and oxidative phosphorylation.

The molecular oxygen reduction occurs as follows:



Superoxide radical ( $\text{O}_2^{\cdot-}$ ) may also result from one electron reduction of oxygen by oxidases such as xanthine oxidoreductase, NADPH oxidase and cyclooxygenase. Hydrogen peroxide ( $\text{H}_2\text{O}_2$ ) may also arise from dismutation of  $\text{O}_2^{\cdot-}$ , NADPH oxidases, CYP catalytic cycle, peroxisomal enzymes, normal protein folding and polyunsaturated fatty acid metabolism. Hydroxyl radical ( $\text{OH}^\cdot$ ) is a highly oxidizing molecule that also derives from radiolysis of water and hydrogen peroxide reaction with metal species (Fenton reaction). In addition, other ROS can be found such as hydroperoxyl, peroxy and alkoxy radicals.

Even though high ROS amounts are associated with many diseases such as Alzheimer, ALS, Parkinson, cataracts or cancer, appropriate concentrations have a role in cell signalling, being involved in the regulation of cell proliferation, apoptosis and gene expression. In addition, activated phagocytes, for instance, produce ROS as a defence mechanism against bacteria or fungi. Therefore, it is crucial to ensure balance between ROS production and scavenging to maintain redox homeostasis. Thus, cells have evolved a complex endogenous system to neutralise the extra ROS which includes antioxidant enzymes such as superoxide dismutase, catalase, glutathione peroxidase, and non-enzymatic compound like glutathione, proteins (ferritin, transferrin, albumin) and low molecular weight scavengers, like coenzyme Q and lipoic acid [54; 55].

#### 2.5.2. POLYOL PATHWAY

In physiological conditions, once inside the cell, glucose enters glycolysis pathway and is converted into glucose-6-phosphate by hexokinase. However, in hyperglycaemic conditions, it is likely that hexokinase is saturated and glucose excess is converted to sorbitol by aldose reductase enzyme (polyol pathway). Accumulation of sorbitol results in an osmotic stress since its low plasma-membrane permeability. Moreover, aldose reductase activity consumes the proton donor NADPH which is necessary for regeneration of glutathione. As a consequence of glutathione depletion, glutathione peroxidase capacity is compromised leading to increase in superhydroxyl radicals ( $\bullet\text{OH}$ ) production from hydrogen peroxide ( $\text{H}_2\text{O}_2$ ), instead of being metabolised into water, thus contributing to oxidative stress. In addition, sorbitol could be converted to fructose by sorbitol dehydrogenase which may contribute to the formation of

intracellular AGEs. This is particularly important for glial cells in the PNS, since neurons do not express aldose reductase enzyme [56].

### 2.5.3. ADVANCED GLYCATION END PRODUCTS

AGEs result from the non-enzymatic reaction of a reducing sugar with amino group of proteins, lipids and nucleic acids. There are several processes that contribute to AGEs formation such as glucose autoxidation, Maillard reaction between glucose and proteins residues, glycolysis, polyol pathway and lipid peroxidation. These processes generate reactive dicarbonyls including methylglyoxal, glyoxal and 3-deoxyglucosone that are precursors of AGEs [57]. The irreversible glycation of essential molecules alters their function causing cellular damage and dysfunction. It has been described that peripheral nerve myelin is highly glycated in diabetes which makes it susceptible to phagocytosis by macrophages contributing to demyelination [58]. Cytoskeletal proteins such as tubulin, neurofilament, and actin, as well as extracellular matrix proteins like collagen and laminin also undergo glycation under hyperglycaemic conditions leading to slower axonal transport and impaired nerve regeneration [59; 60]. Moreover, AGEs also bind to AGEs receptor (RAGE) inducing reactive oxygen species accumulation through the activation of NF- $\kappa$ B pro-inflammatory pathway and NAD(P)H oxidase, establishing a favourable milieu to generate more AGEs [61].

### 2.5.4. HEXOSAMINE PATHWAY

Oxidative stress inhibits glyceraldehyde-3-phosphate dehydrogenase (GAPDH) activity [62] leading to the activation of hexosamine pathway by diverting the upstream metabolite fructose-

6-phosphate to uridine 5-diphosphate-N-acetylglucosamine (GlcNac). GlcNac binds serine and threonine residues on common transcription factors, blocking its phosphorylation and thus compromising its normal function [63]. Interestingly, it has been recently demonstrated that Schwann cells develop ER stress under glucosamine exposure [64]. In addition, inhibition of GAPDH activity also increases glyceraldehyde-3-P, which can be converted to methylglyoxal contributing to AGEs generation.

#### 2.5.5. ROS-MEDIATED MODIFICATION OF BIOMOLECULES

Overall, hyperglycaemia-mediated ROS production will eventually overwhelm antioxidant defences leading to oxidative attack of biomolecules like lipids, DNA and proteins, modulating their structure and function, and leading to PNS degeneration [65].

Lipids, mainly from cellular membrane, are the most susceptible to undergo oxidation leading to changes in the permeability and fluidity of plasma membrane altering cell integrity. Moreover, lipid peroxidation products like malondialdehyde (MDA) can react with DNA to form guanosine, adenosine and cytidine adducts which eventually results in genome genotoxicity. In addition, MDA and other lipid peroxidation products can also covalently modify proteins altering their structure and function compromising cell viability [66].

ROS also mediate damage to DNA/RNA by direct oxidation of nucleotides eventually leading to their mutation or strand breakage. The most common marker for DNA oxidation is 8-hydroxydeoxyguanosine adduct which causes loss of base-pairing specificity, misreading of adjacent pyrimidines, or insertion of

adenine opposite the damage site generating mainly a G → T transversion [67].

Besides protein glycooxidation, ROS may affect protein structure by direct oxidation of amino acid side-chains, formation of protein-protein cross-linkages, and oxidation of the protein backbone resulting in its fragmentation [68].

#### 2.5.6. OXIDATIVE METABOLISM UNDER DIABETIC CONDITIONS

Although the main unifying mechanism proposed by Brownlee, 2001 is still accepted, there are some aspects that need to be revised. It was postulated that under conditions of excess flux of glucose towards glycolysis and tricarboxylic acid cycle (TCA), NADH and FADH<sub>2</sub> concentration increases generating an abnormally high mitochondrial membrane potential. The altered electrical gradient would inhibit the transport of electrons at complex III, increasing the half-life of free-radical intermediates of co-enzyme Q, facilitating the reduction of O<sub>2</sub> to superoxide [53].

Even though it is expected that nutrient overload would increase glycolysis, TCA cycle and oxidative phosphorylation, metabolic activity of peripheral nerves is compromised due to an overwhelmed system. Indeed, reduced respiratory chain activity was described in mitochondria from DRG in type 1 diabetic rats and type 2 diabetic mice [69; 70]. Akude et al. [71] also demonstrated that DRG sensory neurons from type 1 diabetic rats exhibited lower levels of proteins related to respiratory chain complexes and tricarboxylic acid cycle. Interestingly, lower oxidative phosphorylation was associated with a decrease in superoxide radical generation, despite oxidative stress was present in axons of diabetic neurons.

Similar reduction in TCA cycle, as well as in glycolytic pathway, was observed in the sciatic nerve from type 2 diabetic mice using metabolomics, whereas oxidation of lipids and proteins were found increased [72].

#### 2.5.7. ROLE OF DYSLIPIDAEMIA IN DIABETIC NEUROPATHY

Furthermore, hyperglycaemia-mediated damage has been considered the main risk factor for neuropathy development for years. Nonetheless, studies involving more than 11,000 individuals from different countries consistently demonstrated that obesity is independently associated with neuropathy [73]. Moreover, another study found that metabolic syndrome also correlated with diabetic neuropathy progression, independently of glycaemic status [74]. Metabolic syndrome is a condition diagnosed by development of at least three out of five metabolic risk factors: a large waistline, high triglyceride level, low HDL cholesterol level, high blood pressure and high fasting blood sugar. Therefore, dyslipidaemia has emerged as an important risk factor to focus on to better understand the physiopathology of DN in type 2 diabetes in contrast with type 1.

In obesity, FFA have systemic effects promoting inflammatory cytokine release from adipocytes and macrophages [75], but also local effects in the PNS. Triglycerides accumulate in nerves upon a high-fat diet (HFD) enriched in saturated fatty acids [76]. Under normal conditions, the ER membrane has a low free cholesterol to phospholipid ratio and a low saturated FFA content. However, exposure to hyperlipidaemia lead cholesterol and saturated FFA-containing phospholipids to accumulate, reducing its fluidity. It has been described that loss in membrane fluidity inhibits  $\text{Ca}^{2+}$  transport to ER lumen which triggers protein misfolding and ER stress [77].

Furthermore, the release of  $\text{Ca}^{2+}$  into the cytosol may overload the mitochondrial matrix inducing membrane depolarization. Thus, palmitate induced a dose-dependent increase in mitochondrial depolarization and consequent reduction in ATP level *in vitro* [78; 79]. Membrane depolarization impairs mitochondrial motility by inducing Miro GTPase degradation [80]. Also, increased calcium influx by itself promotes detachment of the mitochondria from microtubules halting its trafficking [81; 82]. Therefore, mitochondrial trafficking along the axon in cultured sensory neurons exposed to palmitate is impaired with reduced number of motile mitochondria and lower velocity [79]. Schwann cells cultured *in vitro* can also be directly damaged by FFA exposure inducing ER stress [83]. Conversely, saphenous nerve from HFD-fed mice does not exhibit impaired mitochondrial trafficking although increased in size and number was observed as well as reduced membrane potential [84].

Interestingly, fatty acid effects depend on saturation level since unsaturated FFA oleate prevents the deleterious effect of palmitate in skeletal muscle [85] and in cultured sensory neurons [78]. Furthermore, Rumora et al. [78] also demonstrated that neuropathy was completely reversed by switching the mice diet from saturated fatty acid enriched HFD to monounsaturated fatty acid enriched diet. In addition, consuming a diet rich in unsaturated fatty acids has also been associated with reduced risk of developing T2DM [86] and cardiovascular disease [87].

Lipoproteins like LDLs can be oxidised by lipid peroxidation products, changing their affinity towards receptors like RAGE [88], LOX1 [89] and TLR4 [90] that trigger NADPH oxidase activation, contributing to oxidative stress and inflammatory milieu. Moreover, it



has also been described that oxysterols derived from cholesterol oxidation may cause apoptosis of neurons *in vitro* [91].

#### 2.5.8. ROLE OF MITOCHONDRIA AND ENDOPLASMIC RETICULUM

Neurons are dependent on a continuous supply of ATP for their normal function and survival, which is highlighted by the greater mitochondrial density found compared to other cell types [92]. PNS axons can measure almost one meter in length, so mitochondrial trafficking is crucial to ensure their distribution along axons. Mitochondria concentrate in regions of high metabolic demand such as axonal preterminal area [93; 94] to supply enough ATP. Hence, transporting mitochondria from the neuronal perikarya to these highly active regions plays a key role in cell survival, synapsis and growth cone motility [95].

Mitochondria are highly dynamic organelles that undergo cycles of fission and fusion to regulate their number, morphology, and size [96]. Interestingly, mitochondrial bioenergetics are dependent on mitochondrial dynamics since fusion is enhanced under nutrient starvation to increase ATP production efficiency, whereas nutrient excess leads to mitochondrial fission boost to distribute metabolic overload [92]. However, excessive fission may lead to membrane depolarization which decreases ATP production impairing neuronal function.

Impaired mitochondrial function has been described in diabetic neuropathy, as previously explained, resulting from metabolic overload. Thus, abnormal mitochondrial trafficking and reduced electron chain activity may compromise ATP availability and the

energetic status in the PNS from obese and diabetic subjects. Furthermore, structural abnormalities have also been observed in DN. Schwann cells of myelinated and unmyelinated axons of the human sural nerve present enlargement of mitochondria [97]. Axonal swellings containing not only normal but also abnormally enlarged mitochondria have also been described in the sural nerve from a diabetic feline model [98]. Conversely, a decrease in mitochondrial diameter in DRG perikarya was found in 24-week old BKS-*db/db* mice (T2DM) [99] as well as in neurons from sympathetic ganglia in Akita mouse model (T1DM) [100]. In addition, an increase in mitochondrial density in DRG cell bodies [99] and axons [101] from 24-week old BKS-*db/db* was also observed due to activation of mitochondrial fission.

Regarding the role of endoplasmic reticulum in DN, many evidence highlighted how fatty acids impair the ER capacity to store  $Ca^{2+}$ , leading to mitochondrial dysfunction. ER is a complex organelle involved in synthesis, folding and maturation of proteins,  $Ca^{2+}$  storage and lipid biosynthesis. Accumulation of misfolded proteins may occur if protein load overcomes the folding capacity. Under those stressful conditions, an adaptive mechanism known as unfolded protein response (UPR) is triggered to recover homeostasis (**Fig. 14**).

The main role of the UPR is to decrease the unfolded protein load by decreasing protein translation and inducing transcription of chaperones and foldases [102]. Moreover, UPR induces the expression of antioxidant genes since hydrogen peroxide is generated during the folding process [103]. However, if homeostasis is not recovered, prolonged ER stress leads to generation of inflammatory and pro-apoptotic signals.

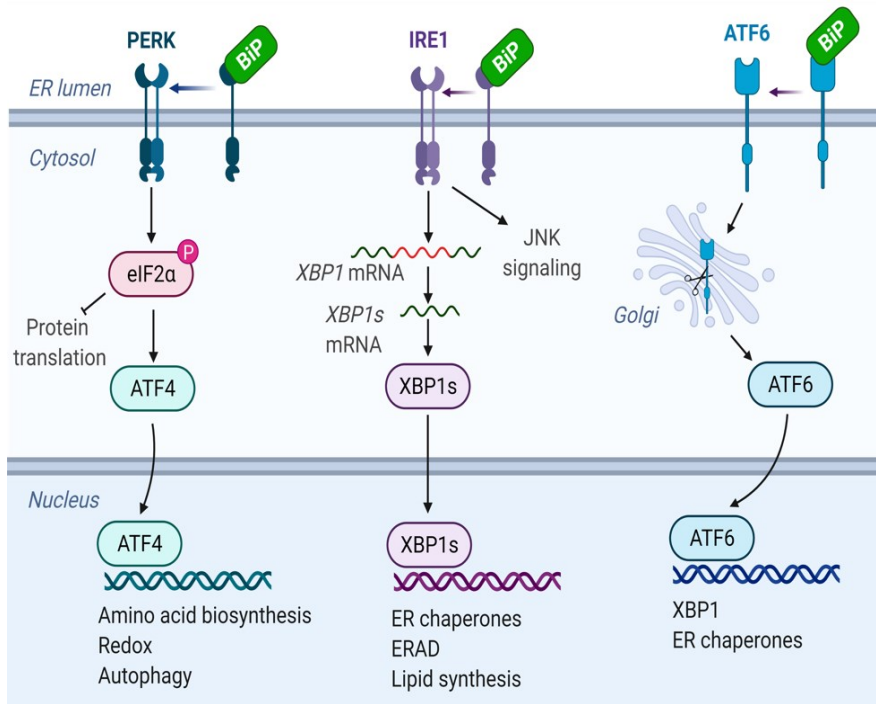


**Figure 14.** PERK, IRE1 and ATF6 pathways involved in UPR.

### 2.5.9. INSULIN AND IGF-1 RESISTANCE

Even though glucose uptake in the PNS is insulin-independent, insulin as well as insulin-like growth factor I (IGF-1) are potent neurotrophic factors that affect the growth, development and maintenance of the system. DRG neurons and Schwann cells express both insulin [104] and IGF-1 receptors [105; 106]. In cultured adult rat sensory neurons, neurite outgrowth is induced by insulin and IGF-1 exposure [107]. Local hindpaw administration of low dose insulin improves skin innervation without affecting glycaemia levels in type 1 and type 2 diabetes models [108]. Furthermore, IGF-1 KO mice show reduced nerve conduction velocities and decreased axonal diameters without affecting myelin thickness [109]. Nonetheless, *in vitro* and *in vivo* studies have demonstrated that IGF-1 is able to promote axon myelination [110-112].

Interestingly, some papers suggest that neurons and glia in the PNS develop insulin resistance, similar to muscle, adipose tissue and liver. Kim et al. [113] found that chronic insulin exposure *in vivo*, using the *db/db* model, lead to blunted insulin signalling cascade after *in vitro* acute insulin stimulation of DRG. Moreover, Grote et al. [114] observed similar results in DRG and sciatic nerves from *ob/ob* mice after insulin or IGF-1 intrathecal injection contrary to what was observed in non-diabetic mice. Therefore, impaired neurotrophic support due to insulin and IGF-1 resistance may also contribute to diabetic neuropathy pathophysiology.

## 2.6. ANIMAL MODELS OF DIABETIC NEUROPATHY

*In vivo* murine models are crucial for understanding diabetic neuropathy pathogenic mechanisms and elucidating new treatment approaches. Unfortunately, no single diabetic mouse recapitulates all the features and complications found in humans. Therefore, the appropriate model should be selected according to the diabetes stage and the degree of obesity under study.

Currently, many T2DM mouse models are available and can be classified as diet-induced, polygenic or monogenic models. The development of DN in these models is multifactorial including duration of diabetes, diet, age, sex and genetic background (strain).

Mice fed a HFD may develop diet-induced obesity (DIO) and prediabetes with hyperinsulinemia and IGT, but not severe hyperglycaemia. To note, mice only develop obesity on a saturated-enriched HFD, whereas unsaturated fat feeding may be protective against obesity [115]. Different studies have researched the role of HFD on neuropathy development, observing that obesity

predisposes mice to low-grade nerve damage even in the absence of T2DM [89; 116]. Thus, it is a good model to mimic the gradual onset of metabolic disturbances typical of human metabolic syndrome. However, some of the drawbacks of DIO models are the non-progression to diabetes and the variability associated with HFD duration and composition.

There are also models carrying a combination of susceptibility alleles that predispose to eventually develop obesity and diabetes. Because of polygenic nature, these models may recapitulate more accurately human T2D than monogenic models with more moderate obesity and mature onset diabetes. Nonetheless, available polygenic models, NONcNZO10/LtJ and TALLYHO/JngJ mice, do not develop neuropathy.

Monogenic mouse models with impaired leptin signalling are the most studied models in diabetic neuropathy research. In the 1970s, Doug Coleman at the Jackson Laboratory used parabiosis to characterise the obese murine models carrying in homozygosis the naturally occurring *ob* and *db* mutations. Results from that study allowed Coleman to hypothesize that *ob/ob* mice may lack a blood factor that participates in body weight regulation and that *db/db* mice may lack its receptor [117].

In 1994, Jeffrey Friedman's laboratory cloned *Ob* gene [118] demonstrating a year later that OB protein functions as an endocrine factor that regulates body fat stores by reducing food intake and increasing energy expenditure [119]. *Ob* gene encodes leptin, a hormone secreted postprandially by adipocytes that controls appetite by hypothalamic signalling. Mutations in either the leptin gene (*ob/ob*) or its receptor (*db/db*) result in compromised leptin

signalling inducing hyperphagia and consequent obesity and diabetes (**Fig. 15**). The severity of diabetes in *ob/ob* and *db/db* mice is strongly influenced by the genetic background of the strain. C57BL/6J strain carrying *ob/ob* or *db/db* mutations develops marked obesity, mild diabetes, hypertrophy and hyperplasia of  $\beta$ -cells, and hyperinsulinemia. Contrarily, both mutations on the C57BL/KsJ lead to obesity and severe diabetes, with transient hyperinsulinaemia followed by islet atrophy [117].

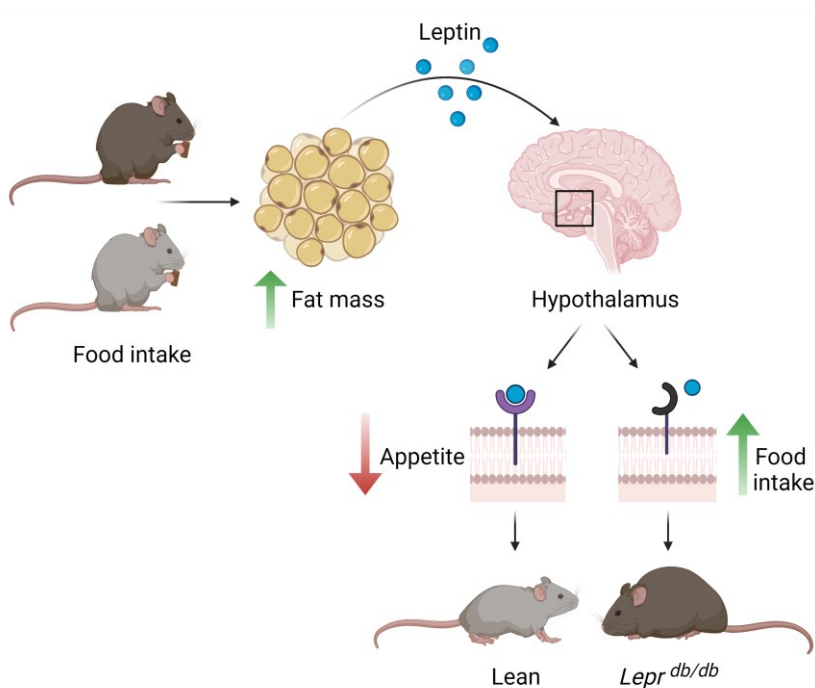


**Figure 15.** Adipocytes enlargement after food intake stimulates leptin secretion which controls appetite by hypothalamic signalling. BKS-*Lepr<sup>db/db</sup>* mouse model exhibits hyperphagia and obesity due to compromised leptin signalling.

Diabetic neuropathy severity is likewise strain-dependent. C57BL/6 *db/db* exhibit mild neuropathy, whereas on the C57BKS background more robust neuropathy is developed [120]. Sima and Robertson [121] were the first to characterise DN in BKS-*db/db*. Electrophysiological studies showed severely decreased motor

nerve conduction velocity with morphometric abnormalities like axonal atrophy and increased fibre density. Thenceforth, many other studies have investigated DN using this model [122].

Nerve damage characterisation in mice carrying the *ob/ob* mutation is much less studied compared to C57BKS-*db/db* with only few studies available. Kosacka et al. [123] found intraepidermal nerve fibre degeneration in foot skin and just low-grade neuropathic abnormalities using C57BL/6 *ob/ob* model.

Therefore, BKS-*db/db* is a better model due to the early onset and more robust nature of neuropathy compared to DIO models. However, some disadvantages are the absence of prediabetes and indirect consequences of impaired leptin signalling [124]. In addition, females homozygous for the mutation are infertile while males exhibit a reduced ability to mate which could hinder obtaining enough animal numbers and make them much more expensive than regular mouse models.

## 2.7. CURRENT TREATMENTS OF DIABETIC NEUROPATHY

Nowadays, there is no cure for diabetic neuropathy rather than lifestyle changes, strict glycaemic control, and management of neuropathic pain [49]. Diet and exercise have shown some improvements in neuropathy outcomes, including increased intraepidermal nerve fibre density (IENFD) and reduced neuropathic pain [125-127]. However, glucose control alone in type 2 diabetic patients has shown modest effect on preventing DN in large clinical trials [128]. This phenomenon may be in part related to other risk factors independently associated with diabetic neuropathy as, for instance, obesity [73]. In addition, it has been recently suggested

that complications develop after sufficient glycaemic exposure by either a greater exposure for a relatively short time or a milder exposure for a longer period. Thus, improved HbA1c as a result of intensive insulin treatment only delays the development of diabetic complications [129]. Furthermore, even with pancreas transplantation, DN progression is only improved but not completely reversed [130].

Regarding neuropathic pain, the American Diabetes Association has recently published a guideline to manage pain associated with diabetic neuropathy. Once painful DN is confirmed, first-line and second-line treatments include several types of drugs, such as anticonvulsants (pregabalin), serotonin-noradrenaline reuptake inhibitors (duloxetine), and secondary amine tricyclic antidepressants (nortriptyline, desipramine). Based on comorbidities, potential adverse effects, drug interactions and costs one of these treatments is selected as first-line treatment. If no clinically meaningful effect is observed, another agent is chosen as a second-line treatment, or alternatively, a combination of agents is prescribed. Opioids (tapentadol and tramadol) have demonstrated effectiveness in the treatment of neuropathic pain. Nonetheless, a high risk of addiction, abuse and sedation may prevent their prescription unless other treatments fail [49].

Several other drugs have been tested in preclinical models and humans to treat diabetic neuropathy. For instance, antioxidant molecules, such as alpha-lipoic acid, have been extensively tested in clinical trials to counteract oxidative stress. Although just modest improvements in some neurological parameters were observed, alpha-lipoic acid may be a valuable therapeutic option in patients with early neuropathic symptoms [131]. Other treatments, however,



have failed to demonstrate a relevant improvement. For example, even though Benfotiamine reduces AGEs formation, no positive results were observed in a phase III clinical trial for diabetic neuropathy [132]. Aldose reductase inhibitors have also been studied since many years ago, but have failed to meet regulatory requirements to be approved by the FDA or EMA, even though one of them, epalrestat, is marketed in Japan for the treatment of DN in geriatric populations [133].

### 3. GENE THERAPY

The main problem of conventional drug administration for the treatment of neurological disorders is the short-term effect of this kind of drugs and limited bioavailability in target tissues due to blood-brain barrier in the CNS or blood-nerve barrier in the PNS. Consequently, higher amounts of drugs need to be administered to reach these tissues at the appropriate concentration, thus increasing adverse side effects. To overcome these issues, gene therapy approaches are alternative therapeutic options that offer greater specificity and long-term effect. Thus, gene therapy has a great potential to treat monogenic diseases as well as multifactorial disease as diabetes and diabetic neuropathy.

The main goal of gene therapy is to transfer a genetic material into cells to treat or prevent a disease. Depending on the aetiology of the disorder, gene therapy strategies could be based on transgene addition, endogenous gene correction, or gene silencing.

Therapeutic gene should be introduced in a vector to be efficiently transferred to the target cell. Two main groups of vectors can be differentiated according to their origin: viral vectors derived from

viruses and non-viral vectors such as plasmid DNA. Non-viral vectors offer low immunogenicity and limitless packaging capacity. However, its reduced efficiency to transfect cells makes it an undesirable choice for most *in vivo* approaches. Conversely, viral vectors represent a great tool to successfully transduce cells taking advantage of the natural ability of virus to infect cells. Viral vectors design implies to replace all pathogenic genes with the therapeutic gene while keeping the viral capsid. Therefore, viral vectors are non-pathogenic gene vehicles that maintain the same tropism as the parental virus [134].

### 3.1. ADENO-ASSOCIATED VIRAL VECTORS

Currently, viral vectors could derive from many viruses such as adeno-associated virus, adenovirus, lentivirus, retrovirus, etc. Among all the viral vectors available, adeno-associated virus (AAV) vector is the most widely used in the gene therapy field for long-term expression of therapeutic proteins. Proof of that is the approval of three different therapeutic strategies using AAV as well as over 100 ongoing clinical trials using this vector. In 2012, Glybera was the first AAV therapy approved in Europe for the treatment of lipoprotein lipase deficiency. In 2017, Luxturna for the treatment of Leber's congenital amaurosis was approved by the FDA as well as Zolgensma for the treatment of spinal muscular atrophy in 2019.

Adeno-associated virus belongs to the *Parvoviridae* family consisting of small, nonenveloped viruses with a single-stranded DNA (ssDNA) genome of ~4.7 kb packaged in an icosahedral capsid. AAV viruses need a helper virus, like adenovirus, to complete a replication cycle. Indeed, adenoviral proteins participate

in each step of AAV cycle including nuclear translocation, transcriptional activation, translation and DNA replication [135]. For that reason, a helper plasmid containing these genes is needed to produce AAV *in vitro*.

AAV genome contains two genes *Rep* and *Cap* flanked by two palindromic inverted terminal repeats (ITR). *Rep* encodes four proteins (Rep78, Rep68, Rep52, Rep40) involved in replication and packaging of AAV genome. Moreover, Rep proteins also participate in the insertion of AAV genome in 19q13 locus. *Cap* gene encodes three proteins that assemble the capsid (VP1, VP2 and VP3, in approximately a 1:1:10 ratio) and two accessory proteins (AAP, MAAP) (Fig. 16).

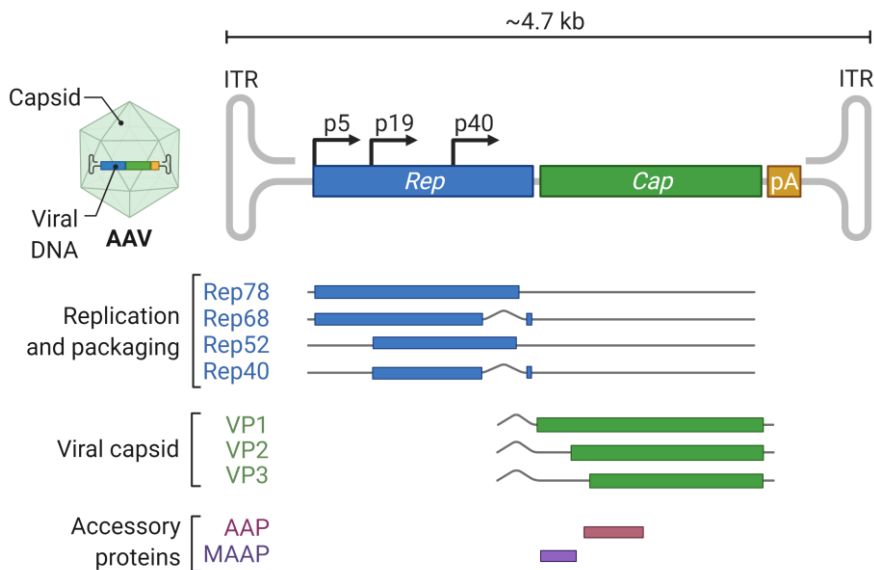


**Figure 16.** Adeno-associated virus genome containing *Rep* and *Cap* genes flanked by ITRs.

AAV interaction with cellular receptors triggers a cascade that results in AAV endocytosis, intracellular trafficking, nuclear import and genome release. Once released, ssDNA is converted to double-

stranded DNA (dsDNA) (**Fig. 17**). The absence of helper virus leads to dsDNA integration establishing a latent state. On the contrary, helper virus coinfection promotes AAV genome replication and production of AAV virions.

*Rep* and *Cap* genes are completely removed and replaced with the transgene of interest to produce an AAV-based vector. Since Rep proteins are missed in the AAV vector, transgene constructs are neither replicated nor inserted into the 19q13 locus, but mainly remain as linear or circular episomal concatamers associated with high molecular weight DNA, enabling its long-term expression in non-dividing cells (**Fig. 17**) [136-138].

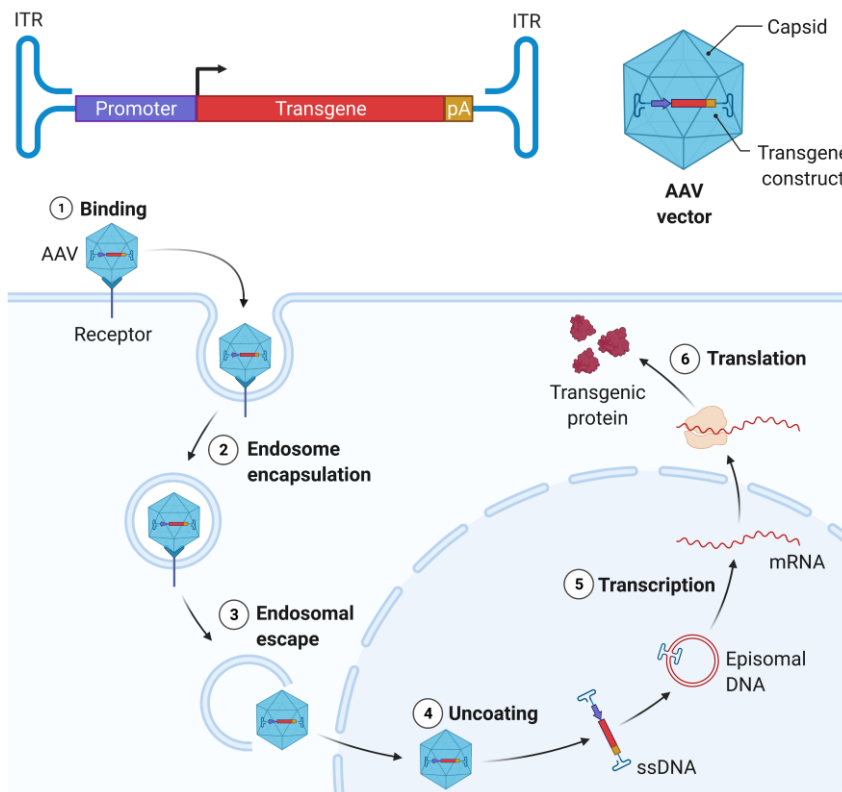


**Figure 17.** Structure of transgene construct and life cycle of AAV vector.

Since ITRs are necessary for replication and packaging of wild-type (wt) AAV genome, the design of therapeutic constructs implies flanking the transgene with ITRs. In addition, *Rep* and *Cap* genes are provided *in trans* to produce AAV vectors *in vitro*.

Even though wtAAV has not been associated with any disease, neutralizing antibodies against AAV capsids could be found in a large proportion of the human population resulting from successive infections. Indeed, wtAAV has been detected in many different human tissues [139]. Pre-existing immunity represents a great concern in the outcome of human clinical trials. On the one hand, neutralization of viral capsids may limit the efficient transduction of target cells. On the other hand, immune response could trigger toxicity in those patients treated with high doses of AAV vector [140; 141]. In addition, neutralizing antibodies raised in patients treated with AAV gene therapy vectors may prevent vector re-dosing. Therefore, treatment of patients without pre-existing immunity would be desirable. However, when that is not feasible, administration of immunomodulatory regimens could turn into a promising strategy to enable vector re-dosing and avoid toxicity associated with high viral cargo [142]. Moreover, removal of most AAV genome and using tissue specific promoters contributes to reduce the immunogenicity.

Other issue to take into consideration is the possibility of toxicity associated with long-term expression of the transgene. While in most cases, continual expression of the transgene by using a constitutive promoter is harmless, severe toxicity may arise in others. For instance, a recent paper described that long-term AAV9-mediated SMN overexpression induces motor dysfunction associated with neurodegeneration in a model of spinal muscular atrophy [143]. Therefore, strategies to control the expression of the transgene by

using inducible promoters or, more recently, drug-induced splicing technology may be desirable for some therapeutic approaches [144].

### 3.2. GENE THERAPY APPROACHES TARGETING PNS

The combination of several naturally occurring and engineered serotypes with different tropisms with distinct administration routes such as direct injections, intravenous administration and intrathecal puncture have demonstrated the ability to reach the nervous system, including the PNS.

Direct injections into the DRG and sciatic nerve have been tested in preclinical models showing high transduction efficiency at the injection site. Nonetheless, transgene expression decreased with the distance from the administration point [145-147]. Hence, its clinical applicability is very limited since local effectiveness implies that multiple injections must be performed to obtain a whole correction of the pathology. In addition, the invasiveness of the technique implies safety concerns that prevents its usage in human practice [148].

Since some AAV, such as AAV9, are able to cross the brain blood barrier from the systemic circulation, intravenous injection of AAV vectors is a non-invasive approach that may be useful to target CNS and PNS [149-151]. Nevertheless, some issues are associated with this approach. Firstly, some reports described a shift toward mostly glial cells transduction when adult mice and nonhuman primates were used rather than neurons. Secondly, neutralizing antibodies are a clear drawback for this type of administration limiting transduction efficiency. Thirdly, the need to load extremely high titers of vectors, with the consequent safety concerns, and lastly, high

tropism of AAV vectors for liver which represents another barrier to target the nervous system from system circulation [152; 153].

On the contrary, lumbar intrathecal administration is a clinically translatable approach to target the PNS that can be performed in an outpatient setting, with higher efficiency or less invasive than the methods previously described, and moreover, allows to evade the effects of neutralizing antibodies [154; 155]. Compared to other serotypes (AAV2, 5, 6, 8), AAV9 and AAVrh10 injected intrathecally have higher efficiency transducing DRG from mice and nonhuman primates [112; 156-159].

### 3.2.1. GENE THERAPY FOR DIABETIC NEUROPATHY

Currently, most gene therapy approaches in preclinical models have used neurotrophic and angiogenic factors as a treatment for DN. For instance, the effect on DN of IGF-1, secretoneurin, neurotrophin-3 and nerve growth factor have been explored [112; 160-162]. In addition, a gene therapy product developed by Helixmith is currently in phase III for the treatment of painful diabetic neuropathy in the US. Engensis (VM202) is a plasmid DNA designed to express two isoforms of hepatocyte growth factor that is delivered by intramuscular injections using non-viral methods. At the present time, moderate pain relief has been reported, but more studies must be conducted in the near future [163]. Unfortunately, these treatments only partially ameliorate or delay neuropathy progression. Consequently, therapeutic approaches focus on the underlying mechanisms of diabetic neuropathy may be required to reach clinically meaningful effect, for this, a better understanding of the diabetic neuropathy pathophysiology needs to be approached.

# ***OBJECTIVES***





Diabetic neuropathy is the most common and debilitating complication of diabetes with a huge clinical and economic burden. Nevertheless, no effective treatment is currently available. Over the past decade, high-throughput gene expression profiling technologies and, more recently, metabolomics have enabled to study the molecular landscape of the peripheral nervous system of diabetic murine models and diabetic patients [72; 164; 165]. However, there are no studies exploring the effect of T2DM on the PNS proteome. Since poor correlation between transcriptomics and proteomics has been demonstrated [166], a multi-strategy approach that includes the analysis of the proteome would be essential to fully characterise diabetic neuropathy.

For that reason, the main purpose of this work is to characterise the PNS proteome under metabolic syndrome aiming to gain further understanding of the pathogenic mechanisms of the disease and to elucidate new therapeutic approaches.

As previously presented, BKS-*Lep<sup>db/db</sup>* mouse is the most studied model of diabetic neuropathy in T2DM research. Indeed, most omics studies have been conducted using this model. Thus, we chose the *db/db* model for proteomic analysis to facilitate further comparisons with previous studies.

In addition, even though neuropathic phenotype has been already demonstrated in *db/db* mouse, we considered that further neuropathic evaluation performed in our hands would be necessary, before proteomic analysis, to show evidence of DN in the animals, taking into account the inherent variability associated with the metabolic nature of the disease.

To address these aims, the following objectives have been established:

1. To fully evaluate the metabolic and neuropathic profile in BKS-*db/db* mouse model along the progression of the disease.
2. To characterise the dorsal root ganglia and sciatic nerve proteome before development of established neuropathy.
3. To analyse new promising targets to design therapeutic approaches.

# ***RESULTS***



## 1. METABOLIC PROFILE OF BKS-*Lep<sup>db/db</sup>* MICE

Throughout the development of this thesis six batches of animals have been used for multiple purposes including metabolic profiling, neuropathic evaluation, proteomic characterisation and gene therapy testing. Male BKS-*Lep<sup>db/db</sup>* were used as well as lean littermates (BKS-*Lep<sup>+/+</sup>*) as control animals for all experiments. We chose males over females since it has been described that male *db/db* mice develop a more severe form of neuropathy [167]. Breeding scheme of animal supplier maintains *Lep<sup>db</sup>* allele in repulsion with *Dock7<sup>m</sup>* allele (misty mutation). Thus, *db/db* mouse presents a black coat, whereas lean control (*dock7<sup>m/m</sup>*) a misty fur.

We established a glycemia value above 250 mg/dL to consider diabetes onset. Thus, animals with glycaemia below this value were not included in further studies. The *db/db* mice develop obesity from 4-5 weeks of age resulting from its hyperphagic phenotype leading to insulin resistance and consequent hyperglycaemia at 4-8 weeks of age. Despite the onset of diabetes differs among animals, ninety four percent of *db/db* mice exhibited diabetes at 9 weeks of age.

*Lep<sup>db/db</sup>* mice showed progressive increase in weight and glycaemia reaching values over 50 g and 600 mg/dL, respectively (**Fig.18**). Interestingly, we observed in all batches studied that *db/db* mice started to lose weight around 13 weeks after diabetes onset despite sustained hyperglycaemia, high levels of fructosamine and serum FFA, as well as huge deposition of visceral fat (**Table 4, Fig. 19**). Despite measure of Hba1c is routinely performed in human, fructosamine testing is more commonly used in veterinary practice and it results from glycation of serum proteins enabling to monitor glycaemia status over 2-3 weeks prior testing.

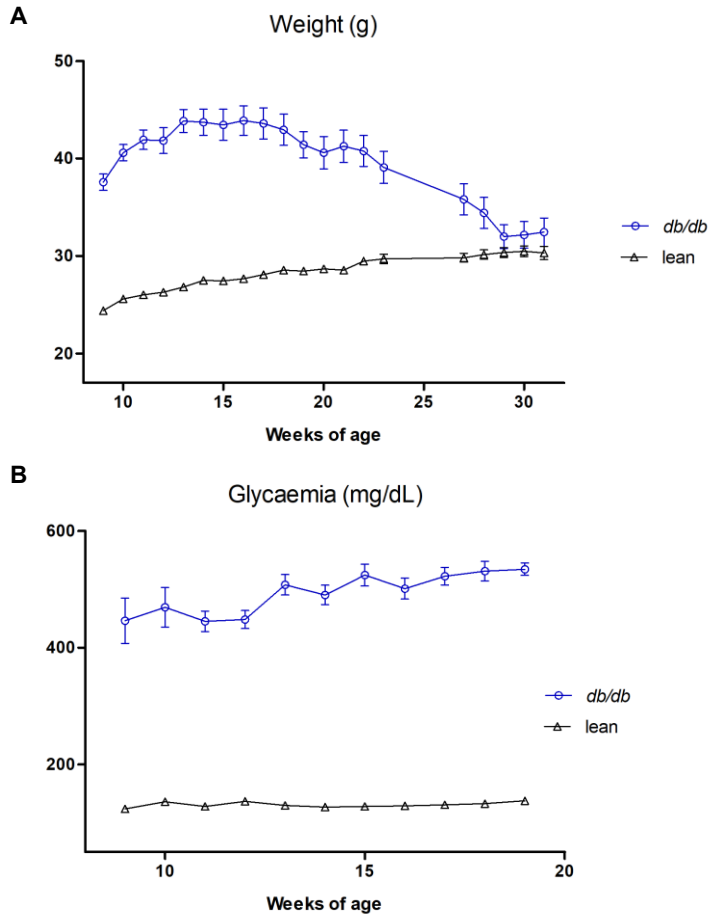


**Figure 18.** Weekly measurements of body weight (**A**) and glycaemia (**B**) in BKS-*db/db* (blue) and BKS-lean (black) mice to monitor obesity and diabetes progression. N = 8-12 animals per group.

**Table 4.** Body weight and glycaemia comparison between male *db/db* mice with 15 and 25 weeks of diabetes and lean control before euthanasia. N = 6-9 animals per group. \*\*\*\*p < 0.0001, by Student's T test.

	lean	<i>db/db</i>
<b>Weeks of age</b>	21	21
<b>Weeks with diabetes</b>	-	15
<b>Body weight (g)</b>	27.85 ± 0.80	37.83 ± 1.48****
<b>Fasting blood glucose (mg/dL)</b>	177.78 ± 9.87	HI (>600 mg/dL)
<b>Weeks of age</b>	31	33
<b>Weeks with diabetes</b>	-	25
<b>Body weight (g)</b>	30.33 ± 2.12	29.93 ± 3.47ns
<b>Fasting blood glucose (mg/dL)</b>	188.6 ± 6.39	523.4 ± 17.46****

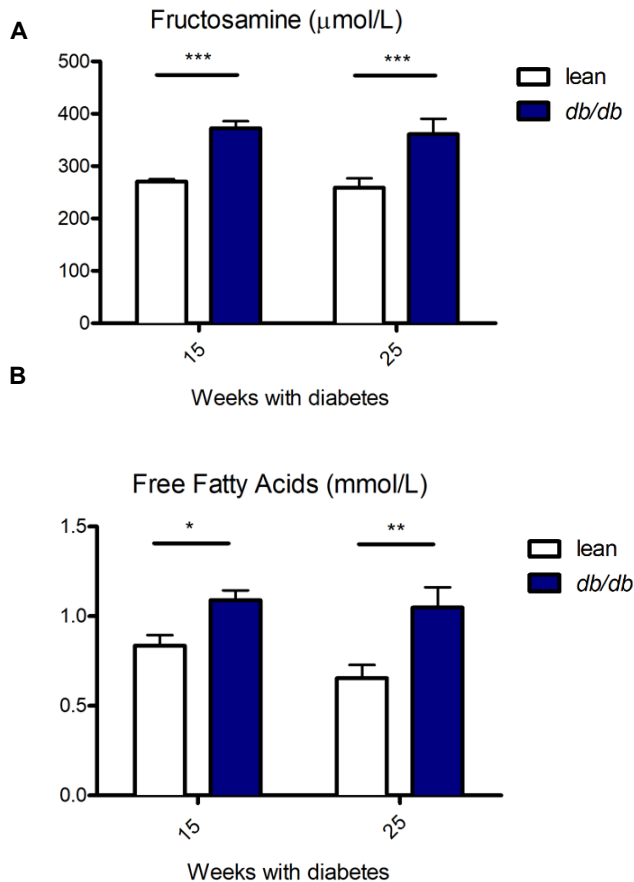


**Figure 19.** Fructosamine (**A**) and free fatty acid (**B**) measurements in *db/db* (blue) mice with 15 and 25 weeks of diabetes compared to lean (white) animals. N = 6-9 animals per group. \*p < 0.05, \*\*p < 0.01, \*\*\*p < 0.001, by Student's T test.

## 2. NEUROPATHY EVALUATION IN BKS-*Lep<sup>db/db</sup>* MICE

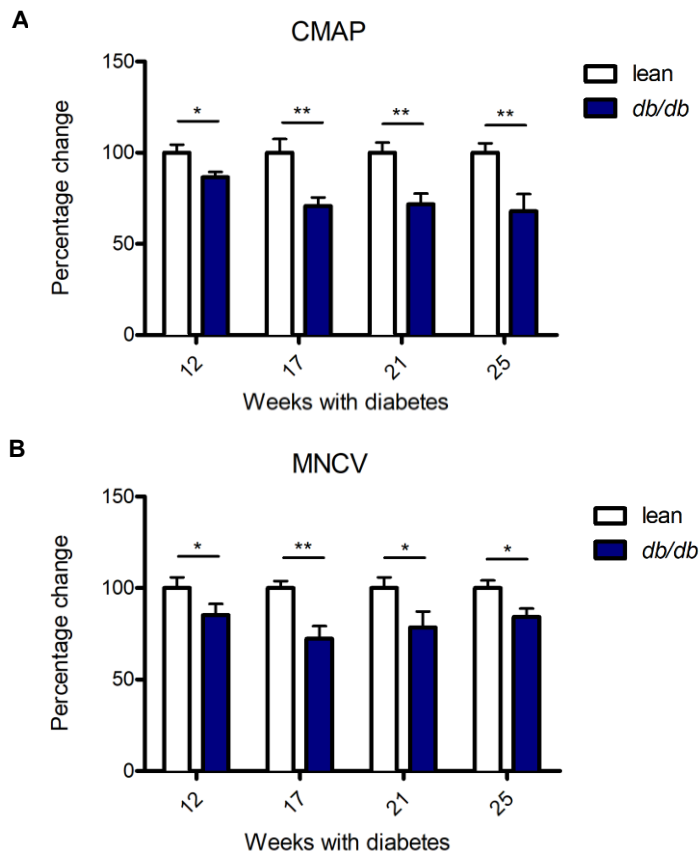
Concurrently, we evaluated neuropathy by multiple approaches comprising electrophysiological tests, nerve morphometry, cutaneous innervation and sweating activity.

Electrophysiological testing enables to distinguish whether nerves experiment demyelination, axonal degeneration or both pathological features. Aiming to characterise the abnormalities of diabetic nerves



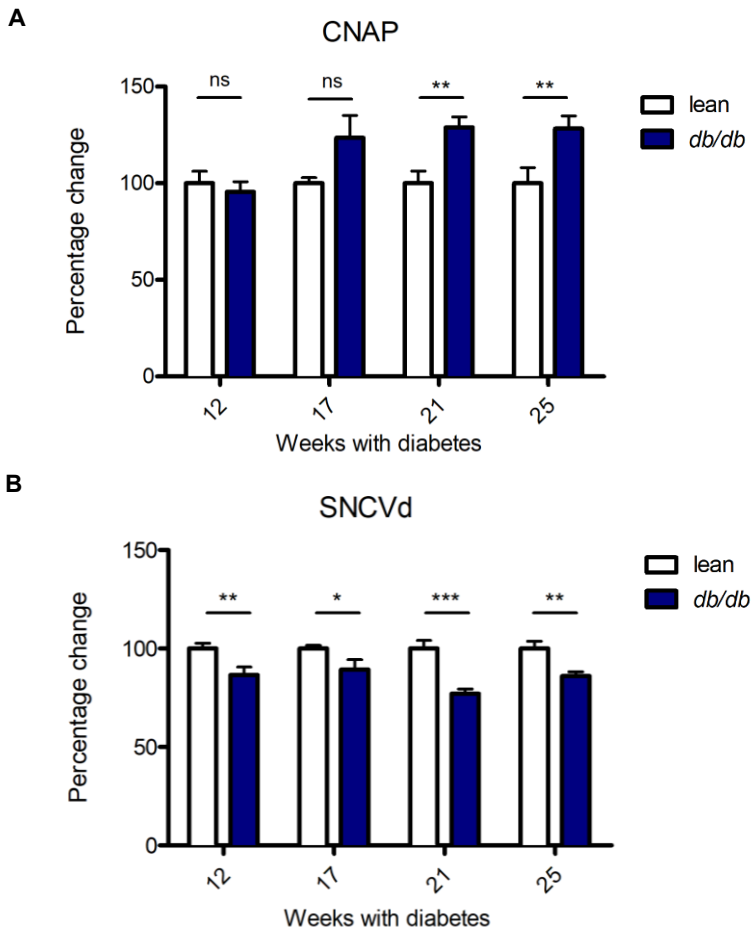
we performed conduction tests after 12, 17, 21 and 25 weeks with diabetes in the sciatic and caudal nerves.

We observed a consistent decline in compound muscle action potential (CMAP) amplitude as well as lower motor nerve conduction velocity (MNCV) in sciatic nerve from the first time point analysed (12 weeks). These observations may be indicative of both motor axonal atrophy and demyelination, respectively. For the time frame analysed, we did not see a progressive deterioration, but a steady neuropathic phenotype along the course of diabetes (**Fig. 20**).



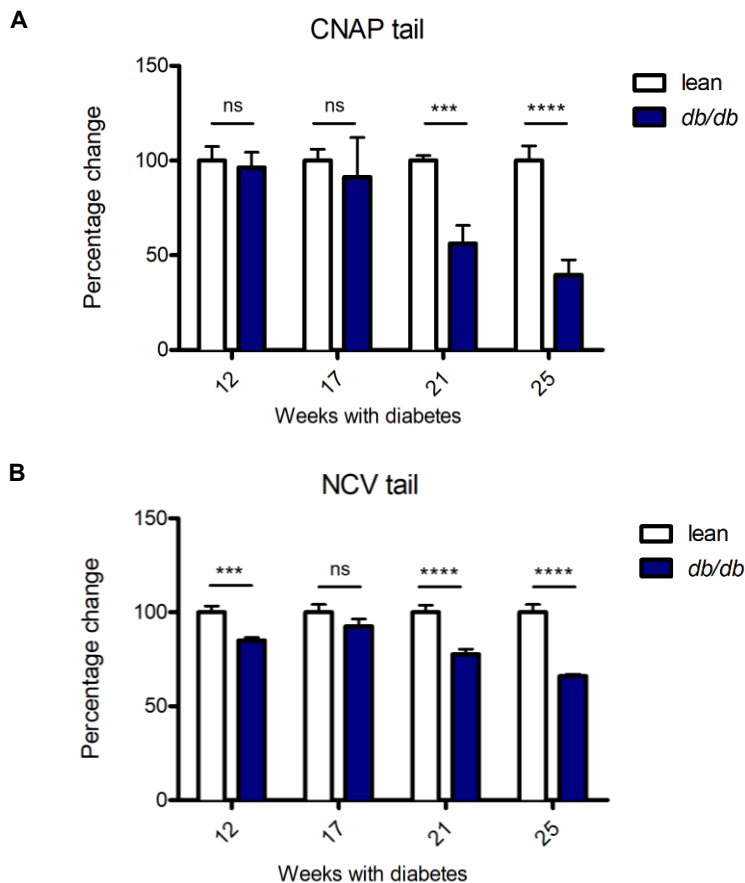
**Figure 20.** Evaluation of compound muscle action potential (**A**) and motor nerve conduction velocity (**B**) by electrophysiological study of the sciatic nerve at 12, 17, 21 and 25 weeks with diabetes. Data are expressed as percentage of change compared to lean mice. N = 7-13 animals per group. \*p < 0.05, \*\*p < 0.01, by Student's T test.

Regarding sensory nerve fibres in sciatic nerve, compound nerve action potential (CNAP) amplitude was found, unexpectedly, increased since 17 diabetic weeks. On the other hand, distal sensory nerve conduction velocity (SNCVd) was declined to the same extent as MNCV also demonstrating a demyelinating phenotype of these fibres. As observed for motor fibres, it does not seem that a gradual degeneration occurs along time (**Fig. 21**).



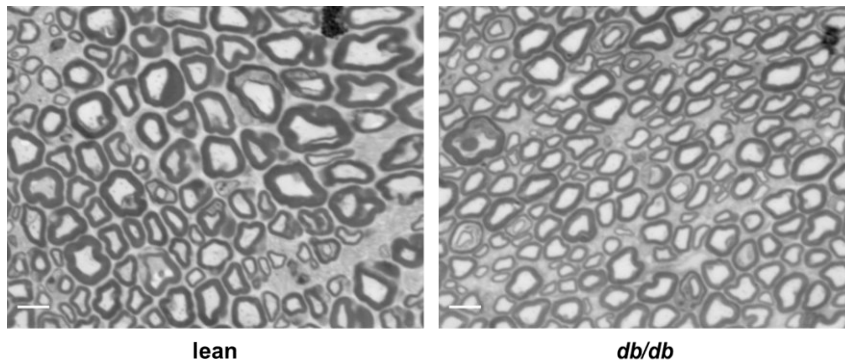
**Figure 21.** Evaluation of sensory compound nerve action potential (**A**) and distal sensory nerve conduction velocity (**B**) by electrophysiological study of the sciatic nerve at 12, 17, 21 and 25 weeks with diabetes. Data are expressed as percentage of change compared to lean mice. N = 7-13 animals per group. \*p < 0.05, \*\*p < 0.01, \*\*\*p < 0.001, by Student's T test.

Interestingly, when we analysed the caudal nerves from the tail, we observed a progressive and more noticeable drop in sensory CNAP and nerve conduction velocity (NCV) compared with parameters studied in the sciatic nerve (**Fig. 22**). Therefore, electrophysiological tests may indicate that although same pathological abnormalities in sciatic nerve were detected, a more pronounced phenotype was exhibited in caudal nerves. This observation is consistent with the distal-to-proximal degeneration characteristic in distal polyneuropathy.



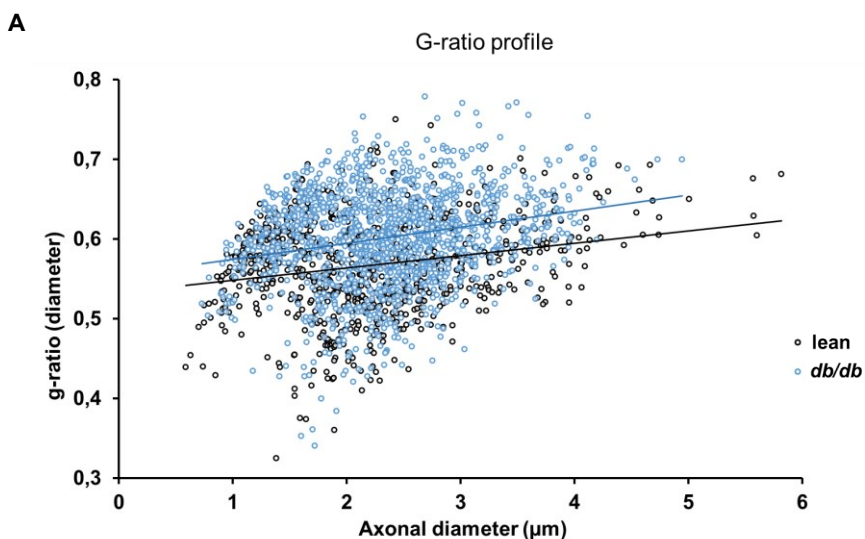
**Figure 22.** Evaluation of sensory compound nerve action potential (**A**) and sensory nerve conduction velocity (**B**) by electrophysiological study of the caudal nerves at 12, 17, 21 and 25 weeks with diabetes. Data are expressed as percentage of change compared to lean mice. N = 7-13 animals per group. \*\*\*p < 0.001, \*\*\*\*p < 0.0001, by Student's T test.

Additionally, we characterised the tibial nerve by morphometric analysis to correlate electrophysiological alterations with structural changes (**Fig. 23**). Based in previous experience in our laboratory and already published bibliography, we analysed the tibial nerve in *db/db* mice after 25 weeks with diabetes (previous time points did not show any structural difference).



**Figure 23.** Representative micrographs of 0.7  $\mu\text{m}$  semithin sections of tibial nerves from lean and *db/db* mice (25 weeks with diabetes) stained with toluidine blue. Scale bar = 5  $\mu\text{m}$ .

Firstly, tibial nerves from diabetic mice showed a higher g-ratio (axonal /fibre diameter) due to thinner myelin which may correspond to the decline observed in nerve conduction velocities (**Fig. 24**).



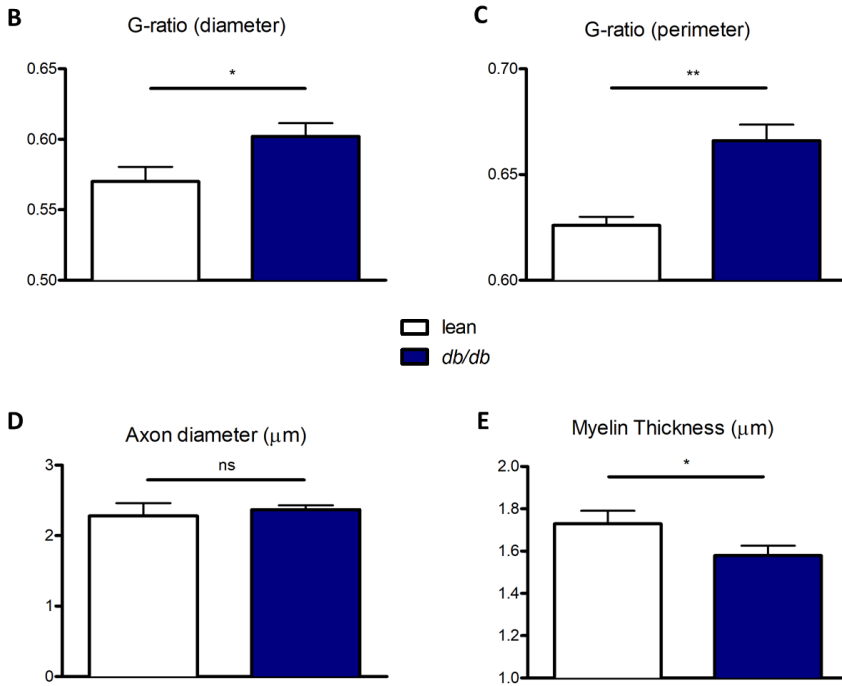


**Figure 24.** (A) Representation of G-ratio (axonal diameter/fibre diameter) versus axonal diameter ( $\mu\text{m}$ ) profile from the whole set of analysed nerve fibres. (B, C, D, E) Morphological parameters from semithin sections of tibial nerves including G-ratio (diameter), G-ratio (perimeter), axonal diameter and myelin thickness. N = 3 lean and 5 *db/db* (25 weeks with diabetes). \* $p < 0.05$ , \*\* $p < 0.01$ , by Student's T test.

Interestingly, increased number of myelinated fibres as well as higher density were demonstrated in diabetic mice compared to lean animals (Fig. 25).

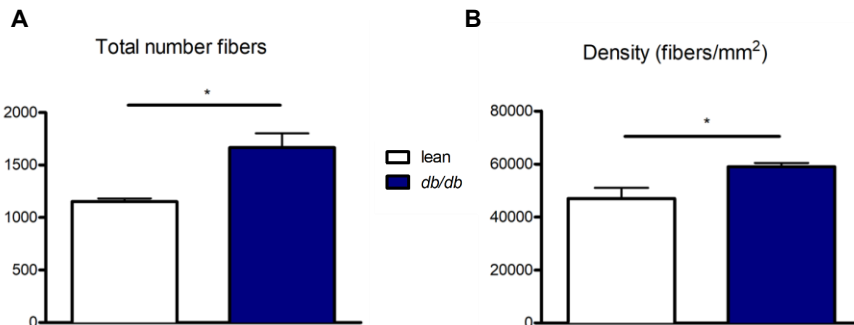


**Figure 25.** Quantification of total number of myelinated fibres (A) and fibre density (B) in tibial nerves from lean and *db/db* animals (25 weeks with diabetes). N = 3 lean and 5 *db/db*. \* $p < 0.05$ , by Student's T test.

In addition, larger and smaller fibres decreased their frequency, whereas fibres of 3-4.99  $\mu\text{m}$  are more common in diabetic nerve (**Fig. 26**). Therefore, these changes may indicate a degeneration of larger fibres followed by a regenerative sprouting that increases the number and density of smaller myelinated fibres. Moreover, higher fibre density may explain why sensory CNAP was higher in diabetic animals.

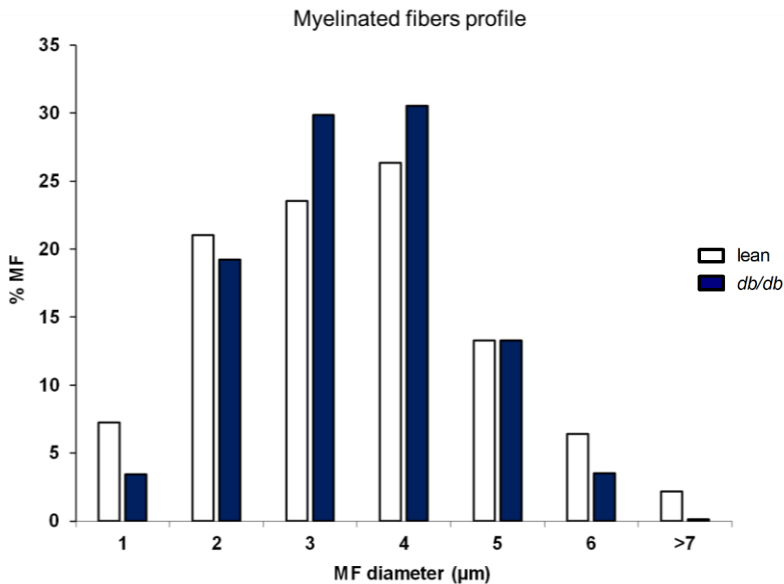


**Figure 26.** Histogram of the distribution of myelinated fibres of tibial nerves according to diameter in the lean group and the *db/db* group after 25 weeks with diabetes. N = 3 lean and 5 *db/db*.

Autonomic neuropathy is a frequent complication of diabetes mellitus that often is concomitant or even preceding of sensory-motor neuropathy [47]. Thus, we evaluated the sympathetic sudomotor function in BKS-*db/db* mice using pilocarpine and the silicone imprint technique after 13 weeks with diabetes. By subcutaneous injection of pilocarpine, a cholinergic agonist, we were able to directly stimulate the muscarinic receptors of sweat glands. In addition, silicone mould retains the impressions of sweat droplets

as they emerged from the sweat duct enabling their quantification. We confirmed that sweat glands from *db/db* mice are able to respond to pilocarpine stimulation. Nonetheless, the number of active sweat glands and the sweat output per gland is lower compared to lean mice (**Fig. 27**).

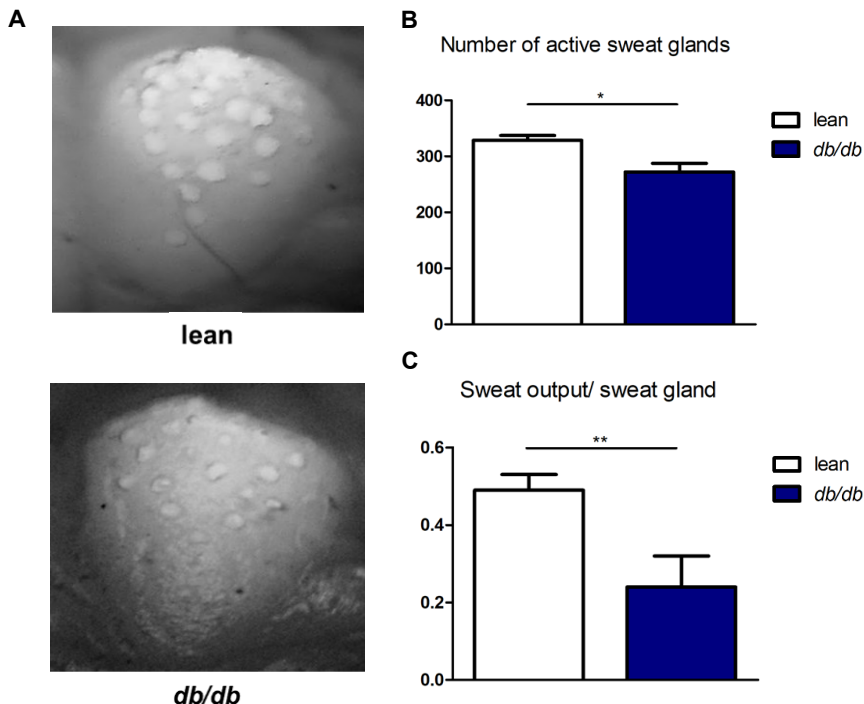


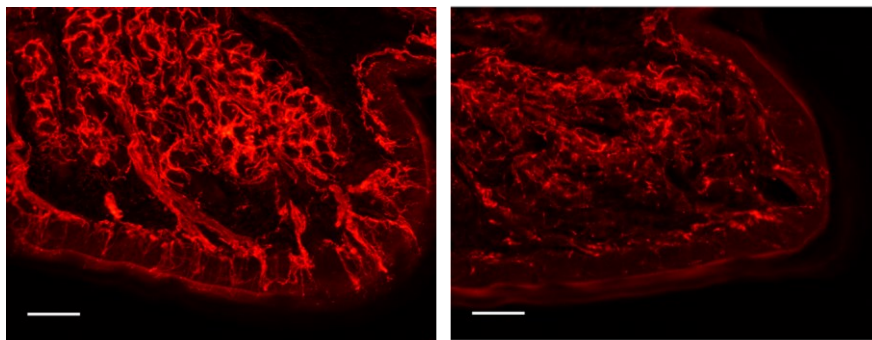
**Figure 27.** (A) Photographs of representative silicone moulds of one footpad with retained impressions of sweat droplets at 10 minutes after pilocarpine administration in *db/db* (13 weeks with diabetes) and lean mice. (B, C) Quantification of number of active sweat glands (sweat droplets number) and sweat output per sweat gland (sweat droplets diameter) from silicone moulds at 10 minutes after pilocarpine administration. N = 13 animals per group. \* $p < 0.05$ , \*\* $p < 0.01$ , by Student's T test.

It is well known that fully denervated glands, in mice and humans, does not result in hypersensitivity response (Cannon's law), but they become unresponsive to pilocarpine, acetylcholine and adrenaline. Conversely, partial denervation of sweat glands does not prevent them from sweating after stimulation, although lower sweat output per gland is produced [47; 168]. Therefore, lower number of active

sweat glands might result from fully denervation of some glands, whereas reduced sweat output per sweat gland could be explained by partial denervation of still responsive glands.

To confirm that changes in sudomotor function were related to the loss of innervation of sweat glands, we performed an immunohistochemistry of footpads using the pan-Neuronal marker PGP9.5 after 15 weeks with diabetes. We observed that *db/db* mice showed a significant loss of sweat gland innervation accompanied by reduction in gland area, which may be an indicative of some gland atrophy (**Fig. 28**).

**A**

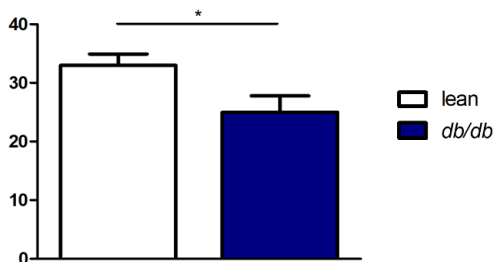


lean

*db/db*

**B**

Innervation of sweat gland area (%)



**C**

Sweat gland area ( $\mu\text{m}^2$ )

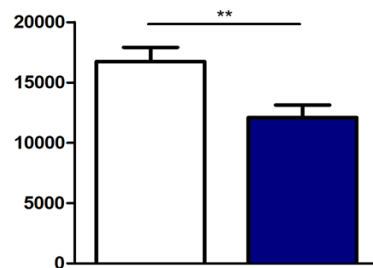


**Figure 28.** (A) Representative fluorescence images of PGP9.5-immunostained plantar pads from lean and *db/db* animals (15 weeks with diabetes). (B, C) Quantification of the innervation percentage and the area of sweat glands from PGP9.5-immunostained footpads. N= 8 lean and 7 *db/db*. \* $p < 0.05$ , \*\* $p < 0.01$ , by Student's T test. Scale bar = 100  $\mu\text{m}$ .



In addition, we quantified the IENFD in the plantar pads to evaluate the degeneration of free nerve endings of small-calibre A $\delta$  and C fibres. Using PGP9.5 immunostaining, we observed a clear reduction in the number of intraepidermal fibres per mm after 15 weeks with diabetes confirming distal neuropathy of small diameter fibres (**Fig. 29**).

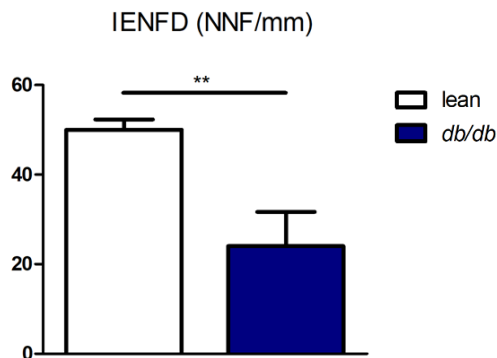


**Figure 29.** Quantification of nerve fibre density (number of nerve fibres (NNF)/mm) of the epidermal layer from PGP9.5-immunostained footpads of lean and *db/db* mice (15 weeks with diabetes). N= 11 animals per group. \*\*p < 0.01, by Student's T test.

Considering all these data, we decided to characterise PNS proteome after 15 weeks with diabetes before established neuropathy was observed. The rationality behind this decision was to analyse which molecular alterations precede the development of profound diabetic neuropathy to, eventually, develop a therapeutic approach.

### 3. ANALYSIS OF DRG AND SCIATIC NERVE PROTEOME

Lumbar dorsal root ganglia and sciatic nerve from *db/db* mice after 15 weeks with diabetes were selected to study proteomic alterations in diabetic PNS. Once these tissues were harvested, we followed the workflow presented in **Figure 30**.

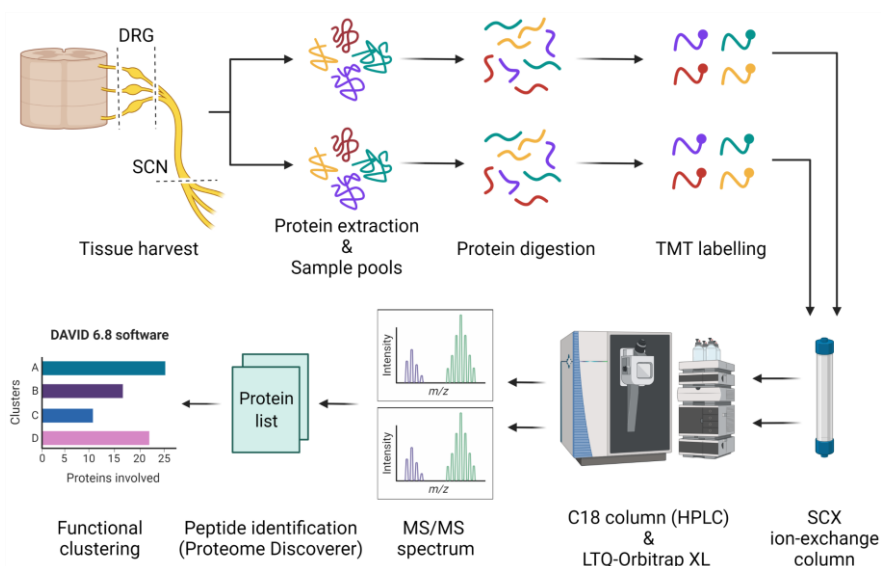


**Figure 30.** Proteomic analysis workflow: **1.** DRG and SCN harvest from *db/db* (at 15 weeks with diabetes) and lean control mice. **2.** Protein lysates obtention and sample pooling in pairs. **3.** Sample pools digestion and labelling using TMTsixplex™ reagents to enable multiplex quantification. **4.** Sample fractionation using a SCX ion-exchange column to reduce sample complexity. **5.** Sample injection to the high-resolution mass spectrometer LTQ-Orbitrap XL through a C18 high-performance liquid chromatography (HPLC) column. **6.** Peptide identification from MS/MS spectrum using Proteome Discoverer software. **7.** Functional clustering of proteins identified to elucidate biological meaning.

Since the amount of protein extracted from DRG or SCN was relatively low, we decided to make sample pools by mixing protein extracts from two animals. Thus, enough protein amount was available for further experiments. It is also remarkable that each digested pool was labelled using different TMT reagent enabling

multiplex relative quantitation of proteins from different samples in a single-run analysis.

Proteomic study of DRG identified 12,430 mass spectra of unique peptides (3199 non-redundant peptides) defining 866 proteins. On the other hand, mass spectrometry allowed us to quantify 12461 mass spectra (3769 non-redundant peptides) defining 843 proteins for SCN. DanteR software determined 286 and 312 differentially expressed proteins for DRG and SCN, respectively, between *db/db* and lean animals. Regarding DRG, 185/286 proteins were upregulated and 101 downregulated. Of those, 68 proteins showed ratios higher than 1.2, whereas 31 proteins were downregulated below ratios of 0.8. Concerning SCN, 217/312 proteins were increased, 117 of which with a ratio higher than 1.2 and 95 were downregulated, 57 with a fold change lower than 0.8. Raw data are included in the annex section (**Annexed table 1, 2**).

Once list of differentially expressed proteins was obtained, we analysed data with different bioinformatic resources as well as by manual literature search to elucidate functional understanding and biological meaning. Firstly, we used WebGestalt (WEB-based Gene SeT AnaLysis Toolkit), a functional enrichment analysis web tool, to characterise protein localization based on subcellular categories from Gene Ontology (GO). As expected, we observed a wide distribution of proteins throughout cell compartments for both tissues (**Fig. 31**).

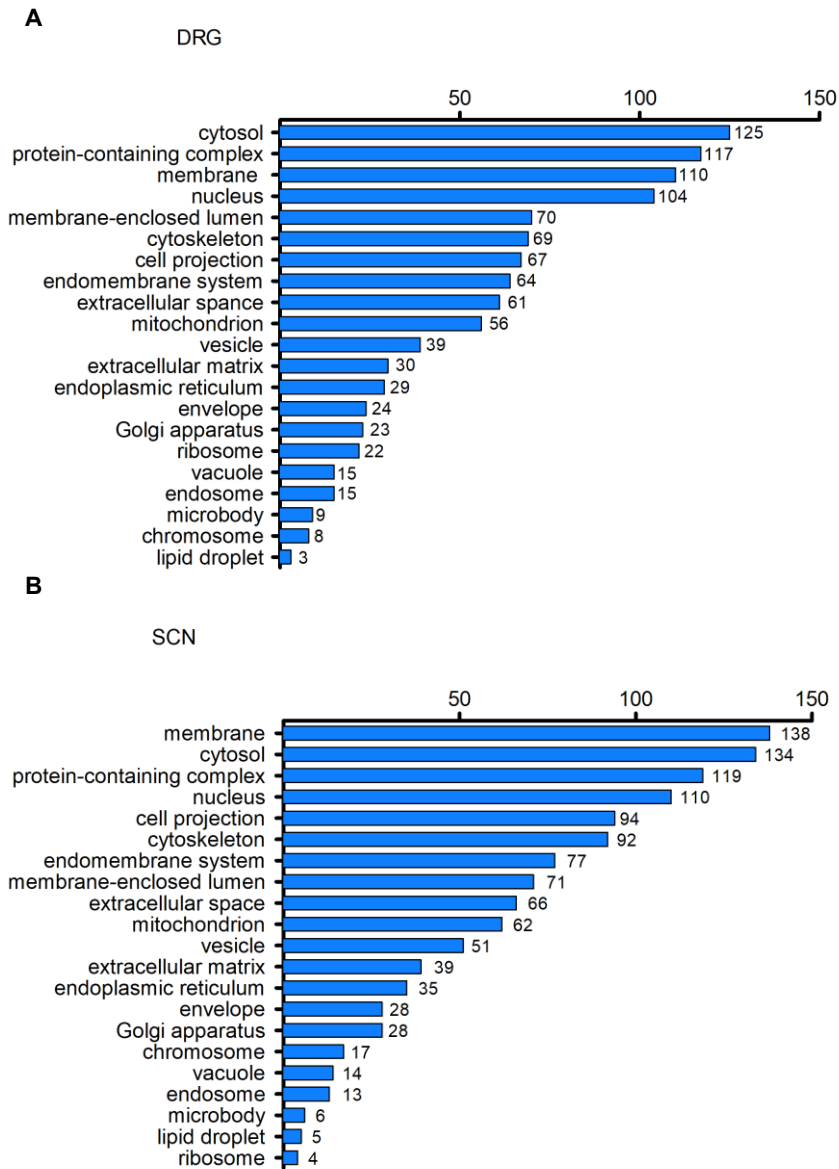


**Figure 31.** Cellular component categories plot of DRG (**A**) and SCN (**B**) data obtained using WebGestalt software and GO database. Values indicate the number of proteins included in each category.

We were also interested in identifying those proteins with larger fold changes that were also highly statistically significant. Hence, data were plotted in a volcano chart (**Fig. 32**).

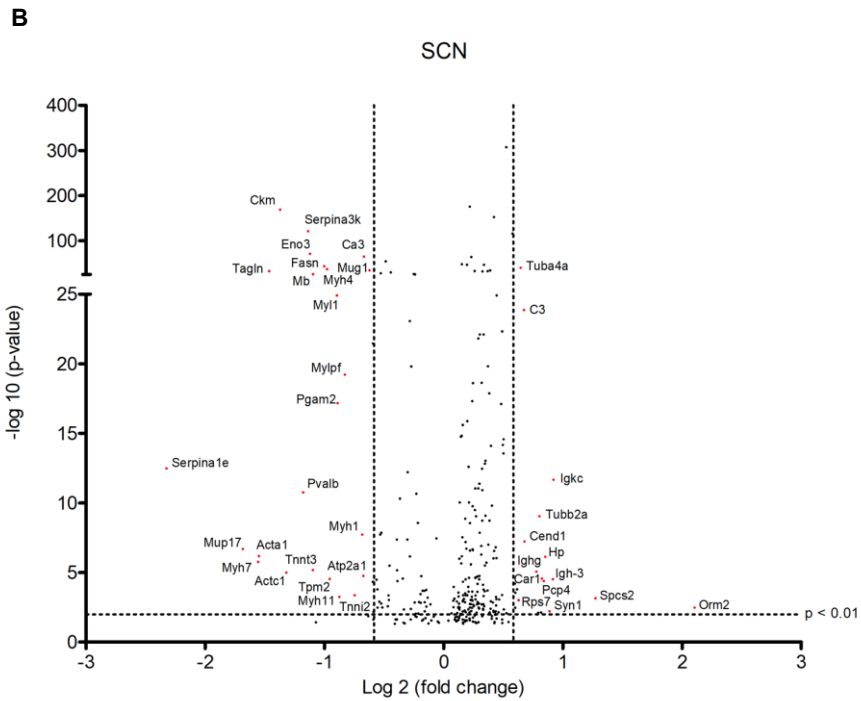
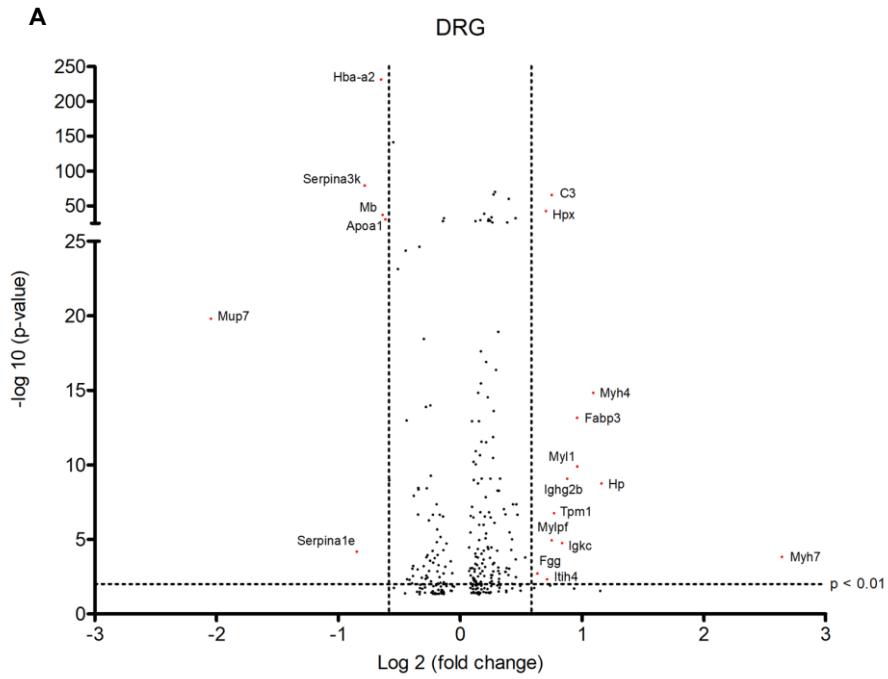


**Figure 32.** Volcano plot showing statistical significance ( $-\log_{10}$  p-value) versus magnitude of change ( $\log_2$  fold change) of the whole dataset from DRG (A) and SCN (B).

In a volcano plot, the most upregulated genes are towards the right, the most downregulated genes are towards the left, and the most statistically significant genes are towards the top. Differentially expressed proteins with a fold change  $\geq 1.5$  or  $\leq -1.5$  and a p-value  $< 0.01$  are highlighted in red and name is shown. One-way ANOVA test followed by Benjamini & Hochberg correction.

Then, we used DAVID bioinformatics resources 6.8 to identify the most significant biological functions in the data sets. DAVID software consists of an integrated biological knowledgebase and analytic tools aimed at systematically extracting biological meaning from large gene/protein lists. DAVID Knowledge Base is constructed using public databases such as Ensembl, Entrez, Uniprot, Gene Ontology, KEGG Pathways, BioCarta, etc. Therefore, the functional annotation derived from DAVID resources is the result of an integrative analysis.

Among all the analysis options available in DAVID, we chose functional annotation clustering since it measures the relationships among the annotation terms given by different databases to turn similar annotation into functional groups. This reduces the burden of different terms associated with the similar biological process, thus allowing more comprehensible biological interpretation of the data set. Functional clusters are ordered according to an enrichment score for the group based on the geometric mean of annotation terms' p-values. A higher score for a group indicates that these annotation terms in the group are playing more important roles in the study. Enrichment score of 1.3 is equivalent to a p-value of 0.05. Therefore, we paid attention to these functional clusters with an enrichment score over 1.3 [169].

The most relevant functional clusters obtained by DAVID analysis and the number of proteins found up or downregulated for each

biological term are plotted in **Figures 33** and **34**. Moreover, it is presented in **Tables 5** and **6**, a detailed description of the results obtained by DAVID analysis including the accession numbers of the proteins involved in each group.

Comparing the functional results from both independent studies we detected a high number of common altered features: cell-cell adherents junction, glycolysis and gluconeogenesis, tricarboxylic acid cycle, structural constituent of cytoskeleton, extracellular space, oxidoreductase activity, glutathione metabolic process, muscle protein, nucleotide phosphate-binding, lipid metabolism, fatty acid binding, neurofilament, calcium ion binding, oxygen transport, protease inhibitor and annexin.

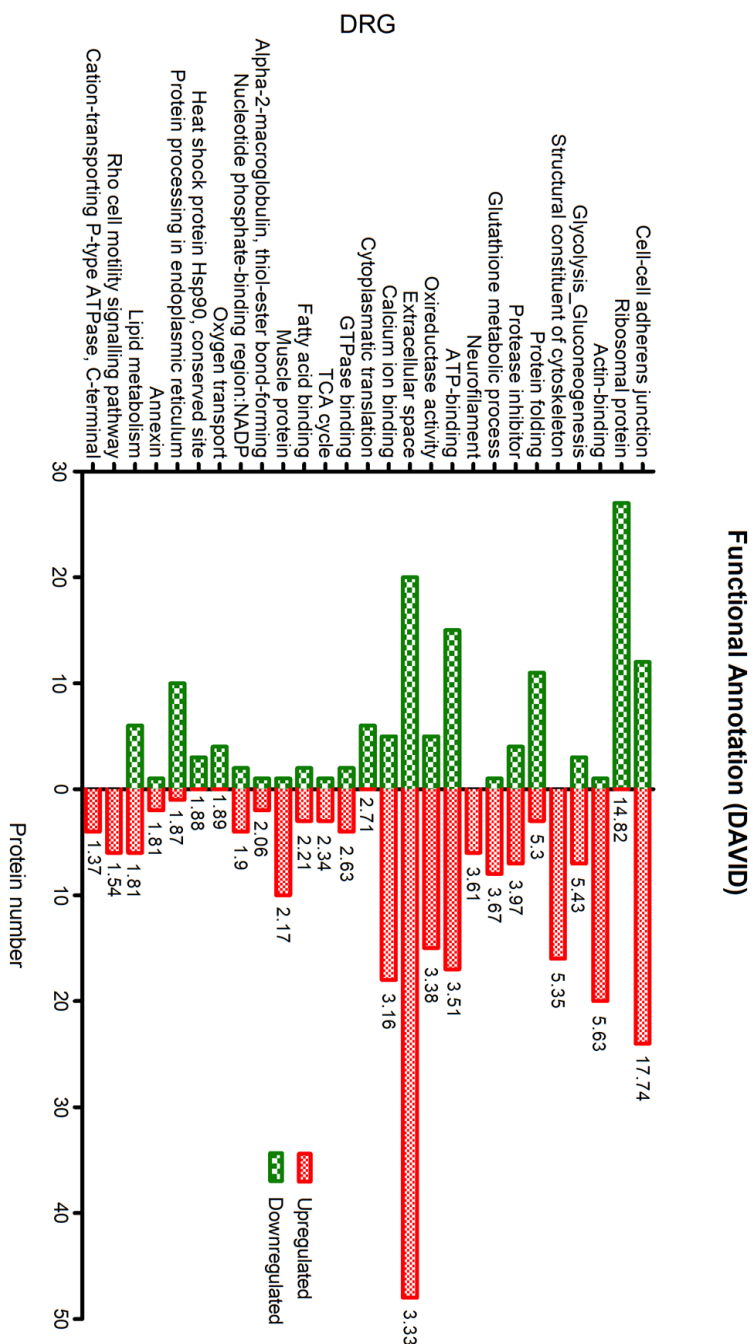


**Figure 33.** Plot of most relevant functional clusters obtained by DAVID 6.8 analysis for DRG data. Upregulated (red) and downregulated (green) proteins are shown for each biological term. Functional clusters are ordered according to an enrichment score for the group, based on the geometric mean of annotation terms' p-values.



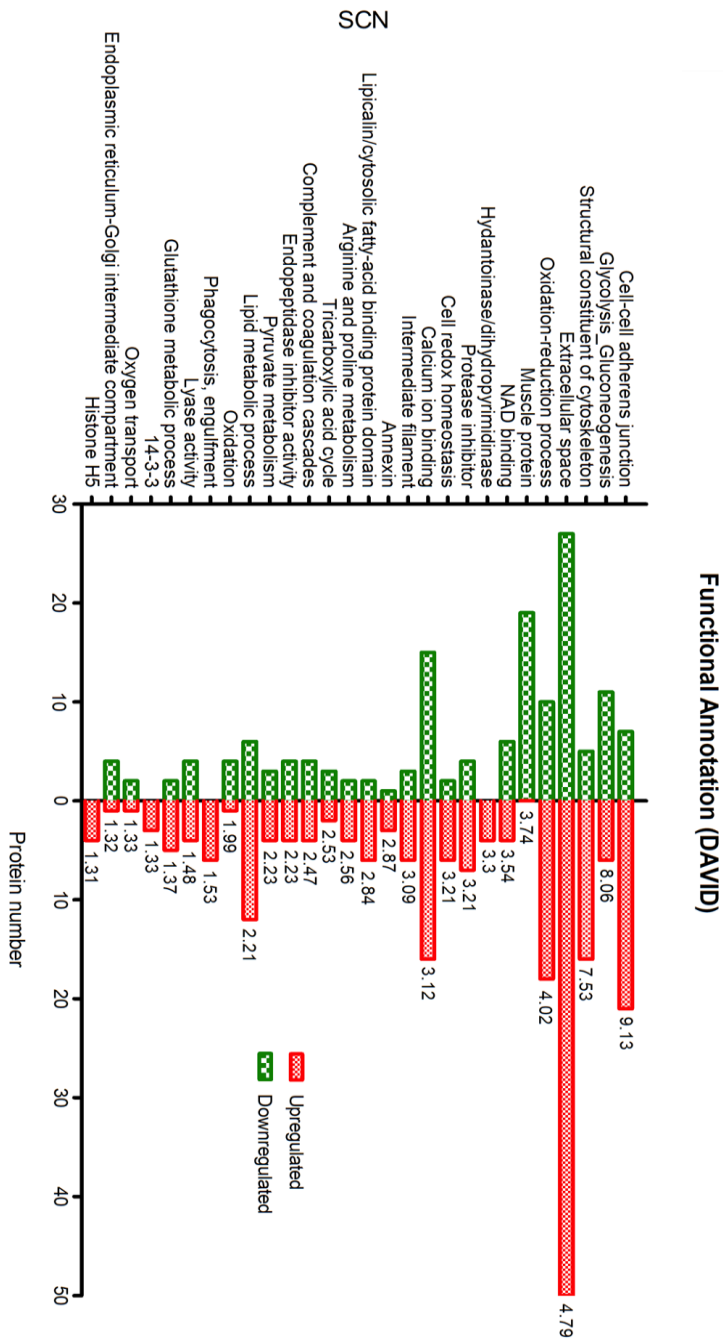


**Figure 34.** Plot of most relevant functional clusters obtained by DAVID 6.8 analysis for SCN data. Upregulated (red) and downregulated (green) proteins are shown for each biological term. Functional clusters are ordered according to an enrichment score for the group, based on the geometric mean of annotation terms' p-values.

**Table 5.** Summary of functional annotation results obtained by DAVID 6.8 analysis of DRG dataset.

Annotation cluster	Most representative annotation	Enrichment Group Score	Number of proteins involved	P-value of the most representative annotation	Benjamin of the most representative annotation	Proteins involved	Up/Down
1	Cell-cell adhesion junction	17.74	38	6.90E-22	3.90E-20	P07356, Q3U4Z3, Q92208, P93017, B8LI94, P35700, P12970, Q8B940, P83101, O88844, F6ZTG3, Q8VDD3, Q62261, E9Q3V6, D3Z0V2, E9D016, Q9D8N0, Q9JCC49, A1LUD3, B7ZWC0, P20029, P26039, P11489, P17182, B7S7B7, P16546, Q9WV44, Q64727, P05064, P60335, Q3UNN1, P62962, Q65398, P68040, P19096, F6XC15	24/12/1
2	Ribosomal protein	14.82	27	1.50E-19	9.50E-18	Q6ZVZ6, D3YVW6, Q545F8, Q9D1R9, D3YVU7, P62754, P12970, Q6PHZ1, P63325, E9Q3T0, P14131, P14148, A0A0A6YXL3, Q9DC49, Q9D8E6, P62908, P47963, Q497D7, Q3U561, P62911, Q921R2, Q9LJL8, P99027, O55142, D3YVW5, A0A1L1SQ48, O09167	27/1
3	Actin-binding	5.63	21	2.10E-07	1.10E-05	Q3TJX0, B2RY26, P26039, P14873, P16546, Q3TE06, P18760, P56871, Q647Z7, P62962, Q65398, P47754, Q8VDD5, A2A6J2, P68510, Q62261, P568774, Q55X39, F6XC15, P26041, Q9R0P5	20/1/1
4	Glycolysis_Gluconeogenesis	5.43	10	1.90E-05	8.70E-04	O70250, P17182, P21550, P06745, A0A0G2LEU1, P17183, Q9DBJ1, P16125, P05064, Q5RLV4	7/1/3
5	Structural constituent of cytoskeleton	5.35	16	5.60E-13	6.90E-11	P08551, P26039, Q9D0F9, Q7TMM9, P68372, P568771, P68369, Q65398, Q9ERD7, P20152, P19246, P99024, Q3TWW0, Q62261, P68368, P68774, Q05CEZ	16/1
6	Protein folding	5.3	14	4.40E-08	2.20E-05	G5E839, P63038, P11489, P63017, P35564, P08113, P17742, Q64433, Q3UWP8, P27773, P07901, P99024, P23927, Q3TGW8	3/1/11
7	Protease inhibitor	3.97	11	1.80E-06	2.80E-05	P10296, A0A0R4J0J1, Q00898, P29865, Q00897, A0A0R4J0K5, Q3ULJ3, Q61839, A0A0R4J1N1, Q3KQD4, Q62426	7/1/4
8	Glutathione metabolic process	3.67	9	4.70E-07	1.70E-04	Q9CPU0, P24472, Q88844, K9J474, P10649, E9P463, D3YX76, P08828, Q9D8N0	8/1/1
9	Neurofilament	3.61	6	5.40E-08	9.60E-07	P08551, P63054, P19246, G5E846, P46660, A0A0R4J036	6/1
10	ATP-binding	3.51	32	3.70E-04	3.40E-03	Q9Z1W8, O55222, Q3U4Z3, P63038, P07310, B2RY26, Q8B947, Q8R429, Q01853, P63017, P56389, P08113, Q3UJQ3, Q8R2X0, P07901, Q8VDD5, Q02053, Q9JHJ4, Q5SX39, Q3TE03, Q6PIC6, G5E839, P20029, D3YVYV, P11489, Q8CGC7, Q04447, A0A1VZP7Z3, P10630, P10296, Q8VDDZ, P68134	17/1/15

Annotation cluster	Most representative annotation	Enrichment Group Score	Number of proteins involved	P-value of the most representative annotation	Benjaminli of the most representative annotation	Proteins involved	Up/Down
11	Antioxidant activity	3.49	7	1.20E-06	5.20E-05	P31725, P27005, P06728, P35700, P08228, D3Z0V2, O61646	7↑
12	Oxidoreductase activity	3.38	20	2.00E-03	2.30E-02	P54071, Q9CSR6, Q8C7K6, Q8BMS1, P35700, P08228, Q3TQP6, P16125, P14152, Q9EQD6, O88844, P50396, Q80T88, Q9DCT2, A0A0G2JEU1, E0CXN5, P19096, D3Z0V2, Q3TCL2, G3X9T8	15↑/5↓
13	Extracellular space	3.33	68	1.10E-18	4.80E-17	P07356, P28665, P07310, P50114, P46660, P63017, A0A075BSP3, P00920, P18760, Q6Z4Z6, P29699, Q61646, P48036, K9JAZ4, P16045, Q8VCM7, F8WIK1, F010Z7, P11404, P50543, Q91X72, B7STB7, Q61838, P17182, P06745, P08228, P17183, A0A0U1RNG0, Q3UWPF, A0A0R4J0I1, A5JUZ1, Q8CAZ9, P31725, P27773, P07724, Q9Z111, Q3KQ4, P26041, Q00623, P68134, Q3TCL2, Q00898, Q00897, P63038, Q60784, P27005, Q31T92, Q6Z000, P35700, P17742, P14152, A0A087W516, P63101, Q3UJL3, Q0Z788, D3Z0V2, P63028, Q3TJX0, Q31DZ5, P06728, Q61613, P05064, P70296, A0A0R4J0X5, A0L1V3, P21550, P16330, G3X9T8	48↑/20↓
14	Calcium ion binding	3.16	23	8.90E-04	1.40E-02	P63028, Q3TJX0, P07356, Q60784, P14089, P27005, P50114, Q8R429, B7STB7, P97457, P35664, P05977, P16546, A0A1W2P6G5, Q3UWPF, P48036, P31725, Q8R2X0, Q9Z2W7, P10493, Q99M71, A0A0R4J1N1, P50543	18↑/5↓
15	calcium-dependent protein binding	2.78	6	3.80E-03	3.60E-02	P07356, P14089, P50114, A2A6L2, B7STB7, P50543	5↑/1↓
16	cytoplasmatic translation	2.71	6	1.20E-04	1.20E-02	P99027, O55142, D3YVM5, EQQ3T0, P14148, A0A06VYX13	6↓
17	GTPase binding	2.63	6	6.50E-05	1.80E-03	Q3TJX0, P07901, Q6Z261, P17182, Q8CGC7, F6XC15	4↑/2↓
18	TCA cycle	2.34	4	3.70E-02	2.70E-01	P54071, Q88844, Q3TE3, P14152	3↑/1↓
19	Fatty acid binding	2.21	5	5.70E-04	1.00E-02	P04117, P07724, P51880, P11404, Q05816	3↑/2↓
20	Spectrin repeat	2.19	4	4.00E-03	7.60E-02	Q6S388, Q05AA6, Q6Z261, P16546	4↑
21	Muscle protein	2.17	11	4.60E-10	1.30E-08	B2RY26, A2A6L2, P04247, A0A1L1STN8, P97457, P05977, Q5SX39, P58774, P58771, A0A1W2P6G5, P68134	10↑/1↓
22	Alpha-2-macroglobulin, thio-ester bond-forming	2.06	3	7.00E-03	1.20E-01	P28665, Q61838, P01027	2↑/1↓
23	Nucleotide phosphate-binding region:NADP	1.9	6	2.20E-03	1.00E-01	P54071, Q88844, Q9CSR6, Q3TQP6, Q3TCL2, Q9EQD6	4↑/2↓
24	Oxygen transport	1.89	4	8.20E-04	6.80E-03	A8DUK4, Q54AH9, P04247, Q91VB8	4↓

Annotation cluster	Most representative annotation	Enrichment Group Score	Number of proteins involved	P-value of the most representative annotation	Benjamini of the most representative annotation	Proteins involved	Up/Down
25	Heat shock protein Hsp90, conserved site	1.88	3	4.90E-04	2.10E-02	P07901, P11489, P08113	3↑
26	Protein processing in endoplasmic reticulum	1.87	11	5.60E-03	7.70E-02	Q3UWP8, P27773, P20029, P07901, Q01853, P11499, P63017, P35564, P23927, P08113, Q3TL58	11↑/10↓
27	Annexin	1.81	3	8.50E-03	5.10E-02	P48036, P07356, B7STB7, Q9CSR6, Q3UKH3, Q8BWS1, A0A0G2JDU5, P01027, Q8BQS5, P19096, Q3TED3, D3Z0Y2, Q00623, Q9EQ08, Q991Y0	2↑/1↓
28	Lipid metabolism	1.81	12	1.10E-02	6.30E-02	P24472, P10649, Q3UKH3, Q3TFC8, Q8BWS1, Q8R0M2, Q8CGC7, Q8DBJ1, G3XA25, Q98UY0, K9JA74, E9PV63, P40142, D3YX76, O70250, A0A0G2JEU1, P19096, D3Z0Y2, Q8R3P0, Q3TED3	6↑/6↓
29	Metabolic process	1.64	20	4.90E-05	7.90E-03	P62962, P28039, Q3TN61, P97457, P18760, Q64727	15↑/5↓
30	Rho cell motility signalling pathway	1.54	6	7.90E-04	6.30E-02	P16015, P00920, P13634	6↑
31	Carbonic anhydrase, alpha-class, conserved site	1.54	3	8.50E-03	1.40E-01		2↑/1↓
32	Extracellular matrix	1.48	11	5.10E-04	4.60E-03	Q8CAZ9, P07356, Q3TDZ5, P16045, Q60784, P10493, Q60675, Q62000, F8VQJ3, Q02798, Q04897	10↑/1↓
33	Cation-transporting P-type ATPase, C-terminal	1.37	4	8.60E-04	3.10E-02	D3YYNF, Q8R429, Q6PIC6, Q8VDN2	4↑

**Table 6.** Summary of functional annotation results obtained by DAVID 6.8 analysis of SCN dataset.

Annotation cluster	Most representative annotation	Enrichment Group Score	Number of proteins involved	P-value of the most representative annotation	Benjamini of the most representative annotation	Proteins involved	Up/Down
1	Cell-cell adherens junction	9.13	28	1.1E-12	3.9E-11	P81979, Q9CFV4, P63017, P35700, O08709, O55131, P63101, O88844, Q9QXS1, Q62261, Q62165, P62827, Q9D8N0, Q9LVV1, P20029, P11449, P17182, P06151, P16546, Q61739, Q99N28, P05064, P62962, P68433, Q61553, Q8R315, Q8BTM8, P19098	21/7↓
2	Glycolysis/Gluconeogenesis	8.06	17	6.2E-12	6.4E-10	Q9LJL2, Q9JLH6, P17182, P17751, P06151, P06745, P47697, P17183, Q9DBJ1, P16125, P05064, P06411, Q9D0F9, P21550, Q70250, P47738, P16658, P08551, A2A5S8, Q9WV92, Q9D0F9, QTTMM9, P68372, Q70318, P68771, P68389, Q927F4, Q8ERD7, Q9QXS1, P20152, P19246, P99024, Q62261, P68368, Q3UX10, P58774, Q70V5, Q5XKE0	6/11↓
3	Structural constituent of cytoskeleton	7.53	21	2.4E-18	1.3E-15	Q60590, P28665, P62188, P07310, P32261, P63017, P00920, P18760, Q62426, Q08677, P29699, Q61646, P48036, Q35206, P34884, P16045, Q62165, P01027, P14602, P11404, P18242, Q91X72, Q9JLH6, P17182, P17751, Q61838, P06745, P07361, P08228, P17183, P31725, P27773, P96029, Q61207, Q8QX19, P10126, P07724, Q92111, P02469, P46376, P26041, P68134, Q00623, Q62188, Q00898, Q00897, Q61147, Q8VCT4, P08813, Q62000, P13020, P35700, P17742, P14152, Q08709, P07758, P63101, P23506, P07759, Q02788, P51910, Q55042, P68033, P63028, P20918, P51642, P19324, P01667, P01668, P05064, Q60854, P60710, P51885, P21550, Q61554, P16930, P28654	50/12↑
4	Extracellular space	4.79	77	2.20E-20	1.30E-18	P54071, Q61147, P13707, P35700, Q9CZ13, Q62425, P41452, Q08709, Q61171, Q88844, P24849, Q00812, Q55042, Q9LJL2, Q9D0C2, Q9JLH6, P10639, P06151, P08228, P06801, P16125, P50396, Q61598, P99028, P45376, P19096, P47738, Q9QLUH0	18/10↓
5	Oxidation-reduction process	4.02	28	3.1E-5	4.6E-3	P13412, P37604, P32848, P21107, P04247, P97457, P05977, P58771, P20901, Q5SX40, Q91283, Q9QZ47, P68033, P58774, Q08638, Q5SX39, Q80605, Q5XKE0, P68134	19↓
6	Muscle protein	3.74	19	4.9E-21	2.7E-19		

Annotation cluster	Most representative annotation	Enrichment Group Score	Number of proteins involved	P-value of the most representative annotation	Benjamini of the most representative annotation	Proteins involved	UpDown
7	Spectrin repeat	3.6	6	3.0E-5	3.7E-3	Q9JI91, Q055AA6, Q9QXS1, Q62261, P16546, O88990	4/121
8	NAD binding	3.54	10	3.9E-7	2.2E-5	Q9JLJ2, Q9DON2, P54071, O88844, P13707, Q8VDC8, P06801, P14125, P14152, P16858	4/161
9	Hydantoinase/dihydropyrimidinase	3.3	4	6.3E-5	4.3E-3	Q62188, P97427, O08553, Q9ECF6	4↑
10	Protease inhibitor	3.21	11	6.7E-6	9.0E-5	Q00898, Q60854, P28665, Q00897, P07758, P32261, P07759, A6X935, Q61838, Q62426, O08677	7/141
11	cell redox homeostasis	3.21	8	1.1E-4	1.0E-2	O08709, Q61171, P27773, P99029, P10639, P35700, P09103, Q9QLHD	6/121
12	Calcium ion binding	3.12	31	4.7E-6	1.8E-4	Q9JI91, Q8BH64, Q8R429, Q35639, P32848, A6X935, P06977, P13020, P0DE26, P14824, P48036, P20801, Q08529, Q99MQ4, Q62165, O55042, Q80603, F63028, P56480, Q07076, A2ASS6, P14069, P06207, P97457, P16546, O88990, P31725, Q06138, F09405, P10493, Q61554	16/115↓
13	Intermediate filament	3.09	9	5.4E-4	4.4E-3	Q6P5H2, P08553, P08551, P20152, P15331, P19246, F63017, Q01768, Q70V5	6/131
14	Extracellular matrix	3.04	39	8.6E-24	6.8E-22	F61979, F62198, F63017, F68372, Q62000, Q61292, P30700, P18760, F62301, P29699, P16045, Q35206, Q9QXS1, P20152, Q99MQ4, Q8BH63, Q02788, P14602, F62827, P09103, Q80605, P18242, P20029, P56480, F63001, P62082, P08228, P31725, Q80X19, P10493, F51885, P99024, P02468, P02469, Q8BTM8, Q61554, Q04857, P28654, P16858	22/171↓
15	Regulation of muscle contraction	2.90	6	3.4E-5	4.7E-3	P13412, P20801, Q8R429, P20444, Q9QZ47, P14824	2/141
16	Annexin	2.87	4	5.1E-4	4.3E-3	P48036, Q07076, Q35639, P14824	3/111
17	Lipocalin/cytosolic fatty-acid binding protein domain	2.84	8	5.1E-5	4.2E-3	P04117, P24526, Q06059, P51910, P07361, P11404, Q05816, B5X0G2	6/121
18	Arginine and proline metabolism	2.56	6	8.4E-3	7.3E-2	Q9JLJ2, P30275, P06202, P07310, Q04447, P47738	4/121
19	Tricarboxylic acid cycle	2.53	5	3.5E-4	3.1E-3	Q89K10, P54071, O88844, Q9DDG2, P14152	2/131
20	Complement and coagulation cascades	2.47	8	3.4E-3	3.8E-2	Q00898, Q00897, F07758, P20918, P32261, Q8BH61, P01027, O08677	4/141

Annotation cluster	Most representative annotation	Enrichment Group Score	Number of proteins involved	P-value of the most representative annotation	Benjamini of the most representative annotation	Proteins involved	Up/Down
21	Endopeptidase inhibitor activity	2.23	8	8.0E-7	4.0E-5	Q00898, P28665, O00897, P07758, Q61838, P01027, Q62426, P28699	4/14
22	Pyruvate metabolism	2.23	7	4.5E-4	1.2E-2	Q9LJL2, Q9CPJ0, P06151, P47738, P06801, P16125, P14152	4/12
23	Lipid metabolic process	2.21	18	2.1E-3	7.8E-2	Q9DCN2, P56480, P51150, P63005, Q8VCT4, P42125, Q05816, O08709, O35678, Q61207, Q61206, P51910, P01027, Q9R0Q7, P19096, Q8BWT1, C8CGN5, Q00623	12/16
24	Oxidation	1.99	5	7.2E-5	7.2E-4	P60710, P09813, P68033, P68134, Q00623	1/14
25	Phagocytosis, engulfment	1.53	6	9.2E-4	4.6E-2	P01837, P01863, P01867, P63001, P01868, P13020	6/1
26	Lyase activity	1.48	8	1.1E-2	9.4E-2	Q9CPJ0, Q99K10, P16015, P21550, P00920, P13634, P17183, P19096	4/14
27	Oxidoreductase activity, acting on the aldehyde or oxo group of donors, NAD or NADP as acceptor	1.47	4	1.8E-2	1.4E-1	Q9LJL2, P24549, P47738, P16858	2/12
28	Glutathione metabolic process	1.37	7	1.6E-4	1.5E-2	Q9CPJ0, P24472, O88844, Q00612, P08228, P15626, Q9DBN0	5/12
29	14-3-3 protein	1.33	3	5.8E-3	1.3E-1	P61982, P63101, P68510	3/1
30	Oxygen transport	1.33	3	2.0E-2	9.4E-2	P02088, P01942, P04247	1/12
31	Endoplasmic reticulum, Golgi intermediate compartment	1.32	5	2.2E-2	1.0E-1	Q9JKM7, P20029, P19324, Q8R429, P09103	1/14
32	Histone H5	1.31	4	3.6E-4	1.5E-2	P10922, P43274, P43277, P15864	4/1

We ran dataset analysis with different bioinformatic tools aiming to obtain consistent functional results regardless the software used. In that sense, String v11.0, a database of known and predicted protein-protein interactions, was used to generate a pathway network of interconnected proteins. In DRG, the network consisted in 221 nodes and 539 edges with an enrichment p-value  $< 1.0 \times 10^{-16}$ , indicating that these proteins are at least partially biologically interconnected. On the other hand, the protein association network from SCN involved 308 nodes connected through 654 edges, also with significantly more interactions than expected (**Table 7; Fig. 35, 36**).

Finally, we analysed datasets using GeneRanker software from Genomatix to perform a similar analysis as DAVID, but in an automated way using conventional databases and existing bibliography as data source. We selected biological functions derived from GO-terms as the most relevant information (**Table 8**).

Overall, different bioinformatic tools obtained similar biological conclusions from our proteomic datasets, concluding that *db/db* DRG and SCN develop metabolic dysregulation related to glucose and lipid metabolism, tissue scaffold abnormalities based on alterations in structural proteins, a mild dysregulation of folding chaperones, an upregulation of acute-phase response and inflammation, and an alteration of oxidative stress-related proteins. Considering these results, we proceeded with the analysis of the most relevant proteins included in the functional clusters by manual literature search and database examination.



**Table 7.** Summary of most relevant functional terms from KEGG database using String v11.0. Annotation terms were selected based on the false discovery rate and their biological relevance using DRG (**A**) and SCN (**B**) proteomic data.

**A**

DRG Description	KEGG Pathways	
	Count in gene set	False discovery rate
Ribosome	20/128	6,36E-15
Carbon metabolism	14/118	5,74E-09
Biosynthesis of aminoacids	9/75	1,01E-05
Glycolysis/Gluconeogenesis	8/65	3,17E-05
Gap junction	8/85	1,20E-04
Protein processing in endoplasmic reticulum	10/161	1,80E-04
Metabolic pathways	31/1296	1,80E-04
Antigen processing and presentation	7/78	3,60E-04
PPAR signaling pathway	7/85	5,60E-04
Focal adhesion	10/195	5,70E-04
Glutathione metabolism	6/61	7,10E-04
Pyruvate metabolism	5/38	8,10E-04
Fatty acid metabolism	5/51	2,60E-03
cGMP-PKG signaling pathway	8/164	3,30E-03
HIF-1 signaling pathway	6/102	6,60E-03
Ferroptosis	4/40	8,10E-03
Nitrogen metabolism	3/17	8,10E-03
Cardiac muscle contraction	5/75	9,20E-03
Regulation of actin cytoskeleton	8/208	9,70E-03
Cholesterol metabolism	4/48	1,07E-02
Tight junction	7/165	1,07E-02
ECM-receptor interaction	5/81	1,07E-02
Fatty acid elongation	3/26	1,52E-02
PI3K-Akt signaling pathway	10/349	1,65E-02
Metabolism of xenobiotics by cytochrome P450	4/65	2,27E-02
Pentose phosphate pathway	3/32	2,27E-02
Citrate cycle (TCA cycle)	3/32	2,27E-02

**B**

SCN Description	KEGG Pathways	
	Count in gene set	False discovery rate
Glycolysis/Gluconeogenesis	17/65	2,43E-13
Carbon metabolism	19/118	5,79E-12
Biosynthesis of aminoacids	14/75	1,50E-09
Metabolic pathways	49/1296	2,36E-08
Focal adhesion	16/195	1,89E-06
Gap junction	11/85	3,32E-06
Pyruvate metabolism	7/38	5,74E-05
HIF-1 signaling pathway	10/102	7,14E-05
ECM-receptor interaction	9/81	7,93E-05
Tight junction	12/165	0,00012
Cardiac muscle contraction	8/75	0,00029
Protein processing in endoplasmic reticulum	11/161	0,00039
Complement and coagulation cascades	8/88	0,00062
Regulation of actin cytoskeleton	12/208	0,00063
Arginine and proline metabolism	6/50	0,00110
Pentose phosphate pathway	5/32	0,00120
Citrate cycle (TCA cycle)	5/32	0,00120
Endocrine and other factor-regulated Ca <sup>2+</sup> reabsorption	6/54	0,00130
PI3K-Akt signaling pathway	15/349	0,00130
2-Oxocarboxylic acid metabolism	4/19	0,00170
PPAR signaling pathway	7/85	0,00190
Glucagon signaling pathway	7/99	0,00390
cGMP-PKG signaling pathway	9/164	0,00390
Axon guidance	9/174	0,00540

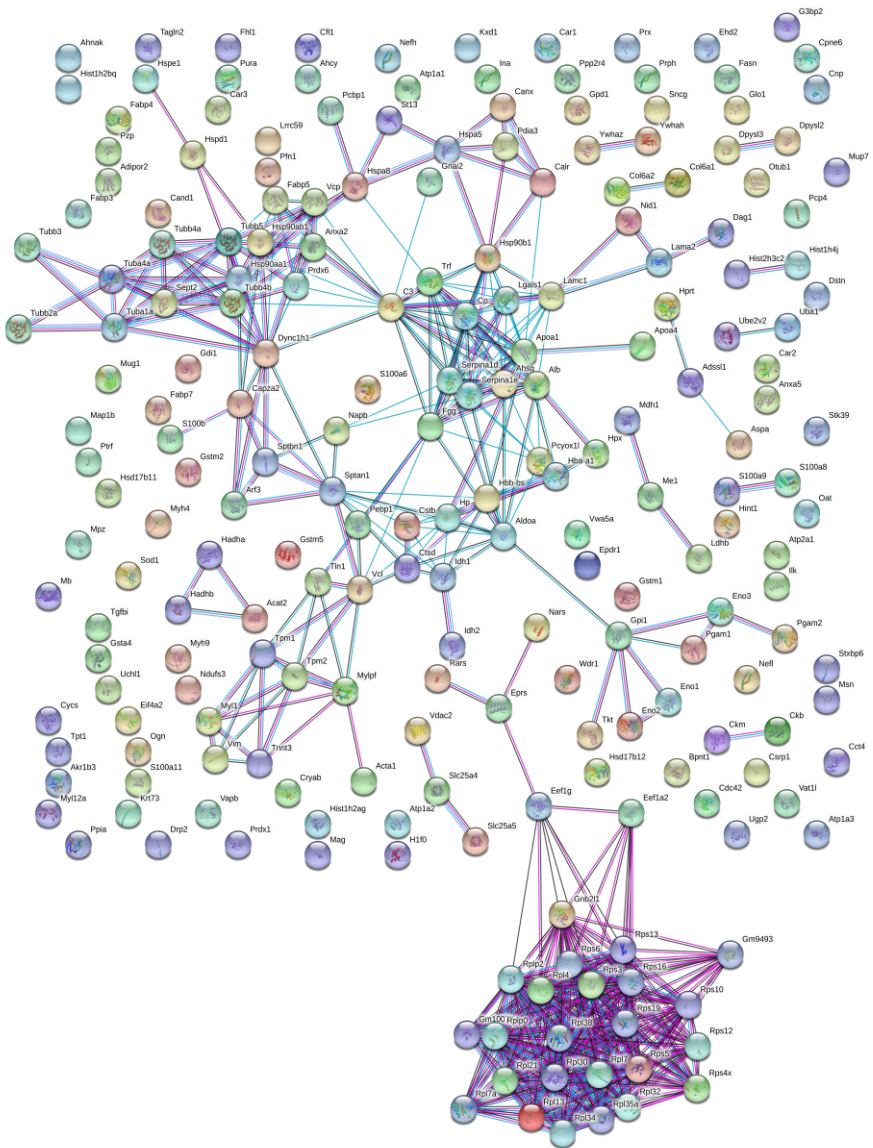


**Figure 35.** Network of interconnected proteins generated by String v11.0 software for DRG data. Network edges are based on the type of interaction evidence (experiments = violet, databases = blue, co-expression = black, protein homology = purple) considering that the minimum required interaction score was set as the highest confidence (0.900).

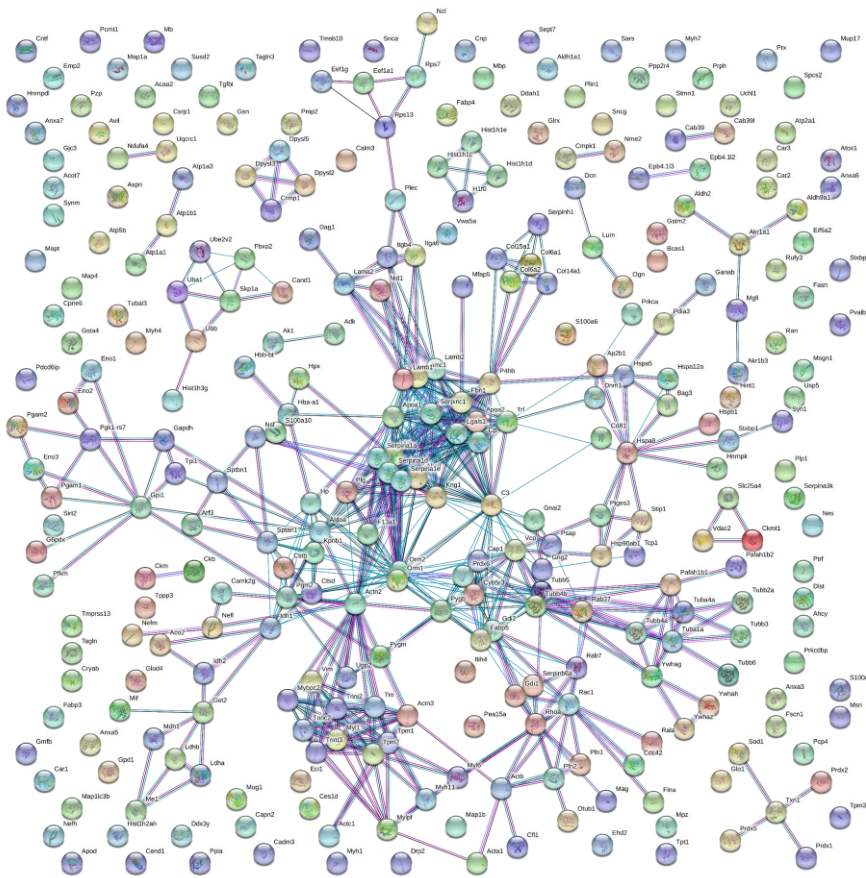


**Figure 36.** Network of interconnected proteins generated by String v11.0 software for SCN data. Network edges are based on the type of interaction evidence (experiments = violet, databases = blue, co-expression = black, protein homology = purple) considering that the minimum required interaction score was set as the highest confidence (0.900).

**Table 8.** Summary of most relevant functional terms from GO database using Genomatix platform. Annotation terms were selected based on the p-value and their biological relevance using DRG (A) and SCN (B) proteomic data.

<b>A DRG</b>	<b>GO-Terms (Genomatix)</b>	
<b>Description</b>	<b>Genes (observed)</b>	<b>P-value</b>
Cytoskeleton organization	49	1,08E-15
Carboxylic acid metabolic process	38	7,43E-13
Cellular metabolic process	166	5,30E-13
Translation	33	1,50E-12
Response to stress	80	8,59E-11
Actin cytoskeleton organization	28	2,89E-10
Muscle contraction	18	5,71E-09
Catabolic process	52	5,66E-09
Regulation of cell death	48	1,39E-09
Protein folding	13	3,94E-08
Intermediate filament cytoskeleton organization	8	3,00E-08
Response to reactive oxygen species	13	2,54E-07
ATP metabolic process	14	2,13E-07
Glutathione metabolic process	8	1,66E-07
NAD metabolic process	6	5,43E-06
NADP metabolic process	6	3,34E-06
Glycolytic process	8	1,19E-06
Tricarboxylic acid metabolic process	5	6,49E-05
Fatty acid metabolic process	14	6,28E-05
Lipid metabolic process	28	2,46E-04
Gluconeogenesis	4	8,46E-03
Cell-cell junction organization	7	6,49E-03
Oxygen transport	2	3,58E-03

<b>B SCN</b>	<b>GO-Terms (Genomatix)</b>	
<b>Description</b>	<b>Genes (observed)</b>	<b>P-value</b>
Cytoskeleton organization	68	1,34E-26
Muscle contraction	29	9,61E-18
Actin cytoskeleton organization	41	2,15E-18
Catabolic process	71	5,55E-16
ATP metabolic process	23	9,74E-15
Regulation of cell death	63	3,50E-15
Carboxylic acid metabolic process	45	1,01E-15
Response to stress	94	1,76E-13
Cellular metabolic process	177	1,17E-10
NAD metabolic process	9	1,54E-09
Response to reactive oxygen species	15	2,28E-08
Intermediate filament cytoskeleton organization	7	1,34E-06
Cell-cell junction organization	13	1,31E-06
Lipid metabolic process	36	2,03E-06
Regulation of NADP metabolic process	3	7,53E-05
Glutathione metabolic process	6	6,64E-05
Fatty acid metabolic process	15	6,45E-05
Tricarboxylic acid cycle	5	3,45E-05
Gluconeogenesis	7	3,36E-05
Canonical glycolysis	2	5,08E-04
Protein folding	9	2,38E-04
Acute-phase response	5	2,15E-04

DRG and SCN proteins highlighted in this section are shown in **Table 9** and **10** grouped by functional clusters with the corresponding fold change.

We found multiple proteins involved in glutathione metabolism and **antioxidant activity** in both tissues. In DRG, several isoforms belonging to Mu class of Glutathione S enzymes (GSTM) were upregulated whereas in SCN some of these isoforms were reduced. These opposite results were confirmed by western blot in both tissues (**Fig. 37, 38**). Conjugated with glutathione, GSTM participates in the detoxification of electrophilic compounds, including carcinogens, drugs, toxins and ROS. Concomitantly, we observed that mitochondrial isocitrate dehydrogenase 2, which promotes regeneration of reduced glutathione by supplying NADPH [170], was increased in DRG but not in SCN. On the other hand, in both tissues we detected an increase of superoxide dismutase 1 and many peroxiredoxins isoforms, a highly-conserved family of antioxidant proteins that scavenge cellular ROS. Moreover, other antioxidant proteins such as thioredoxin, glutaredoxin-1 and glyoxalase I were augmented. Interestingly, we previously found by western blot decreased levels of HO-1, an antioxidant protein under the control of NRF2 pathway, in DRG and SCN, further indicating oxidative stress in these tissues (**Fig. 37, 38**).

**Carbohydrate and lipid metabolism** were also altered in both tissues. Several enzymes implicated in glycolytic pathway (phosphoglucose isomerase, phosphofructokinase,  $\beta$ -enolase, phosphoglycerate mutase 2, phosphoglycerate kinase 1, GAPDH and fructose biphosphate aldose 1) were downregulated. In addition, in SCN we observed a decline in the content of aconitase, a TCA cycle enzyme. In SCN we also detected decreased levels of OGDC-

E2, which catalyses the conversion of 2-oxoglutarate to succinyl-CoA and CO<sub>2</sub> in the TCA cycle. Regarding lipid metabolism, we found an upregulation in lipid catabolism-related proteins (trifunctional enzyme, acetyl-CoA acetyltransferase, perilipin-1, monoglyceride lipase, Ras-related protein Rab-7a and Enoyl-CoA delta isomerase I) whereas a reduction in proteins implicated in lipid biosynthesis (17-β-HSD 12, fatty acid synthase, NADH-cytochrome b5 reductase 3 and NADP-dependent malic enzyme).

Translation was downregulated in DRG as demonstrated by a decrease in proteins that constitute the **ribosomal subunits** 60S and 40S and the translation-related factors eIF-4A-II, EF-1-gamma and EF-1-alpha-2, but not in SCN. Another discrepancy between SCN and DRG was the upregulation of **muscle-related proteins** in DRG, such as myosin heavy chain-4, myosin light chain-1, tropomyosin-1, tropomyosin-2, myosin regulatory light chain 2 and actin, but their downregulation in SCN. However, **cytoskeleton proteins** were augmented in both tissues (neurofilament polypeptide, tubulin, spectrin and moesin).

Our data shows differentially expressed positive (haptoglobin, orosomucoid 1, fibrinogen gamma chain, complement C3, hemopexin and inter-a-inhibitor heavy chain 4) and negative (serum albumin and alpha-2-HS-glycoprotein) **acute-phase proteins**. C3 overexpression was confirmed by western blot in both tissues (**Fig. 37, 38**). Many of these proteins can modulate one or more stages of the **inflammatory response** [171]. Associated with the acute-phase response activation, inflammatory markers like S100-A8/9 in DRG and S100-A9 in SCN were enriched. Moreover, levels of immunoglobulin light chain kappa and heavy chain gamma were higher in both tissues.

**Table 9.** List of highlighted proteins from DRG with the corresponding fold change ratio and grouped by functional clusters.

<b>DRG</b>	
<p><b>Oxidative stress</b></p> <p>GSTM1 (1.32)</p> <p>GSTM2 (1.10)</p> <p>GTSM5 (1.37)</p> <p>IDH2 (1.35)</p> <p>SOD1 (1.13)</p> <p>Glyoxalase I (1.12)</p> <p>Peroxiredoxin-1 (1.08)</p> <p>Peroxiredoxin-6 (1.11)</p>	<p><b>40S ribosomal proteins</b></p> <p>S2 (0.9)</p> <p>S3 (0.87)</p> <p>S4 (0.82)</p> <p>S5 (0.7)</p> <p>S7 (0.79)</p> <p>S13 (0.79)</p> <p>S14 (0.79)</p> <p>S16 (0.86)</p> <p>S19 (0.88)</p>
<p><b>Glycolytic pathway</b></p> <p>Beta enolase (0.79)</p> <p>Phosphoglycerate mutase 2 (0.76)</p>	<p><b>Translation factors</b></p> <p>eIF-4A-II (0.85)</p> <p>EF-1-gamma (0.84)</p> <p>EF-1-alpha-2 (0.93)</p>
<p><b>Lipid catabolism</b></p> <p>Trifunctional enzyme (1.19)</p> <p>Acetyl-CoA acetyltransferase (1.10)</p>	<p><b>Acute-phase response (positive)</b></p> <p>Haptoglobin (2.23)</p> <p>Orosomucoid 1 (1.52)</p> <p>Fibrinogen gamma chain (1.55)</p> <p>Complement C3 (1.68)</p> <p>Hemopexin (1.63)</p> <p>Inter-alpha-inhibitor heavy chain 4 (1.64)</p>
<p><b>Lipid biosynthesis</b></p> <p>17-beta-HSD 12 (0.76)</p> <p>Fatty acid synthase (0.74)</p> <p>NADP-dependent malic enzyme (0.87)</p>	<p><b>Acute-phase response (negative)</b></p> <p>Serum albumin (0.91)</p> <p>Alpha-2-HS-glycoprotein (0.91)</p>
<p><b>Muscle-type and cytoskeleton proteins</b></p> <p>Myosin heavy chain-4 (2.13)</p> <p>Myosin light chain-1 (1.95)</p> <p>Tropomyosin-1 (1.71)</p> <p>Tropomyosin-2 (1.91)</p> <p>Myosin regulatory light chain 2 (1.68)</p> <p>Actin (1.39)</p> <p>Neurofilament light polypeptide (1.22)</p> <p>Neurofilament heavy polypeptide (1.20)</p> <p>Tubulin beta-5 chain (1.25)</p> <p>Tubulin beta-2A chain (1.24)</p> <p>Tubulin alpha-4A chain (1.21)</p> <p>Tubulin beta-4B chain (1.18)</p> <p>Tubulin beta-4A chain (1.18)</p> <p>Tubulin beta-3 chain (1.16)</p> <p>Tubulin alpha-1A chain (1.12)</p> <p>Spectrin beta chain (1.08)</p> <p>Spectrin alpha chain (1.07)</p> <p>Moesin (1.09)</p>	<p><b>Inflammatory markers</b></p> <p>S100-A8 (1.32)</p> <p>S100-A9 (1.34)</p> <p>Ig light chain kappa (C region) (1.79)</p> <p>Ig heavy chain gamma 2B (C region) 1.84)</p>
<p><b>60S ribosomal proteins</b></p> <p>P2 (0.89)</p> <p>L4 (0.83)</p> <p>L7 (0.88)</p> <p>L7a (0.87)</p> <p>L10a (0.79)</p> <p>L13 (0.88)</p> <p>L17 (0.82)</p> <p>L21 (0.75)</p> <p>L30 (0.86)</p> <p>L31 (0.79)</p> <p>L32 (0.82)</p> <p>L34 (0.78)</p> <p>L35a (0.82)</p> <p>L38 (0.87)</p>	<p><b>Protein folding</b></p> <p>PPIase A (1.15)</p> <p>Alpha(B)-crystallin (1.32)</p> <p>HSP84 (0.82)</p> <p>Protein disulfide-isomerase A3 (0.91)</p> <p>Heat shock cognate 71 kDa protein (0.91)</p> <p>HSP86 (0.81)</p> <p>Endoplasmic (0.89)</p> <p>Chaperonin 10 (0.86)</p> <p>Chaperonin 60 (0.89)</p> <p>Hsc70-interacting protein (0.91)</p> <p>TCP-1-delta (0.77)</p> <p>Calreticulin (0.88)</p> <p>Calnexin (0.86)</p> <p>GRP-78 (0.95)</p>
	<p><b>Highlighted proteins</b></p> <p>SERCA1 (1.67)</p> <p>ANT1 (0.73)</p> <p>Creatine kinase M-type (0.88)</p> <p>V-type proton ATPase subunit H (0.67)</p> <p>MUP (0.24)</p>

**Table 10.** List of highlighted proteins from SCN with the corresponding fold change ratio and grouped by functional clusters.

<b>SCN</b>	
<b>Oxidative stress</b>	<b>Acute-phase response (positive)</b>
GSTM2 (0.69)	Haptoglobin (1.81)
IDH2 (0.9)	Orosomucoid 1 (1.51)
SOD1 (1.17)	Complement C3 (1.59)
Thioredoxin (1.22)	Hemopexin (1.41)
Glutaredoxin-1 (1.19)	Inter-alpha-inhibitor heavy chain 4 (1.44)
Glyoxalase I (1.26)	
Peroxiredoxin-1 (1.06)	<b>Acute-phase response (negative)</b>
Peroxiredoxin-6 (1.2)	Serum albumin (0.75)
Peroxiredoxin-5 (1.23)	Alpha-2-HS-glycoprotein (0.89)
Peroxiredoxin-2 (1.09)	
	<b>Inflammatory markers</b>
<b>Glycolytic pathway</b>	S100-A9 (1.35)
Phosphoglucose isomerase (0.81)	Ig light chain kappa (C region) (1.89)
Phosphofructokinase (0.87)	Ig heavy chain gamma 2B (C region) (1.89)
Beta enolase (0.46)	Ig heavy chain gamma 2A (C region) (1.71)
Phosphoglycerate mutase 2 (0.54)	Ig heavy chain gamma 1 (C region) (1.46)
Phosphoglycerate kinase 1 (0.86)	
GAPDH (0.85)	<b>Protein folding</b>
Fructose biphosphate aldose 1 (0.71)	PP1ase A (1.15)
	Alpha(B)-crystallin (1.18)
<b>TCA cycle</b>	Prostaglandin E synthase 3 (1.19)
Aconitase (0.89)	HspB1 (1.09)
Dihydroliipoamide succinyltransferase (E2) (0.72)	Heat shock cognate 71 kDa protein (1.06)
	TCP-1-alpha (1.27)
<b>Lipid catabolism</b>	Protein disulfide-isomerase A3 (0.91)
Acetyl-CoA acetyltransferase (1.18)	PDI (0.93)
Perilipin-1 (0.76)	HSP84 (0.88)
Monoglyceride lipase (1.52)	GRP-78 (0.88)
Ras-related protein Rab-7a (1.10)	
Enoyl-CoA delta isomerase I (1.76)	<b>Highlighted proteins</b>
	SERCA1 (0.63)
<b>Lipid biosynthesis</b>	ANT1 (0.73)
Fatty acid synthase (0.50)	Creatine kinase M-type (0.39)
NADH-cytochrome b5 reductase 3 (0.83)	MUP (0.31)
NADP-dependent malic enzyme (0.68)	
<b>Muscle-type and cytoskeleton proteins</b>	
Myosin heavy chain-4 (0.51)	
Myosin light chain-1 (0.54)	
Tropomyosin-1 (0.66)	
Tropomyosin-2 (0.52)	
Myosin regulatory light chain 2 (0.56)	
Actin (0.34)	
Neurofilament light polypeptide (1.11)	
Neurofilament heavy polypeptide (1.11)	
Tubulin beta-5 chain (1.25)	
Tubulin beta-2A chain (1.74)	
Tubulin alpha-4A chain (1.56)	
Tubulin beta-4B chain (1.36)	
Tubulin beta-4A chain (1.18)	
Tubulin beta-3 chain (1.23)	
Tubulin alpha-1A chain (1.29)	
Spectrin beta chain (1.10)	
Spectrin alpha chain (1.17)	
Moesin (1.21)	



In addition to the detailed functional clusters, some interesting proteins were highlighted, such as SERCA1, ANT1, V-ATPase subunit H and MUP.

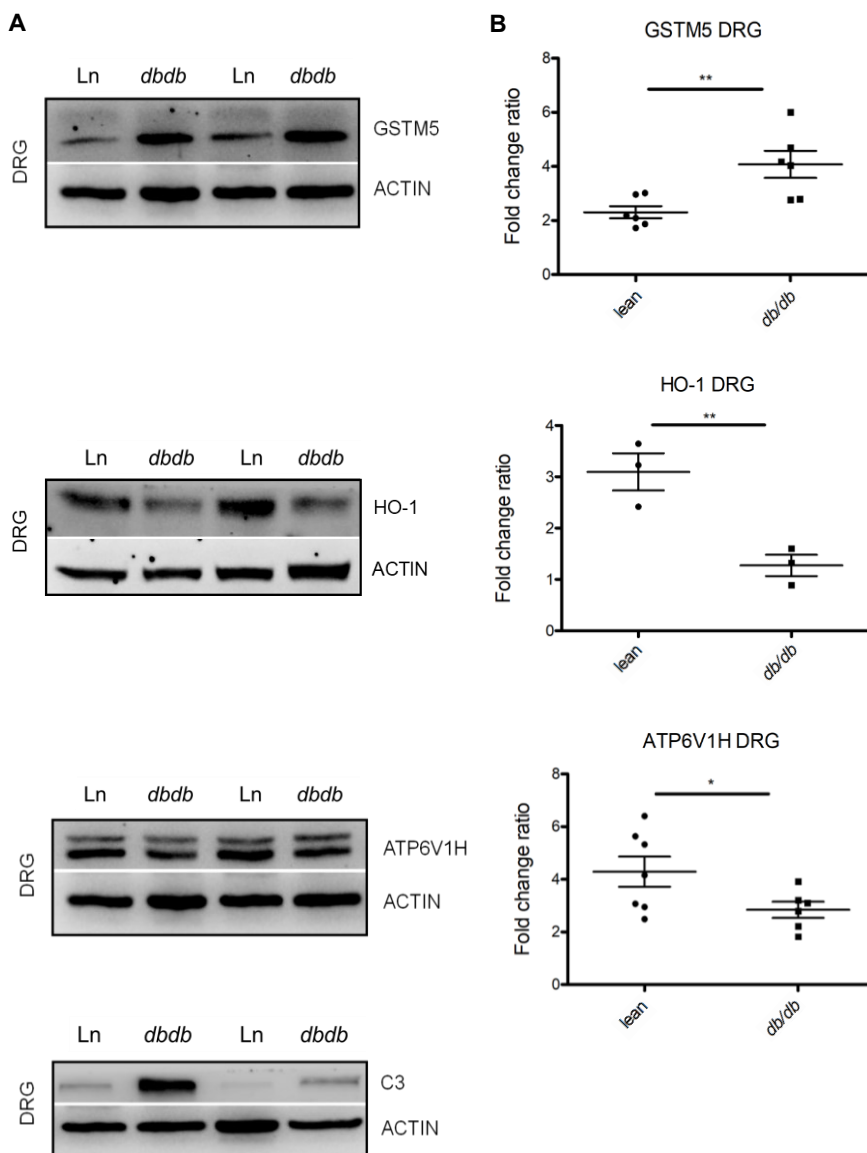
SERCA1 (Sarcoplasmic/endoplasmic reticulum calcium ATPase 1) is an intracellular membrane-bound enzyme that catalyses the hydrolysis of ATP to transport  $\text{Ca}^{2+}$  against a concentration gradient from the cytosol into the sarcoplasmic reticulum. Since protein folding is  $\text{Ca}^{2+}$ -dependent, calcium depletion in the endoplasmic reticulum lumen leads to protein misfolding [102]. SERCA1 was increased in DRG but downregulated in SCN. In agreement with this observation, several molecular chaperones were moderately dysregulated in DRG and SCN such as PPIase A, alpha(B)-crystallin, HSP84, protein disulfide-isomerase A3, heat shock cognate 71 kDa protein and GRP-78.

Related to energy depletion, ANT1 (ADP/ATP translocase 1), which forms a channel in the inner mitochondrial membrane that allows the translocation of ADP into the mitochondrial matrix and ATP from the mitochondrial matrix into the cytoplasm, was downregulated in both tissues. Interestingly, we also observed lower levels of creatine kinase M-type. This enzyme catalyses the reversible interconversion of creatine into phosphocreatine which is used to keep constant global and local ATP/ADP ratio [172]. ATP exhaustion is probably also the cause of the downregulation of V-type proton ATPase subunit H in DRG proteome, which was validated by western blot in both DRG and SCN tissues (**Fig. 37, 38**). V-type proton ATPase subunit H is a component of vacuolar ATPase, a multisubunit enzyme responsible for the establishment and maintenance of the acidic pH of endocytic and secretory organelles, pumping cytosolic  $\text{H}^+$  into their lumen. Hence, V-ATPase has a role in protein

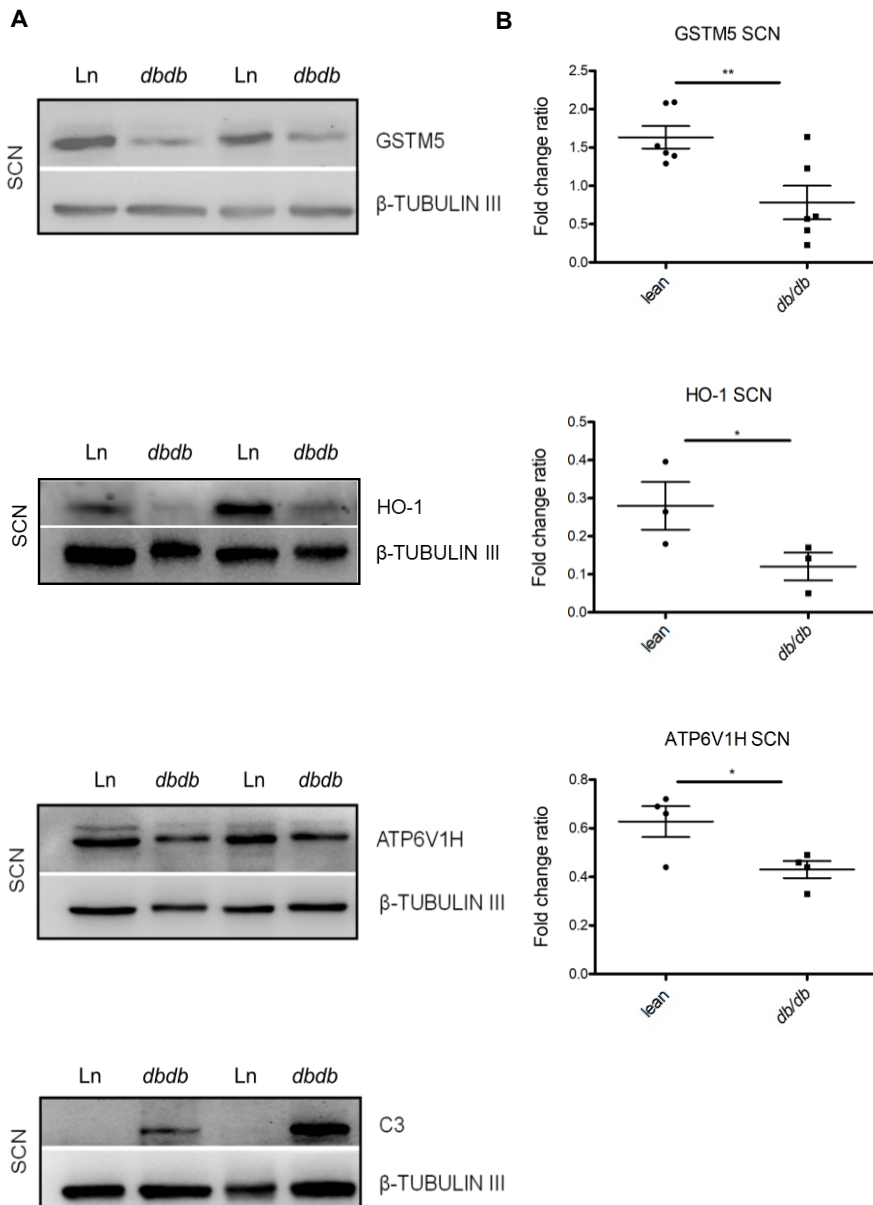
processing and degradation by lysosomes, endocytosis and vesicular traffic as well as synaptic vesicle loading, driven by the electrochemical gradient [173].

Interestingly, MUP (major urinary protein) was the most depleted protein in DRG and the second most downregulated in SCN. MUP is a lipocalin family member secreted to circulation by the liver and filtered by the kidneys into the urine. The main role of MUP proteins is the binding to pheromones and other lipophilic molecules to regulate their transport and release into the air from urine marks [174]. Initially we thought that MUP detection in DRG and SCN was the result of uptake from the circulation or a contamination from blood. Therefore, aiming to elucidate MUP origin, we checked whether *Mup* mRNA was detectable in these tissues. By Real-Time PCR (polymerase chain reaction), we were able to detect *Mup* in both samples and, in agreement with our proteomic results, *Mup* expression was much lower in DRG and SCN from BKS-*db/db* compared to lean. More importantly, the decrease in expression was dependent on the time of diabetes in DRG (**Fig. 39A**). In SCN, *Mup* expression is almost absent already at 1 week of diabetes, pointing at a very early effect of metabolic syndrome (**Fig. 40A**). This result was corroborated by western blot (**Fig. 39B, 39C, 40B, 40C**) as well as by immunohistochemistry in both tissues (**Fig. 41**). Moreover, we decided to investigate MUP localization in the PNS by immunostaining. MUP does not colocalize with neuronal somas nor satellite cells in DRG (**Fig. 42A**), and neither axons nor Schwann cells in SCN (**Fig. 42B**). Alternatively, we detected MUP in the extracellular space, colocalizing with connective tissue in DRG and with endoneurium in SCN, as observed by collagen IV colocalization

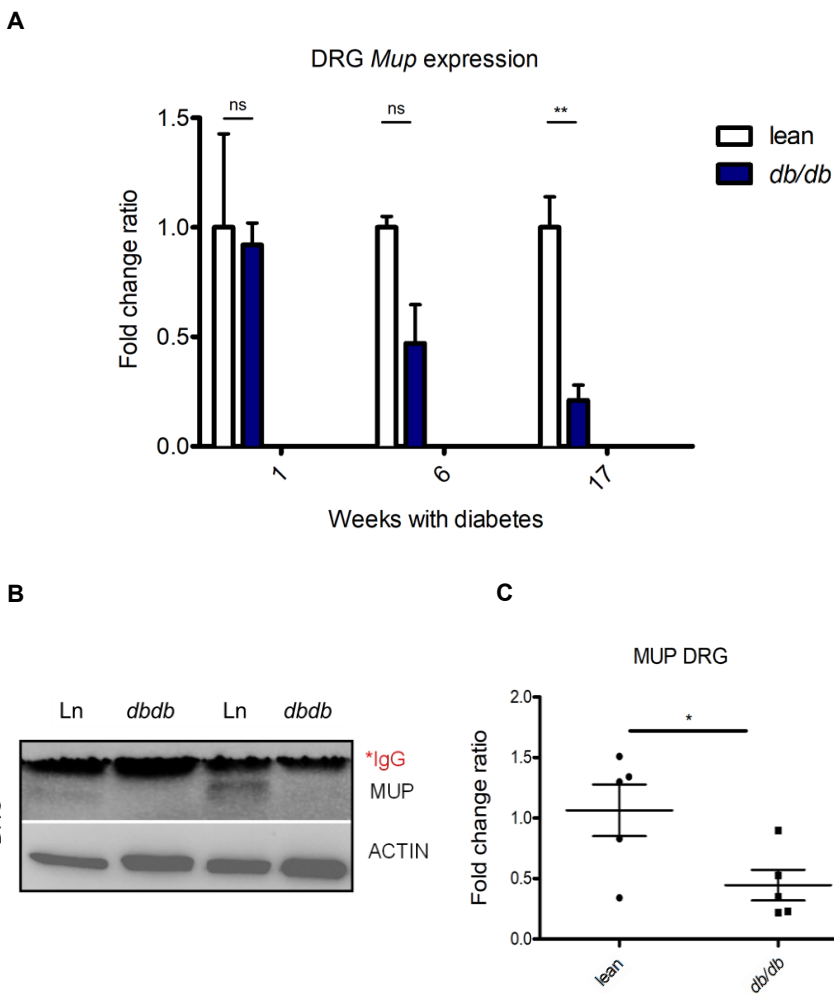
(yellow signal) (**Fig. 43**), which adds relevance to the important changes found in proteins related to extracellular space.



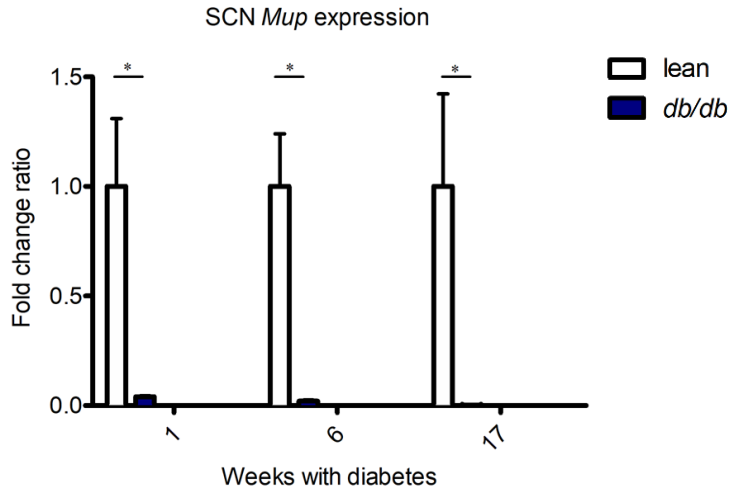
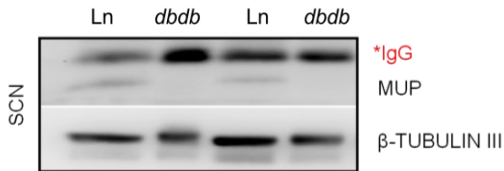
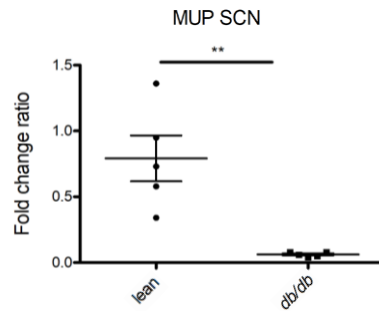
**Figure 37.** Western blot validation of DRG proteomic data. **(A)** GSTM5, HO-1, ATP6V1H and C3 proteins were selected to validate proteomic results using blot immunodetection based on their relevance in oxidative stress, synapsis and inflammation, respectively. Representative western blots of these proteins are shown for DRG at 15 weeks of diabetes. **(B)** Quantification of western blot data normalised to ACTIN as housekeeping. N = 3-7 mice per group. \* $p < 0.05$ , \*\* $p < 0.01$  by Student's t test.



**Figure 38.** Western blot validation of SCN proteomic data. **(A)** GSTM5, HO-1, ATP6V1H and C3 proteins were selected to validate proteomic results using blot immunodetection based on their relevance in oxidative stress, synapsis and inflammation, respectively. Representative western blots of these proteins are shown for SCN at 15 weeks of diabetes. **(B)** Quantification of western blot data normalised to  $\beta$ -TUBULIN III as housekeeping. N = 3-6 mice per group. \* $p < 0.05$ , \*\* $p < 0.01$  by Student's t test.



**Figure 39. (A)** *Mup* gene expression evaluation by Real-Time PCR in DRG at three different time points (one, six and seventeen weeks after diabetes onset). Fold change ratio normalised to lean mice. N = 3-4 animals per group. \*\* $p < 0.01$ , two-way ANOVA followed by Bonferroni's Post hoc test. **(B)** Western blot validation of MUP downregulation for DRG at 15 weeks of diabetes. **(C)** Quantification of western blot data normalised to ACTIN as housekeeping. N = 5 animals per group. \* $p < 0.05$ , by Student's t test.

**A****B****C**

**Figure 40.** (A) *Mup* gene expression evaluation by Real-Time PCR in SCN at three different time points (one, six and seventeen weeks after diabetes onset). Fold change ratio normalised to lean mice. N = 3-4 animals per group. \* $p < 0.05$ , two-way ANOVA followed by Bonferroni's Post hoc test. (B) Western blot validation of MUP downregulation for SCN at 15 weeks of diabetes. (C) Quantification of western blot data normalised to  $\beta$ -TUBULIN III as housekeeping. N = 5 animals per group. \*\* $p < 0.01$ , by Student's t test.

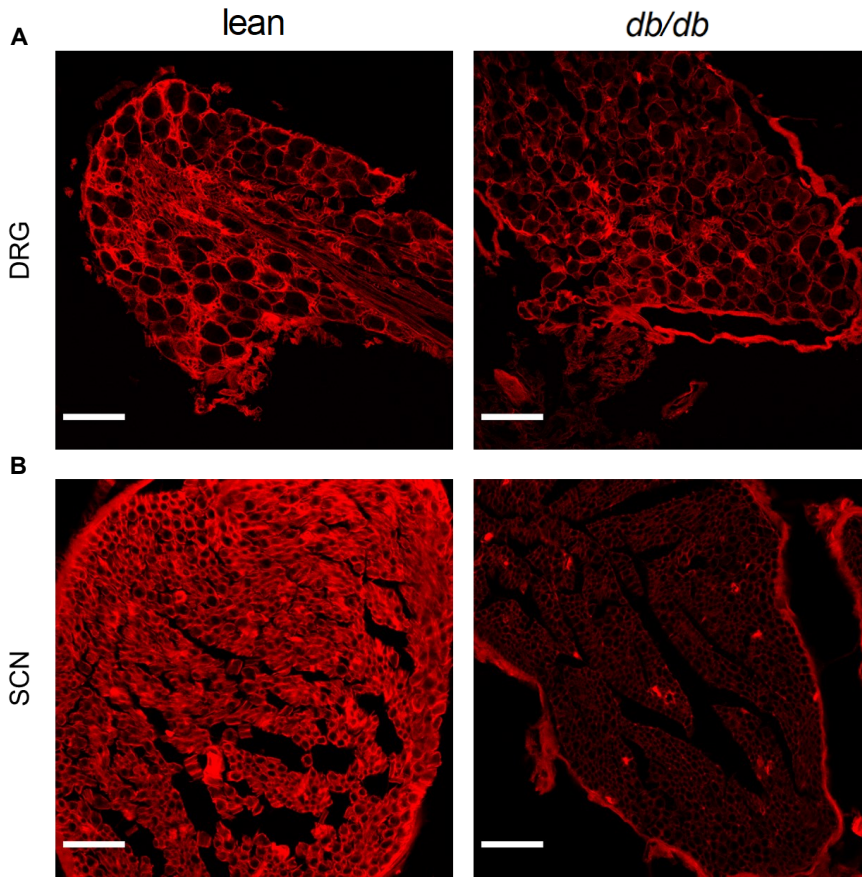


**Figure 41.** Representative confocal images of MUP signal in DRG (A) and sciatic nerve (B) from *db/db* mice at 15 weeks of diabetes and lean control. Scale bar = 100  $\mu$ m (A), 50  $\mu$ m (B).

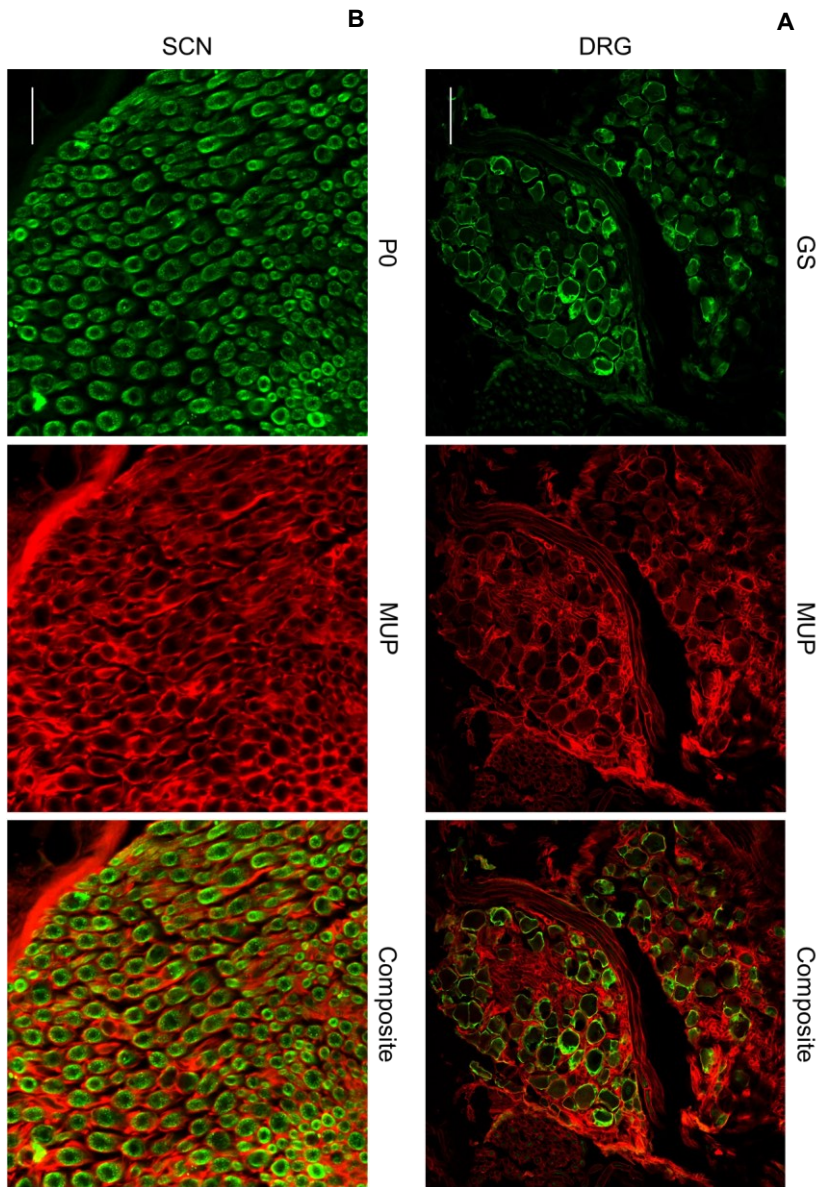


**Figure 42.** Colocalization assessment of MUP (red) with satellite cells (glutamine synthetase (GS) = green) in DRG (**A**) and Schwann cells (P0 = green) in SCN (**B**). Absence of yellow signal indicates no colocalization. Scale bar = 100  $\mu\text{m}$  (**A**), 25  $\mu\text{m}$  (**B**).



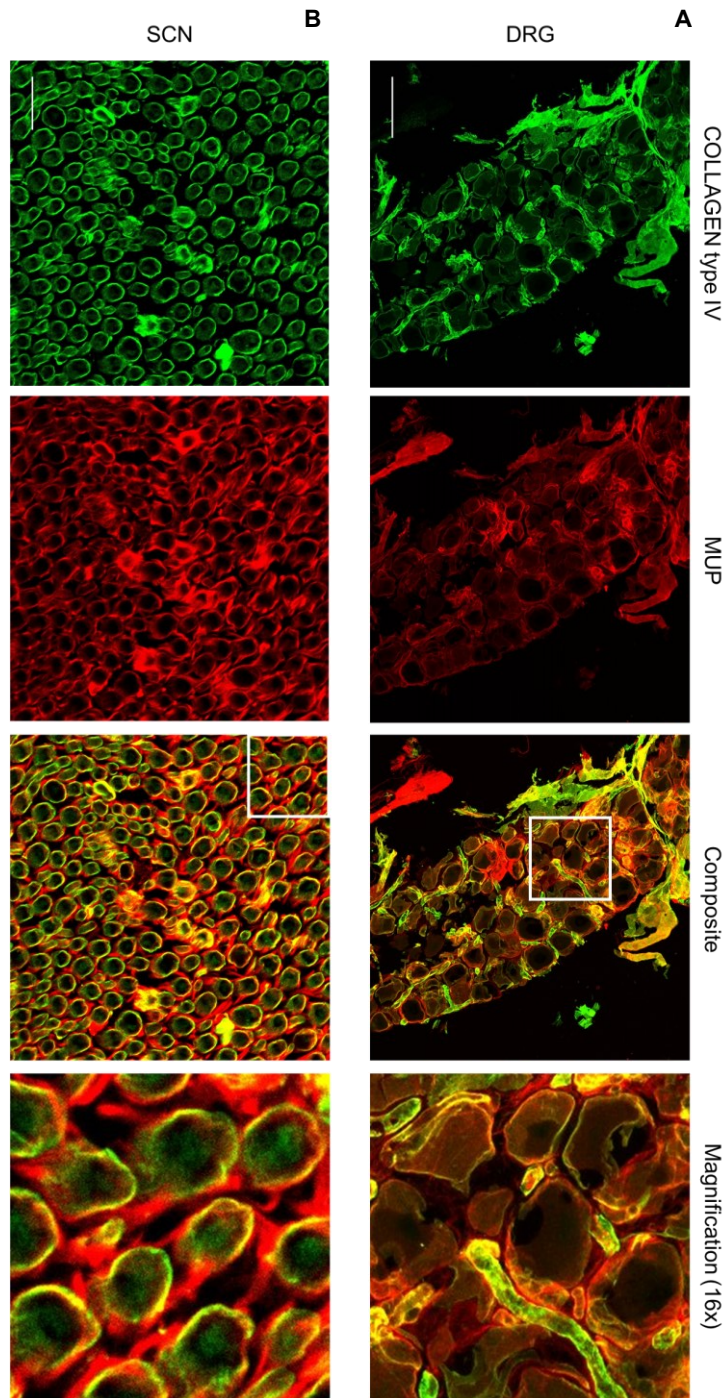


**Figure 43.** Colocalization assessment of MUP (red) with the extracellular matrix (collagen type IV = green) in DRG (**A**) and SCN (**B**). Presence of yellow signal indicates colocalization. Scale bar = 100  $\mu$ m (**A**), 25  $\mu$ m (**B**).

#### 4. IN VITRO AND IN VIVO STUDY OF MUP FUNCTION IN PNS

While we have characterised the effect of diabetes on *Mup* expression as well as its localization in DRG and SCN, the function of this protein in the PNS is largely unknown.

As previously explained, major urinary proteins belong to lipocalin family whose members play a role in physiological processes by binding and transporting small hydrophobic molecules. Interestingly, AGP1 (orosomucoid 1), a positive acute phase protein found upregulated in our data set, has also been classified as a member of the lipocalin family [175]. Indeed, MUP shares a high structural similarity with AGP1 as observed by the pairwise alignment of both three-dimensional structures despite low sequence identity (**Fig. 44**). In addition, acute phase proteins can be found in the extracellular matrix of PNS as well as we observed for MUP [176; 177].

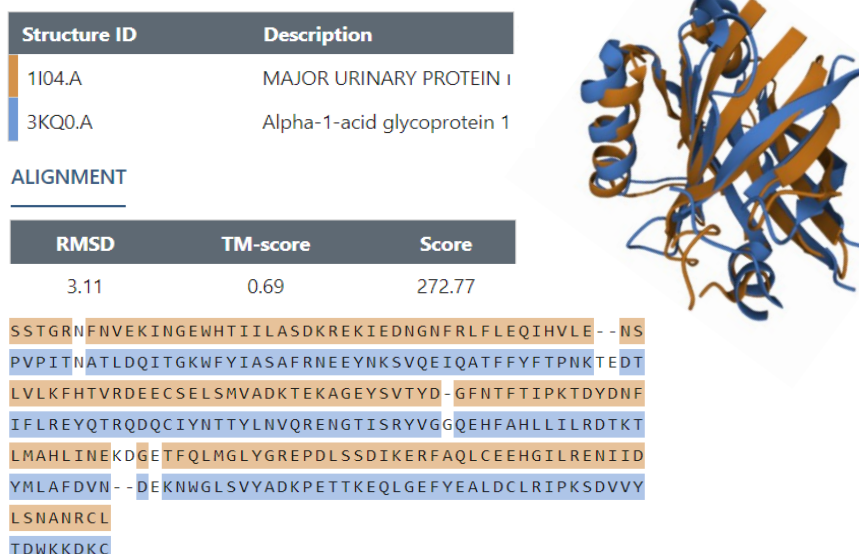


**Figure 44.** Pairwise structure alignment of MUP1 (1I04) and AGP1 (3KQ0) three-dimensional structures using a PDB tool. TM-score ranges between 0 and 1, where 1 indicates a perfect match and 0 is no match between the two structures. Scores >0.5 normally indicates common protein fold.

Despite MUP and AGP1 share similar conformations, fold change ratios were completely opposite. Nonetheless, since it has been described that AGP suppresses inflammation and ROS generation in adipocytes and macrophages *in vitro* [178], we decided to test whether MUP was able to modify oxidative stress *in vitro*.

For this purpose, we first cloned *Mup* cDNA, obtained from sciatic nerves, into an expression vector driven by the strong and ubiquitous CAG promoter. Since multiple isoforms of MUP exist, we designed a pair of primers able to amplify almost all of them. Once we got the final plasmid, we wanted to validate whether MUP protein is properly produced and secreted. Thus, we transfected this plasmid into a HEK293 cell line due to its outstanding transfection efficacy, using a CAG-*Gfp* (green fluorescent protein) plasmid as a control. We confirmed by western blot that MUP protein is secreted into medium upon cell transfection and exhibit the expected molecular weight (21 kDa) (**Fig. 45**).

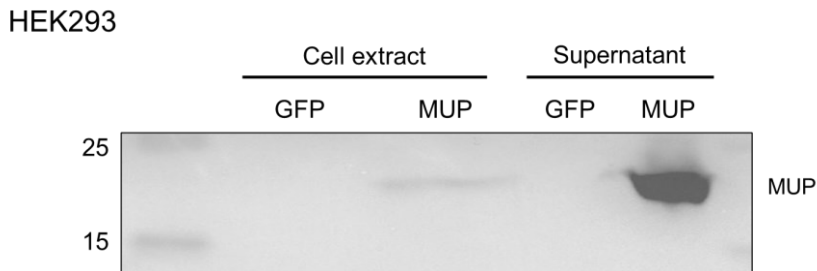


**Figure 45.** MUP immunodetection in HEK293 extracts and collected media by western blot after transfection with CAG-*Gfp* or CAG-*Mup* plasmid.

Then, we used DRG cell line MED17.11 to address the role of MUP on oxidative stress. We chose MED17.11 cell line since exhibits a robust phenotype that closely resembles sensory neurons. Unfortunately, the transfection efficacy of MED17.11 was poor, leading to a deficient protein production. Therefore, we planned to

produce MUP protein in HEK293, collect the supernatant, and expose it to MED17.11 in addition to oxidant insults such as hydrogen peroxide or tert-Butyl hydroperoxide (tBHP). Using the DCFDA dye, we proved that ROS levels increased upon exposure to hydrogen peroxide and, largely, to tBHP. Nonetheless, MUP-containing supernatant was unable to counteract the oxidative stress induced in MED17.11 (data not shown).

We further tested the effect of MUP on this cell line by MTT assay aiming to elucidate whether MUP could affect cell viability upon oxidant insults. As observed for oxidative stress assay, no differences were obtained compared to control supernatant (data not shown).

Since no positive results were obtained by *in vitro* studies, we planned as next step to study the function of MUP *in vivo*. Two main strategies were suitable to address this question: 1) overexpression of *Mup* in BKS-*db/db* mice, and 2) *Mup* silencing in wt mice using a short hairpin RNA (shRNA). Considering the high costs associated with *db/db* purchase and maintenance, we finally decided to design a shRNA strategy aiming to evaluate whether *Mup* downregulation has a role in neuropathy development.

Using GenScript and InvivoGen softwares, we designed three different shRNA sequences targeting *Mup* mRNA. Several parameters including total length, GC content, and nucleotide motifs were considered in the *in silico* approach. Once we cloned these shRNA sequences in an expression vector driven by the H1 promoter, we wanted to determine which shRNA sequence exhibited higher silencing efficacy. Hence, we followed the *in vitro* strategy presented in **Figure 46**.

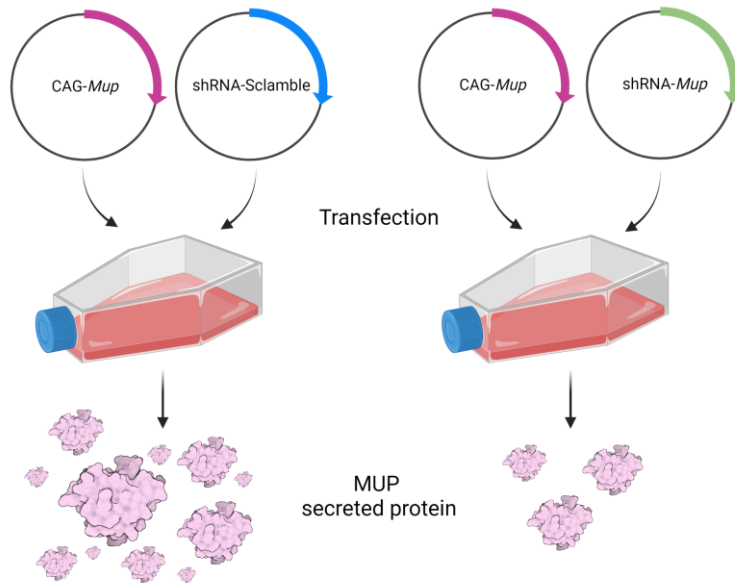


**Figure 46.** *In vitro* strategy to test the silencing efficacy of different shRNA against *Mup*. HEK293 cells were double transfected with a CAG-*Mup* plasmid and a shRNA-Scramble (control) or shRNA-*Mup*. MUP-containing supernatant was collected and analysed by western blot.

Western blot analysis of MUP-containing supernatant enabled us to determine the best shRNA candidate achieving a remarkable *Mup* silencing compared to shRNA-Scramble (control) (**Fig. 47**).

HEK293

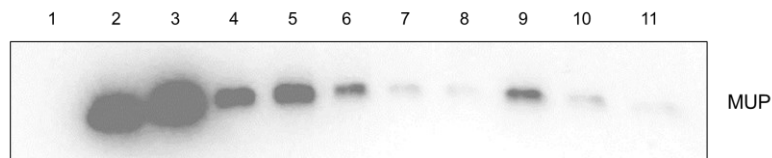


**Figure 47.** MUP immunodetection in HEK293 supernatant after following conditions: **1.** No transfection. **2.** Transfection 2  $\mu$ g CAG-*Mup*. **3.** Transfection 4  $\mu$ g CAG-*Mup*. **4.** Transfection 2  $\mu$ g CAG-*Mup* + 8  $\mu$ g shRNA-Scramble. **5.** Transfection 4  $\mu$ g CAG-*Mup* + 8  $\mu$ g shRNA-Scramble. **6.** Transfection 2  $\mu$ g CAG-*Mup* + 4  $\mu$ g shRNA-*Mup*. **7.** Transfection 2  $\mu$ g CAG-*Mup* + 6  $\mu$ g shRNA-*Mup*. **8.** Transfection 2  $\mu$ g CAG-*Mup* + 8  $\mu$ g shRNA-*Mup*. **9.** Transfection 4  $\mu$ g CAG-*Mup* + 4  $\mu$ g shRNA-*Mup*. **10.** Transfection 4  $\mu$ g CAG-*Mup* + 6  $\mu$ g shRNA-*Mup*. **11.** Transfection 4  $\mu$ g CAG-*Mup* + 8  $\mu$ g shRNA-*Mup*.

As soon as we validated the shRNA against *Mup*, we proceeded with viral vector production to transduce PNS *in vivo*. As previously presented, intrathecal injection is one of the best approaches to target PNS with high efficiency while avoiding neutralizing antibodies from system circulation. Our group previously demonstrated the ability of AAVrh10 to efficiently transduce DRG after intrathecal administration [112]. **Figure 48** shows AAVrh10 tropism for DRG and SCN in ICR mice after intrathecal administration of an AAVrh10-*Gfp* vector while **Figure 49** demonstrates axonal and Schwann cell transduction in sciatic nerve.

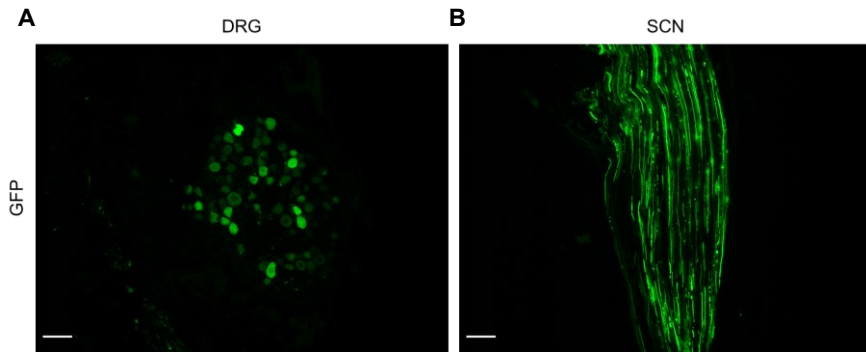


**Figure 48.** Representative fluorescence images of GFP signal in DRG (A) and SCN (B) after intrathecal administration of an AAVrh10-*Gfp* vector. Scale bar = 100  $\mu$ m.

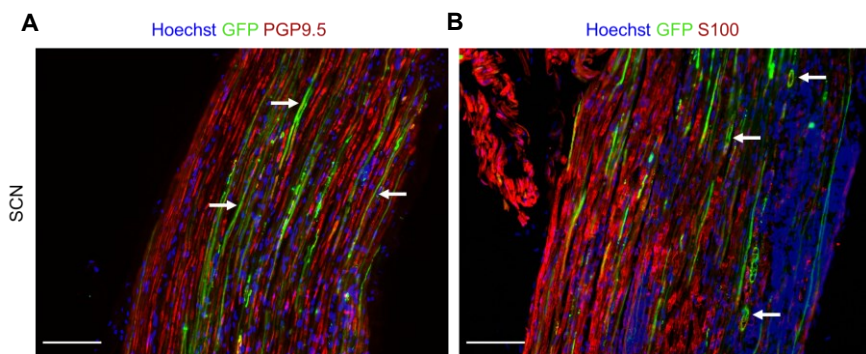


**Figure 49.** Representative fluorescence images of SCN harvested from AAVrh10-*Gfp* intrathecally injected mice. It is shown GFP signal (green) with PGP9.5-labelled axons (red) (A) or S100-labelled Schwann cells (red) (B). Arrows indicate some GFP-positive axons (A) and GFP-positive Schwann cells (B). Scale bar = 100  $\mu$ m.

Thus, AAVrh10-shRNA against *Mup* as well as AAVrh10-shRNA-Scramble were produced and administered intrathecally in ICR mice at three months of age. This experiment is currently ongoing with only preliminary data to show.

All animals were tested for electrophysiological alterations, observing, in just seven weeks, a significant reduction in distal sensory nerve conduction velocity (**Fig. 50**).

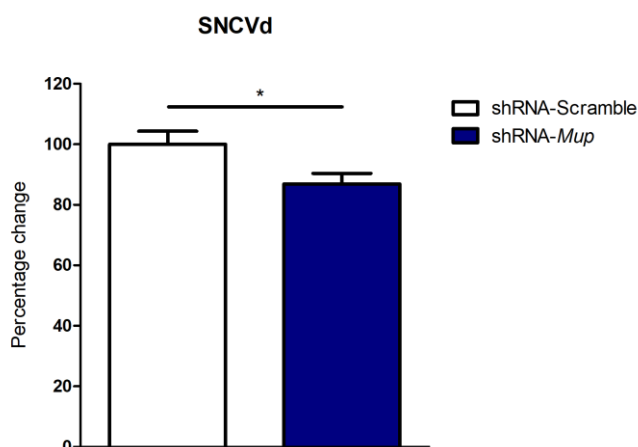


**Figure 50.** Evaluation of distal sensory nerve conduction velocity by electrophysiological study of the sciatic nerve in intrathecally injected ICR mice with AAV-shRNA-Scramble or AAV-shRNA-*Mup* (7 weeks after administration). Data are expressed as percentage of change compared to scramble. N = 8 scramble, 8 *Mup*. \* $p < 0.05$ , by Student's t test.

## 5. AAV9-*Kl* AS A THERAPEUTIC APPROACH FOR DN

KLOTHO is a pleiotropic hormone involved in neuroprotection by modulating neuroinflammation, oxidative stress and myelination. *Kl* gene is mainly expressed in the kidney and the brain, although low expression levels are also found in skeletal muscle, urinary bladder, testis and ovary and pancreas [179]. *Kl* presents two different mRNA splice variants, one codifying for a full-length transmembrane isoform (m-KL) containing the KL1 and KL2

domains, and another codifying for a secreted isoform (s-KL) containing the KL1 domain plus an extra tail. Transmembrane isoform can be processed into a soluble form (p-KL) or further cleaved to soluble p-KL1 and p-KL2. These variants exhibit different expression levels as well as spatio-temporal profiles, suggesting that may be involved in different roles [180].

KLOTHO is extensively known as an anti-aging hormone capable of extending life span in mice when overexpressed [181]. Conversely, *Kl* silencing leads to a remarkably short survival [179]. One of the mechanisms involved in KLOTHO-mediated delaying of ageing is its antioxidant properties. It has been described that KLOTHO mediates FOXOs activation which is involved in the upregulation of antioxidant genes [182]. In addition, other papers found that NRF2, another master regulator of antioxidant response, is also activated upon KLOTHO signalling [183; 184].

Moreover, *in vitro* studies using different cell lines have demonstrated that KLOTHO could ameliorate the unfolded protein response induced by thapsigargin [185].

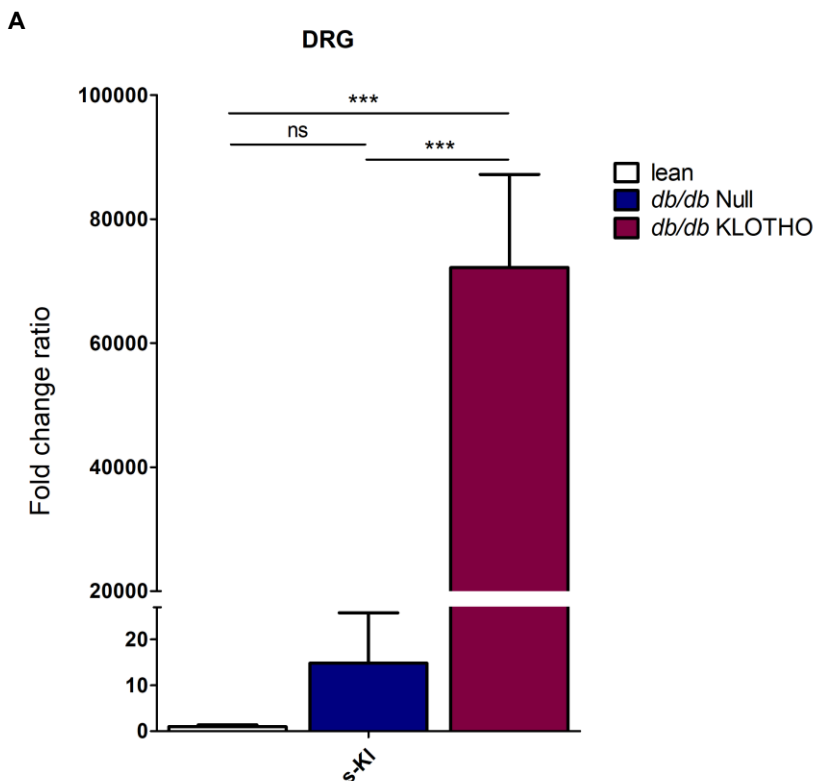
Interestingly, it has also been reported a role for KLOTHO in CNS myelination after observing myelin abnormalities in *Kl* knock-out mice [186].

Considering the neuroprotective properties of KLOTHO, we decided to test whether this anti-aging molecule could be a therapeutic approach to treat oxidative stress and inflammation in *db/db* mice. Since we pursued a widespread biodistribution of KLOTHO throughout the PNS, we selected the s-KL isoform which is directly secreted to the cerebrospinal fluid (CSF). Thus, even low transduction efficiency would be sufficient to achieve whole-tissue



correction. AAV9 codifying for s-KL was kindly provided by Joan Roig from Dr. Miguel Chillón laboratory to perform this experiment. As previously explained, AAV9 serotype efficiently transduces DRG neurons in mice and nonhuman primates after intrathecal administration [157; 158]. Thus, AAV9-s-*Kl* was administered by intrathecal injection to *db/db* mice at two months of age. As a control, lean and *db/db* animals were injected with an AAV9-Null vector at the same time.

We demonstrated by quantitative PCR (qPCR) that AAV9-*Kl* properly transduced DRG and SCN, achieving high levels of *Kl* expression at 26 weeks of age. As expected, transduction efficiency was much higher in DRG compared to SCN (**Fig. 51**).



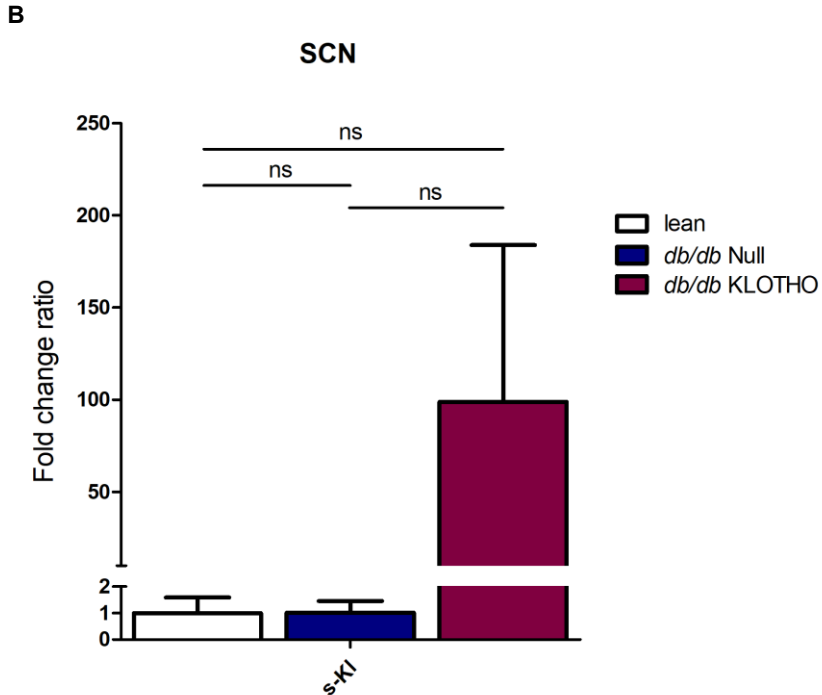


**Figure 51.** Quantification of *s-KI* mRNA expression by qPCR in DRG (A) and SCN (B) at 26 weeks of age (4 months after injection). Fold change ratio normalised to lean mice. N = 4 lean (null), 4 *db/db* (null), 4 *db/db* (KLOTTHO). \*\*\*p < 0.001, one-way ANOVA followed by Tukey's Post hoc test.

As we previously did to characterise *db/db* neuropathy, we performed electrophysiological and sweating tests at 25 weeks of age (17 weeks with diabetes) to evaluate whether KLOTTHO could ameliorate the neuropathic phenotype. Unfortunately, high mortality exhibited by *db/db* mouse lead to small number of animals in this experiment. Hence, most results obtained did not reach statistical significance, though consistent tendencies were noticeable with the consequent loss of significance between lean and *db/db* after treatment.

Sciatic nerve from *db/db* mice demonstrated the expected reduction in motor and sensory nerve conduction velocities as well as lower

CMAP amplitude (**Fig. 52, 53**). Also, reduced NCV was observed for caudal nerves from the tail (**Fig. 54**). Interestingly, we detected in KLOTHO-treated animals a marked tendency to recover the lower CMAP and MNCV observed in null-treated *db/db* (**Fig. 52**).

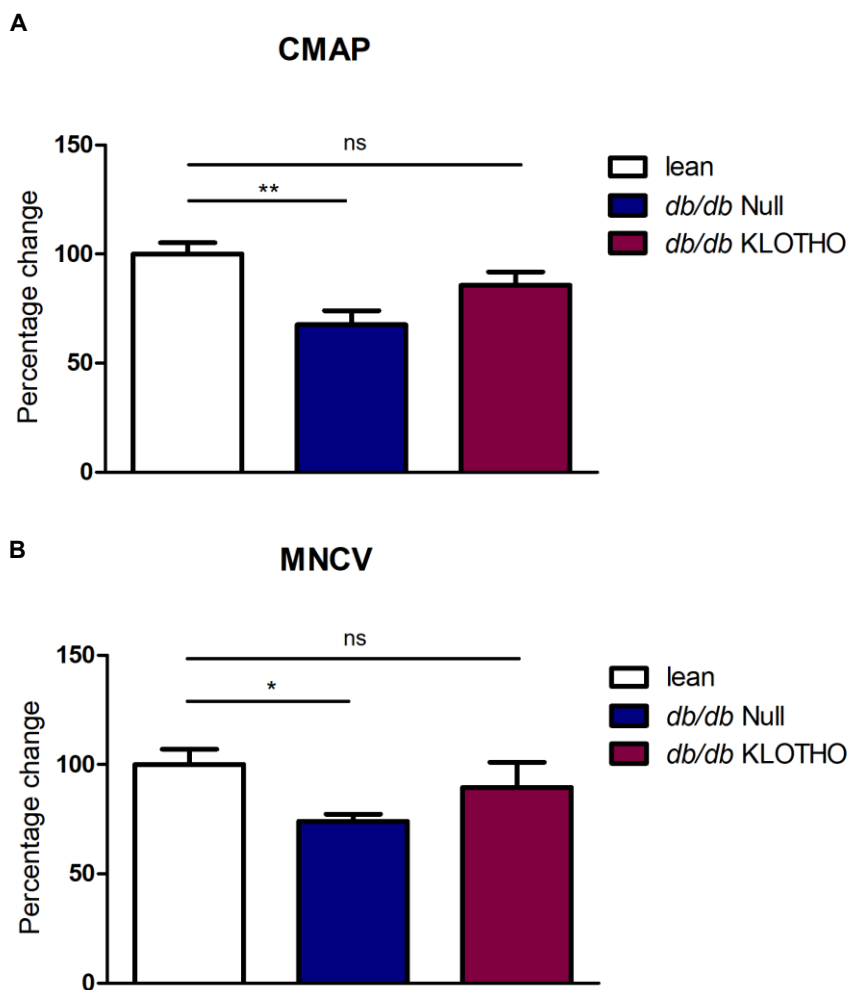


**Figure 52.** Evaluation of compound muscle action potential (**A**) and motor nerve conduction velocity (**B**) by electrophysiological study of the sciatic nerve at 17 weeks with diabetes. Data are expressed as percentage of change compared to lean mice. N = 8-9 lean (null), 9 *db/db* (null), 4 *db/db* (KLOTHO). \* $p < 0.05$ , \*\* $p < 0.01$ , one-way ANOVA followed by Tukey's Post hoc test.

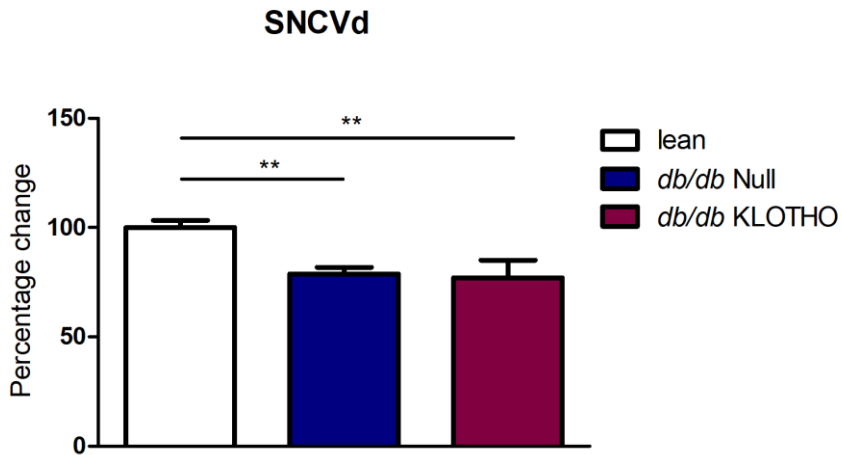


**Figure 53.** Evaluation of distal sensory nerve conduction velocity by electrophysiological study of the sciatic nerve at 17 weeks with diabetes. Data are expressed as percentage of change compared to lean mice. N = 10 lean (null), 9 *db/db* (null), 4 *db/db* (KLOTTHO). \*\*p < 0.01, one-way ANOVA followed by Tukey's Post hoc test.

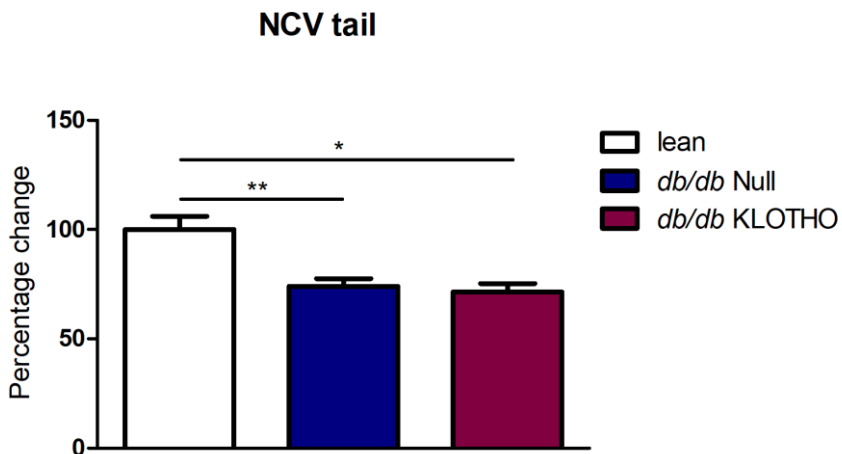


**Figure 54.** Evaluation of sensory nerve conduction velocity by electrophysiological study of the caudal nerves at 17 weeks with diabetes. Data are expressed as percentage of change compared to lean mice. N = 10 lean (null), 9 *db/db* (null), 3 *db/db* (KLOTTHO). \*p < 0.05, \*\*p < 0.01, one-way ANOVA followed by Tukey's Post hoc test.

Then, we analysed by subcutaneous injection of pilocarpine whether KLOTTHO could affect the sudomotor function in *db/db* mice. Based on the number of active sweat glands after the treatment, sudomotor

function was not significantly improved by KLOTHO administration, although a notable tendency was noticed (**Fig. 55**). As explained above, high mortality associated with *db/db* model hindered the obtaining of significant results in this analysis. On the other hand, the differences observed between lean and *db/db* mice were consistent with what we have previously described.

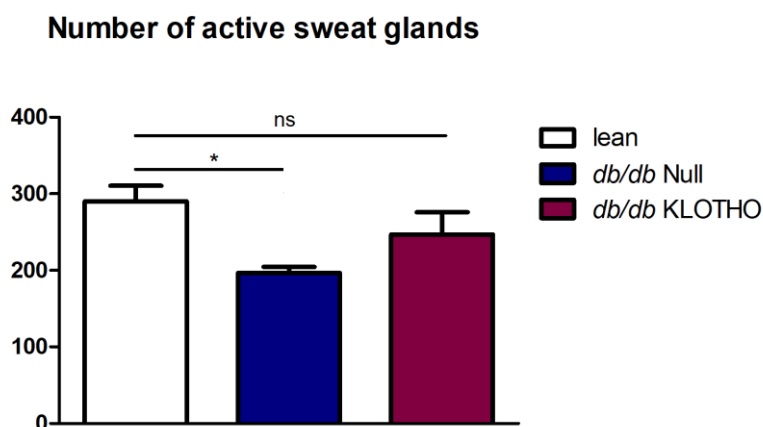


**Figure 55.** Quantification of number of active sweat glands (sweat droplets number) from silicone moulds at 10 minutes after pilocarpine administration (at 17 weeks with diabetes). N = 4 lean (null), 4 *db/db* (null), 4 *db/db* (KLOTHO). \* $p < 0.05$ , one-way ANOVA followed by Tukey's Post hoc test.

Since electrophysiological and sweating tests showed a trend to ameliorate some features of neuropathy, we analysed by qPCR whether this molecule was inducing the expression of antioxidant genes as described. As shown in **figure 56**, a tendency to upregulation could be observed for some antioxidant genes and for *Mup* expression. Unfortunately, small sample size prevents us to draw strong conclusions. Thus, larger *n* as well as western blot analysis of these genes would be necessary to elucidate whether KLOTHO could mediate any therapeutic effect at molecular level.

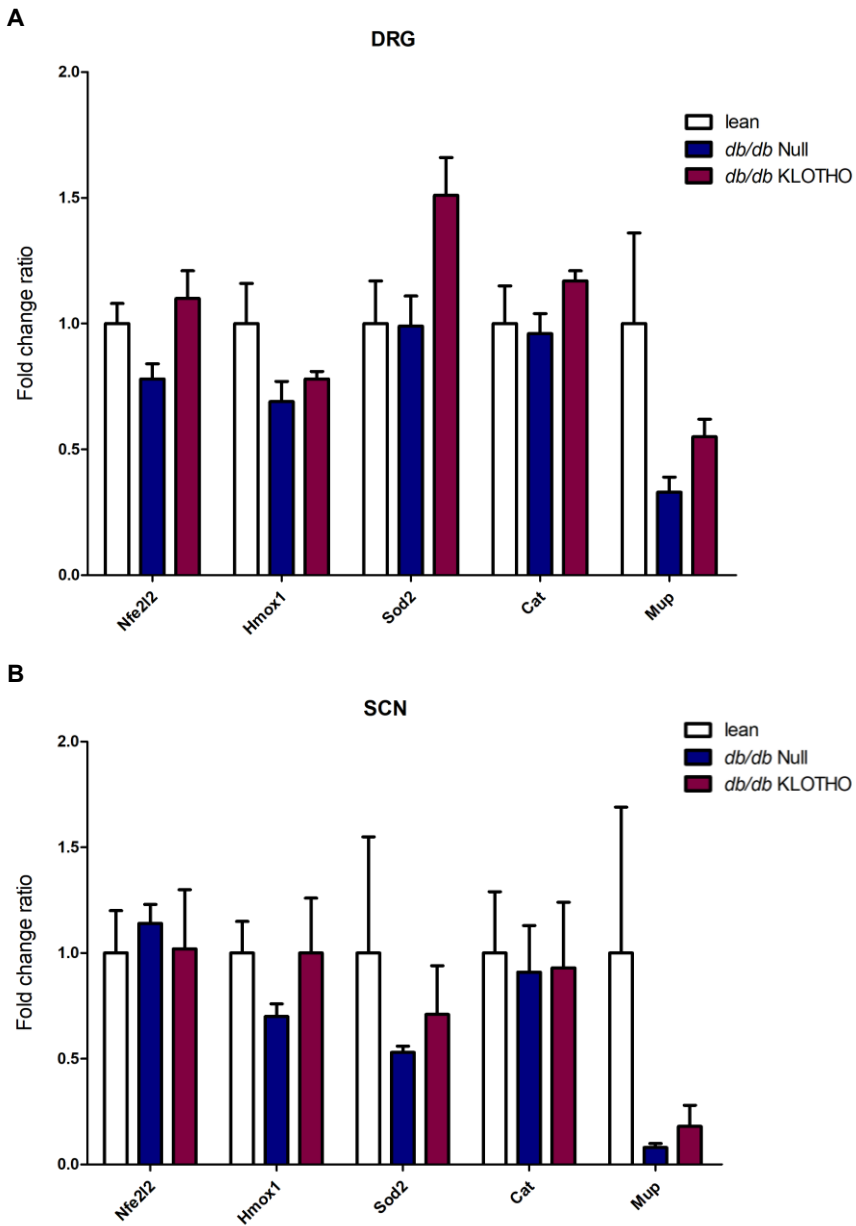


**Figure 56.** Quantification of *Mup* and antioxidant genes expression by qPCR in DRG (**A**) and SCN (**B**) at 26 weeks of age (4 months after injection). Fold change ratio normalised to lean mice. N = 4 lean (null), 4 *db/db* (null), 4 *db/db* (KLOTHO). NS (non-significant) not shown in the chart. One-way ANOVA followed by Tukey's Post hoc test.



## ***DISCUSSION***





## T2DM MOUSE MODEL

BKS-*Lep<sup>db/db</sup>* is the most studied model of diabetic neuropathy in T2DM research as it develops an early onset and robust neuropathy compared to DIO models. Furthermore, most studies using omics approaches have been done with *db/db* mice. For these reasons, we selected *db/db* mouse as the model of choice to conduct this thesis, aiming to facilitate further comparisons with published data.

As previously described [187; 188], we demonstrated that *db/db* mouse develops robust sensory and motor neuropathy comprising features of axonal degeneration and regeneration as well as demyelination. Such results were obtained by electrophysiological tests of the sciatic and caudal nerves, morphometric analysis of the tibial nerve and immunostaining of plantar pads. It is worth highlighting that even though human patients develop motor dysfunction at late stages, reduced CMAP and MNCV are early onset features in *db/db* mice.

Moreover, silicone impression and PGP9.5 immunolabelling of sweat glands enabled us to determine that this model also exhibits distal hypohidrosis confirming autonomic dysfunction. Liu et al. [189] also evaluated *db/db* mice sweating capacity, though using the iodine/starch based sweat assay. Under basal conditions, they observed considerable differences in PGP9.5-positive fibres density in sweat glands as well as reduced number of sweat droplets and slower rate of sweat droplet formation compared to control animals. Surprisingly, they described that sweating in *db/db* was not affected by pilocarpine. Conversely, despite obtaining same results, our data were collected after pilocarpine stimulation because, in our hands, *db/db* mice almost did not sweat under basal conditions. Thus,

pharmacological stimulus was necessary to study sudomotor function. Since plantar glands are activated upon emotional stress, this phenomenon may account for the unstressed behaviour of *db/db* mouse model.

An unexpected finding was the loss of weight of *db/db* mice after 3 months with diabetes which was consistent for all batches studied. Surprisingly, there is no prior report about this observation. Dalbøge et al. [190] monitored insulin levels in *db/db* mice from 5 to 34 weeks of age describing a progressive reduction of insulin secretion from 18 weeks of age (10 weeks with diabetes in their study). Interestingly, onset of insulin secretion impairment coincides with our observation of *db/db* starting to lose weight.

Besides the expensive purchase and maintenance cost, the main drawback of *db/db* mouse as a model is the high mortality rate that hinder to achieve enough number of animals, particularly, at advanced stages of diabetes, when animals exhibit a profound weight loss and critical metabolic impairment. Sataranatarajan et al. [191] performed a detailed pathological evaluation concluding that suppurative inflammation was the main cause of death in the *db/db* mice.

A potential strategy to reduce mortality would be to ameliorate the metabolic phenotype of *db/db* mice by pharmacological treatment. For instance, metformin administration could be a possible approach to resemble diabetes progression in human patients. Indeed, long-term metformin treatment in *db/db* mice improves plasma insulin and body weight due to less  $\beta$ -cell exhaustion and islet degeneration [192].

## PROTEOMIC STUDY

Omics approaches are of particular interest in deciphering the pathophysiological mechanisms and guiding the search for preventive strategies of diseases. Analysis of the peripheral nervous system proteome has enabled us to identify several altered pathways in BKS-*db/db* mice, with most relevance in those related to oxidative stress and unfolded protein response, metabolic dysregulation, translation, muscle-type and cytoskeleton proteins, and acute phase and inflammatory responses.

Several proteins involved in glutathione metabolism and antioxidant activity are altered in our study, supporting the hypothesis that **oxidative stress** has an important role in DN aetiology [133]. In the same model, Hinder et al. [72] described increased levels of 3-nitrotyrosine and hydroxyoctadecadienoic acids in DRG and SCN, markers of protein oxidation and lipid peroxidation, respectively. It is also remarkable the increase of glyoxalase I as it participates in the elimination of methylglyoxal, a toxic compound derived from glucose metabolism in hyperglycaemic conditions [193].

In diabetes, saturated fatty acids, nonenzymatic glycation and ROS reduced SERCA activity [77; 194; 195]. In agreement with these data, we found altered levels of SERCA1. However, while in SCN decreased fold change was observed, increased levels were found in DRG. Concomitantly, a mild dysregulation in several **molecular chaperones** was detected in both tissues, which might result in ER homeostasis disruption [196].

It is worth highlighting the unexpected finding that was the lack of activation of the unfolded protein response in diabetic PNS. Indeed, some folding chaperones exhibited lower levels compared to lean

animals. These findings are opposite to those observed in previous pilot studies we performed *in vitro*. Using the cell lines ND7/23 and NSC-34 as *in vitro* models of sensory and motoneurons, respectively, we tested the activation of unfolded protein response upon palmitate exposure for 12 hours. What we observed was a dose-response effect of palmitate on UPR markers such as *Hspa5* (BiP) and *Ddit3* (CHOP) mRNA upregulation, and *Xbp1* splicing activation (**Annexed fig. 1, 2**).

A possible explanation for these results could be related to the difference between acute and chronic exposure to a particular insult. Acute exposure to palmitate may trigger a marked response to counteract the ER stress, whereas chronic exposure may eventually overwhelm the cell capacity leading to blunted UPR. Indeed, Rumora et al. [79] and Sajic et al. [84] clearly demonstrated how saturated FFA may differentially affect the nervous system *in vivo* compared to *in vitro*.

An alteration of carbohydrate and lipid metabolism was observed. We found a downregulation of several enzymes implicated on **glycolytic pathway** coinciding with a previous study [72] reporting the reduction of glycolytic metabolites (G6P/F6P; 3PG/2PG; PEP; and lactate) in sciatic and sural nerve of *db/db* mice at 20 weeks of diabetes. In addition, we have found in SCN a decline in aconitase, an enzyme which catalyses the conversion of citrate to isocitrate in the TCA cycle. Concurrently, the ROS-mediated inhibition of aconitase activity has been previously demonstrated [197; 198] as well as its decreased activity in DRG and SCN from *db/db* mice [72]. Interestingly, this study also found that among the TCA cycle metabolites, citrate and isocitrate were significantly lower in DRG,

SCN and sural nerve. Overall, these results may indicate that diabetic PNS exhibit an **energetic deficiency**.

In this regard, lower ATP availability in the PNS of *db/db* mice is also represented by downregulation of ANT1 and creatine kinase M-type (M-CK), in both tissues. In addition, it has been demonstrated that ANT1 is responsible for 50-66% of the basal proton conductance. During oxidative phosphorylation, protons are driven back into the matrix through the ATP synthase following an electrochemical proton gradient to synthesize ATP. However, some protons return to the matrix through alternative leak pathways, causing mild uncoupling and lowering the efficiency [199]. One of these pathways is called basal proton conductance which is constitutive and unregulated. It has been proposed that partial dissipation of  $\Delta p$  by mild uncoupling could protect from oxidative damage by limiting formation of ROS due to decreased mitochondrial membrane potential and decreased local oxygen availability [200]. Since ANT1 content is lower in our data, BPC might be poor and, consequently, superoxide production may increase.

The downregulation of V-ATPase subunit H in DRG and SCN may also be related to the decrease in ATP concentration, compromising protein processing and degradation, endocytosis and vesicular traffic, and synaptic vesicle loading [173]. Interestingly, the downregulation of ANT1 and V-ATPase subunit H in Langerhans islets from type 2 diabetes MKR mice model has been described [201].

Concerning **lipid metabolism**, we found an upregulation in lipid catabolism whereas a decline in lipid biosynthesis, as an effort to increase cellular ATP. Interestingly, the enrichment of genes related

to lipid metabolism has also been described by Pande et al. [164] which hypothesized that it could be associated with increased amounts of adipose tissue in the epineurium of the *db/db* mice. Furthermore, Sas et al. [202] described an increase in metabolic flux towards lipid oxidation in SCN from *db/db* mouse after 20 weeks with diabetes.

In DRG, we found a notable decrease in proteins related to **translational machinery**, especially those that constitute the ribosomal subunits 60S and 40S. This could also be related to ATP depletion or even to insulin resistance [113], which may decrease the insulin mediated protein synthesis [203]. Surprisingly, ribosomal proteins were not altered in SCN.

The upregulation of **muscle-related proteins** in DRG was corroborated by other studies reporting the presence of myosin and troponin in DRG neurons [204; 205], while actin and tropomyosin isoforms, the major components of neuronal microfilaments, were increased in DRG following spinal nerve ligation, suggesting that muscle-type enzymes could be upregulated to uphold functional and structural stability of cells under stress [206]. Overall, it seems that there is an alteration of cell scaffold considering also the upregulation of **cytoskeleton proteins** in both tissues that could be related with injury or inflammation.

**Acute-phase response proteins** increase or decrease in plasma during inflammatory disorders, modulating the inflammatory response [171]. We found both, positive and negative acute-phase proteins differentially expressed in *db/db* PNS.

Haptoglobin is a haemoglobin-binding acute phase protein with an antioxidant function primarily synthesized in the liver. However, Zhao et al. [207] found that it is also expressed in brain in which it plays a defensive role protecting neurons from damage induced by haemolytic products after intracerebral haemorrhage. McMillan [208] examined levels of some acute phase proteins in adult diabetes patients (principally type II) compared with subjects with glucose intolerance and control subjects. In agreement with our results, they found that haptoglobin, orosomucoid 1, and C-reactive protein increased in both diabetes and glucose intolerance, whereas serum albumin level decreased more notably as hyperglycaemia advanced.

Orosomucoid 1 or  $\alpha_1$ -acid glycoprotein (AGP 1) is a member of the lipocalin family that modulates immune and inflammatory responses [175] and it is increased in adipose tissue of *db/db* mice, and in plasma of obese and/or diabetic patients. Increased AGP levels in circulation, mediated by an implanted osmotic pump, were beneficial in *db/db* mice as it improved insulin tolerance with the suppression of proinflammatory and prooxidative profiles in their adipose tissue [178]. Interestingly, *Agp1* mRNA upregulation in DRG from *db/db* mice has also been described [209].

On the other hand, we found overexpression of complement C3, one of the most versatile complements in host defence and inflammation. De Jonge et al. [176] characterised the presence of RNAs coding for complement components in sciatic nerves from patients without peripheral nerve disease and described C3 immunofluorescence in endoneurium and blood vessels. They hypothesized that local biosynthesis of complement components contributes to normal regeneration and remyelination of axons by facilitating the efficient myelin clearance after nerve injury. Moreover, Rosoklija et al. [210]



reported the presence of activated complement proteins in the endoneurial microvessels of sural nerve biopsies from individuals with diabetes. Furthermore, Komori et al. [206] found C3 increase in DRG after spinal nerve ligation.

Hemopexin, which may be involved in oxidative stress protection, was also increased in DRG and SCN of *db/db* mice in this study. In injured peripheral nerves, hemopexin mRNA is expressed by fibroblasts, Schwann cells, and invading macrophages, accumulating in the extracellular matrix of SCN as well as DRG extracellular space [177]. All these data suggest that the higher levels of acute-phase proteins could be a mechanism of protection against excessive inflammation and oxidative damage in DN.

Concomitant with the acute-phase response activation, in our data we also observed the enrichment of **inflammatory markers** such as S100-A8 and S100-A9. S100-A8/9, also called calprotectin, is a stable heterodimer, abundantly expressed in neutrophils and activated macrophages, associated with acute and chronic inflammatory conditions. Calprotectin has a role in activation of NADPH oxidase, toll like receptors 4 (TLR4), and RAGE, which are important signalling pathways in pathogenesis of diabetic complications [133; 211-213]. Moreover, Jin et al. [214] found a strong association between S100-A8 and S100-A9 upregulation in peripheral blood and higher risk to develop diabetic neuropathy in type 1 diabetic patients. In addition, higher levels of immunoglobulin light chain kappa and heavy chain gamma were also detected. Hur et al. [209] found in DRG from *db/db* mice a higher expression at RNA level of Ig  $\gamma$  chain meaning that the upregulation at protein level must be, at least partially, of neuronal origin.

Of note, the most downregulated protein in DRG and the second most downregulated in SCN was **MUP**. Via their central pockets, major urinary proteins bind to volatile pheromones or other lipophilic molecules, and regulate their transportation in the circulation, excretion in the kidney, and release into the air from urine marks [174]. Interestingly, *Mup1* mRNA was reduced by 30-fold in the liver of *db/db* mice and decreased in circulation of both HFD and *db/db* mice [215]. Recombinant MUP1 suppresses the gluconeogenic and lipogenic programs in the liver [216] and promotes mitochondrial biogenesis and oxidative phosphorylation in skeletal muscles, thus increasing energy expenditure and insulin sensitivity [215]. Furthermore, rosiglitazone and resveratrol, that decrease hyperglycaemia and glucose intolerance in diabetic mice, also stimulate *Mup1* expression in the liver [215; 217]. In addition, Kleinert et al. [218] found that *Mup1* is endogenously expressed in mouse skeletal muscle and it markedly decreases with HFD, while increases with exercise training and it improves insulin-stimulated GLUT4 translocation in cultured muscle cells.

Here, we demonstrate that MUP is expressed by both DRG and SCN, and located in the extracellular matrix of PNS. More importantly, its expression inversely correlates with the time of diabetes in DRG and it is a very early event in SCN, which needs further studies. Despite structural similarities with the acute-phase protein AGP1, *in vitro* studies did not show any improvement related to oxidative stress or cell viability.

Nonetheless, preliminary *in vivo* data suggests that downregulation of *Mup* in PNS from wild-type mice might be involved in sensory nerve conduction deficits. This study is currently ongoing to analyse

the evolution of the electrophysiological alterations and elucidate the action mechanism of MUP.

Lipocalin family comprises a set of evolutionary conserved genes present in all kingdoms of life. Mouse genome contains 45 lipocalin-like genes, while human genome 19 genes. Despite most lipocalin-like genes are found in both mice and humans, functional major urinary genes are not present in human genome. Probably, the pseudogenization of the single *MUP* gene found in human genome may have resulted from the inactivation of vomeronasal pheromone receptors, which has also been observed in other primates [219].

Even though MUP function in PNS is still unknown, the expression of MUP mRNA outside the liver and the NCV deficits observed *in vivo* may suggest a new role, non-related to chemical communication. Therefore, it is reasonable to think that other lipocalin-like proteins found in humans may have a similar role in PNS as MUP in mouse. Indeed, some lipocalin proteins have been used as biomarkers in the clinical practice [219].

We did not find many differences between DRG and SCN proteomics, correlating with a previous publication that compared transcriptional network from DRG and SCN in T2DM using microarray analysis, without any relevant difference highlighted between them [220]. Notably, the antioxidant enzymes like GSTM, the sarco/ER Ca<sup>2+</sup> ATPase, and the muscle-related proteins are all increased in DRG but not in SCN, which may indicate a higher adaptability to stress by DRG compared to SCN.

No other proteomic studies have been reported so far for DN in type 2 diabetes. Using microarray technology, Pande et al. [164]

characterised the transcriptional profile of the SCN from *db/db* mice at 24 weeks of age (20 weeks of diabetes). They identified several pathways enriched in diabetic nerves: carbohydrate and lipid metabolism, glutathione metabolism, cell development, cell adhesion and extracellular matrix-receptor interaction, and signal transduction pathways. In addition, in agreement with our results, several markers of oxidative stress were detected. Overall, similar biological annotations were found, but also some discrepancies regarding fold change directionality that may be due in part to methodologic differences. For instance, we used animals with shorter duration of diabetes and lean instead of heterozygous *db/+* mice as controls. Moreover, as previously mentioned, poor correlation between transcriptomics and proteomics has been demonstrated due to differences in transcriptional/ translational control [166].

Despite the aetiology of diabetic neuropathy differs from type 1 to type 2 diabetes, only few studies have compared the molecular alterations exhibited by animal models of the two most common types of diabetes. In 2018, McGregor et al. [221] published a comprehensive analysis of transcriptional signatures conserved in human and murine diabetic peripheral neuropathy. Microarray datasets from murine models of type 1 (streptozotocin-treated, STZ) and type 2 (*db/db* and *ob/ob*) diabetes as well as human patients were analysed. Bioinformatic analysis revealed highly conserved pathways among different models and human samples studied highlighting lipid metabolism, extracellular matrix homeostasis and immune response. Strikingly, comparison between murine models and human samples or between type 1 and 2 diabetes mice demonstrated that while similar molecular pathways are involved in

DN, differences in fold change directionality were observed for many of them.

Nonetheless, other transcriptomic and metabolomic studies in type 1 diabetes drew similar conclusions regarding **metabolic deficiency** in diabetic PNS as type 2 diabetes research. Akude et al. [71] demonstrated lower levels of proteins related to TCA cycle and mitochondrial respiratory chain in DRG sensory neurons from STZ-induced diabetic rats after 22 weeks. Moreover, Rojas et al. [222] detected an evident reduction of some TCA metabolites in sciatic nerve of type 1 diabetic C57 Bl6/j mouse after 22 weeks with diabetes, while at 12 weeks only a trend for reduction was noticed. Therefore, it seems that the long-term outcome in type 1 diabetes models may be a metabolic deficiency as described in type 2 diabetes models by previous bibliography and our own data.

Overall, our proteomic data uncover new pathways altered in diabetic neuropathy and validate previous transcriptomic and metabolomic results confirming that both DRG and SCN present molecular alterations, even before morphometric changes developed. It is worth mentioning that many efforts have been done to develop therapeutic approaches that counteract oxidative stress and inflammation with low or moderate effect in clinical practice. Our results, in conjunction with other publications, point out that low ATP bioavailability due to metabolic impairment could represent the main mechanism of neurodegeneration observed in diabetic neuropathy. These findings may provide important information to select appropriate targets to develop new therapeutic strategies for diabetic neuropathy.

Based on these data, and with the aim to counteract the effect of some of the altered mechanisms in T2DN, we decided to overexpress **KLOTTHO** using AAV vectors in the PNS, as a proof of principle in the *db/db* mouse model. KLOTTHO is able to reduce inflammation, increase bioenergetics by improving mitochondrial function and activate redox systems, preventing oxidative stress [182; 223]. Our *KI* gene therapy showed a trend to ameliorate some of the hallmarks of the disease, such as lower compound muscle action potential amplitude and motor nerve conduction velocity, or reduced number of active sweat glands, but due to the high mortality associated with *db/db* model, our data does not reach statistical significance. Even though pandemic crisis prevented us to repeat this experiment for this thesis, we aim to further analyse KLOTTHO overexpression with larger animal size in the near future.



# ***CONCLUSIONS***





**1-** *Lep<sup>db/db</sup>* mouse develops robust sensory and motor neuropathy, highlighting an important decrease in CNAP amplitude and conduction velocity of sensory fibres from caudal nerves, compared to sciatic nerve, thus, confirming distal-to-proximal degeneration.

**2-** *Lep<sup>db/db</sup>* mouse develops autonomic dysfunction based on the notable hypohidrosis of hindpaws after pilocarpine administration, explained by lower innervation of sweat glands and subsequent gland atrophy.

**3-** *Lep<sup>db/db</sup>* type 2 diabetes model shows progressive weight loss around 13 weeks after diabetes onset, despite sustained hyperglycaemia and dyslipidaemia.

**4-** Proteomic study identified several altered pathways in DRG and SCN from *db/db* mice, highlighting those related to oxidative stress and unfolded protein response, metabolic dysfunction, translation, muscle-type and cytoskeleton proteins, and acute phase and inflammatory responses.

**5-** PNS under type 2 diabetes exhibits metabolic deficiency related to reduced glycolytic pathway and TCA cycle, and lower ATP availability due to downregulation of ANT1 and creatine kinase M-type.

**6-** Proteomic analysis did not detect significant differences between DRG and SCN rather than the upregulation of GSTM enzymes, SERCA Ca<sup>2+</sup> channel, and muscle-like proteins in DRG, and downregulation in SCN.

**7-** Major urinary protein was identified as one of the most downregulated proteins in DRG and SCN from *db/db* mice, whose expression inversely correlates with the time of diabetes in DRG and it is a very early event in SCN.

**8-** MUP protein is located in the extracellular matrix of DRG and SCN.

**9-** MUP protein is not able to counteract oxidative stress in sensory neurons *in vitro*.

**10-** *Mup* silencing *in vivo* using AAVrh10-shRNA might be involved in sensory nerve conduction deficits.

**11-** AAV9-*KI* achieves high levels of *KI* overexpression in DRG and SCN after intrathecal administration.

**12-** AAV9-*KI* shows a trend to ameliorate lower CMAP amplitude and motor nerve conduction velocity, and reduced number of active sweat glands in treated *db/db* mice.

***MATERIALS AND  
METHODS***



## 1. *IN VITRO* CELL CULTURE

### 1.1. CELL LINES

Many cell lines have been used to complete this work. We described below the characteristics and culture conditions for each of them.

#### HEK293

Embryonic kidney cells from human origin.

**Growth media:** DMEM (Dulbecco's Modified Eagle Medium) high glucose (Biowest, Nuaille, France) + 10% FBS (fetal bovine serum, Biowest) + 1% P/S (penicillin-streptomycin, Biowest).

#### NSC-34

Hybridoma cell line resulting from the fusion of mouse embryonal motoneurons with the mouse neuroblastoma N18TG2 [224].

**Growth media:** DMEM high glucose + 10% FBS + 1% P/S

**Differentiation media:** DMEM/F12 (Capricorn Scientific, Ebsdorfergrund, Germany) + 1% MEM non-essential amino acids (Biowest)+ 1% FBS + 0.5% P/S

#### MED17.11

Conditionally immortal DRG cell line generated from the Immortomouse [225].

**Growth media:** 33°C, DMEM/F12 + 10% FBS + 1% P/S + 5 ng/mL IFN $\gamma$  (Merck, Darmstadt, Germany) + 0.5% chicken embryonic extract (Gentaur, Kampenhout, Belgium).

**Differentiation media:** 37°C, DMEM/F12 + 10% FBS + 1% P/S + 10 ng/mL FGF2 (Sigma-Aldrich, St. Louis, MO, US), 0.5 mM dibutyryl-cAMP (Santa Cruz Biotechnology, Dallas, TX, US), 25 µM forskolin (R&D systems, Minneapolis, MN, US) + 5 µg/mL Y-27632 (Chemdea, Ridgewood, NJ, US) + 100 ng/mL beta-NGF (R&D systems) + 10 ng/mL GDNF (Sigma-Aldrich).

### ND7/23

Hybrid cell line derived from neonatal rat dorsal root ganglia neurons fused with the mouse neuroblastoma N18TG2 [226].

**Growth media:** DMEM high glucose + 10% FBS + 1% P/S

**Differentiation media:** DMEM high glucose + 0.5% FBS + 1% P/S + 100 ng/mL NGF 2.5s (Merck).

## 1.2. CELL TRANSFECTION

Production of MUP protein and validation of shRNA against *Mup* was achieved by transfection of HEK293 cell line for 3 hours using as transfection reagents branched polyethyleneimine (PEI, Sigma-Aldrich) or lipofectamine™ 2000 (ThermoFisher, Waltham, MA, US) in low FBS medium. Several plasmids were used in these experiments including: pCAG-*Gfp*, pCAG-*Mup*, pshRNA-*Mup* and pshRNA-Scramble.

## 1.3. OXIDATIVE STRESS ASSAY

Reactive oxygen species production was quantitatively assessed *in vitro* using the DCFDA-Cellular ROS Assay Kit (Abcam, Cambridge, UK) upon exposure to oxidant components (300 µM H<sub>2</sub>O<sub>2</sub> or 250 µM

tBHP, Sigma-Aldrich). DCFDA (2',7' –dichlorofluorescein diacetate) is a fluorogenic dye that diffuses into the cell and measures hydroxyl, peroxy and other reactive oxygen species activity. Briefly, after seeding in 96-well plates, cells were exposed to drugs for two hours in different medium conditions. Then, cells were stained with 25  $\mu$ M DCFDA for 45 minutes and fluorescence was detected at excitation/emission wavelength of 485/535 nm.

#### 1.4. MTT ASSAY

Cell viability upon oxidant insults (300  $\mu$ M H<sub>2</sub>O<sub>2</sub> or 250  $\mu$ M tBHP) was assessed by the MTT (Methylthiazolyldiphenyl-tetrazolium bromide, Sigma-Aldrich) assay. Briefly, after seeding in 96-well plates, cells were exposed to drugs for different time periods (up to 24 hours) and in different medium conditions. Then, cells were incubated for 3 hours at 37°C with 0.5 mg/mL MTT and lysed with lysis buffer (2 mM HCl, 0.05% Tergitol type NP40 (Sigma-Aldrich), isopropanol (Panreac, Castellar del Vallès, Spain)). Viable cells with active metabolism convert MTT into formazan leading to a colorimetric change from yellow to purple. Thus, the measured absorbance at 540 nm was proportional to the number of viable cells.

#### 1.5. PREPARATION OF BSA-CONJUGATED PALMITATE

Low solubility of palmitate in aqueous solution was overcome by the utilisation of bovine serum albumin (BSA) as a carrier and stabilising agent, leading to an aqueous-soluble reagent that can be absorbed by cells. Conjugation protocol from Seahorse Bioscience (Agilent, Santa Clara, CA, US) was followed. Briefly, Ultra Fatty Acid Free BSA (Roche, Merck) was dissolved in 150 mM NaCl (Panreac) and warmed to 37°C, while sodium palmitate (Sigma-Aldrich) in 150 mM



NaCl was stirred and warmed to 70°C until complete dissolution. Then, palmitate was transferred to BSA solution and stirred for 1 hour at 37°C to achieve conjugation (6:1 molar ratio Palmitate:BSA).

To study the effect of palmitate *in vitro*, negative controls BSA and methyl palmitate (non-metabolisable form of palmitate, Sigma-Aldrich) were produced following the same protocol. On the other hand, thapsigargin (Sigma-Aldrich) was used as positive inductor of ER stress.

## 2. CLONING

### 2.1. *Mup* CLONING

Major urinary protein was amplified from sciatic nerve tissue of wt mice using a pair of primers that recognise the multiple transcript variants existing: forward (Fwd), 5'-AAATGAAGATGCTGCTGCTGC-3'; reverse (Rv), 5'-TCATTCTCGGGCCTGGAGG-3'. Amplification was performed by conventional PCR: activation (95°C, 5 min), followed by 30 cycles of 95°C (1 min), 58°C (45 s) and 72°C (1 min), and a final step of 72°C for 10 min. PCR products were run into a 1% agarose gel and purified by Wizard® SV Gel and PCR Clean-Up System (Promega, Madison, WI, US). Once DNA was purified a cloning strategy was designed to clone *Mup* under the control of CAG promoter.

In a nutshell, the general cloning strategy is based on the introduction of a DNA fragment (insert) into a DNA vector to generate a single molecule. For this purpose, donor and receptor DNA are digested using restriction enzymes (New England Biolabs, Ipswich, MA, US) which exhibit specific patterns of DNA digestion. Thus, usage of different restriction enzymes enables to introduce the insert

into the vector in a very precise site. After digestion, receptor DNA is usually dephosphorylated to avoid religation with itself using the FastAP Thermosensitive Alkaline Phosphatase kit (ThermoFisher). Once dephosphorylated, 50 ng of vector and x ng of insert (= 50 ng vector \* base pairs (bp) insert \*3/bp vector) are ligated overnight at 16°C. Then, ligation product is transformed in E.coli TOP10 (ThermoFisher) through heat shock and culture in LB-agar (Condalab, Madrid, Spain) + antibiotic. Finally, individual colonies are selected, grown in LB broth + antibiotic overnight at 37°C and transformed plasmids containing our insert are obtained by DNA maxiprep kit (E.Z.N.A.® FastFilter Plasmid DNA Maxi Kit, Omega Bio-Tek, Norcross, GA, US).

## 2.2. shRNA DESIGN AND CLONING

Design of shRNA against *Mup* gene was done using siRNA Target Finder (GenScript, Piscataway, NJ, US) and siRNA Wizard™ software (InvivoGen, San Diego, CA, US) following the criteria and advice of Viral Vector Production Unit (UPV, UAB, Bellaterra, Spain, <https://www.viralvector.eu/>). Three different shRNA were designed, cloned under H1 promoter, and tested for the highest silencing efficacy. Finally, we selected the following sense sequence for our silencing experiments: 5'- AAGAGTGCTCCGAATTATCTA-3'.

## 3. VIRAL VECTORS PRODUCTION

AAV vectors were produced by triple transfection of HEK293 cells, using branched PEI as transfection reagent, with the following plasmids: 1. **pXX6**, containing the adenoviral genes required for AAV replication. 2. **rep2cap9 or rep2capRh10**, containing the *rep* gene of AAV2 and the *cap* gene of AAV9 or AAVrh10. 3. **Expression**

**cassette**, with the transgene of interest flanked by the ITRs sequences of AAV2.

After 48 hours, cellular pellet and supernatant were separated by centrifugation and several purification steps were performed with both samples. Cellular pellets were lysed by freeze-thaw cycles, debris were eliminated by centrifugation and polyethylene glycol (PEG, Sigma-Aldrich) was added to precipitate AAV. Meanwhile, PEG was also used to favour the precipitation of AAV particles found in the supernatant. Finally, viral particles were purified by ultracentrifugation in an iodixanol gradient.

The titration of final AAV vector was performed using Quant-iT™ PicoGreen® dsDNA assay kit (ThermoFisher) allowing DNA quantification by fluorescence detection [227]. **Table 11** shows the features of the AAV vectors used in this thesis as well as the viral dose administered by intrathecal injection.

**Table 11.** Main characteristics of the AAV vectors used in this thesis.

<b>Vector name</b>	<b>Promoter</b>	<b>Transgene</b>	<b>Regulatory element</b>	<b>Dose (vg/animal)</b>
<b>AAVrh10-Gfp</b>	CAG	<i>Gfp</i>	WPRE	8.68x10 <sup>10</sup>
<b>AAVrh10-shRNA-Mup</b>	H1	shRNA- <i>Mup</i>	-	1.5x10 <sup>11</sup>
<b>AAVrh10-shRNA-Scramble</b>	H1	shRNA-Scramble	-	1.5x10 <sup>11</sup>
<b>AAV9-s-KI</b>	CAG	s-KI	-	1.9x10 <sup>11</sup>
<b>AAV9-mock</b>	CMV	Stuffer DNA	-	1.9x10 <sup>11</sup>

**CAG** is a synthetic promoter with strong and ubiquitous expression in mammalian cells. It was constructed using the cytomegalovirus (**CMV**) early enhancer element, the promoter and the first exon and intron of the chicken  $\beta$ -actin gene, and the splice acceptor of the rabbit  $\beta$ -globin gene [228; 229].

**H1** is a polymerase III promoter used for shRNA transcription [230].

**WPRE** is a post-transcriptional regulatory element placed in cis at 3' of the transgene that enhances its expression [231].

Part of AAV vectors were produced by the UPV (<https://www.viralvector.eu/>).

#### 4. ANIMAL PROCEDURES

Animal care and all experimental procedures were approved by the Biosafety and the Ethical Committees of the Universitat Autònoma de Barcelona.

##### 4.1. MURINE MODELS

Male BKS-*Lep<sup>db/db</sup>* (Envigo, Horst, The Netherlands) and lean littermate (BKS-*Lep<sup>+/+</sup>*) mice were used as a type 2 diabetes model. Also, male or female Hsd:ICR (CD-1®) mice (SE-UAB) were used as wt animals to evaluate AAVrh10 tropism in PNS as well as the effect of MUP silencing on the PNS using an AAVrh10-shRNA. In both cases, mice were fed *ad libitum* with a standard diet (2014 Teklad Global 14% Protein; Envigo) and kept under a light-dark cycle of 12h. For BKS-*db/db*, diabetes was assessed by measuring fasting blood glucose weekly with a Glucometer Contour® XT (Bayer, Leverkusen, Germany). Animals with glycaemia below 250 mg/dL

were not included in further studies. Biochemical parameters were measured by the Veterinary Clinical Facility (UAB).

## 4.2. SURGICAL PROCEDURES

### 4.2.1. ANAESTHESIA AND EUTHANASIA

Different methods of anaesthesia were used depending on the procedure performed. Before perfusion with 4% paraformaldehyde (PFA, Sigma-Aldrich), mice were anaesthetized by intraperitoneal injection of a mix of ketamine (Imalgene, Merial Laboratorios, Tarragona, Spain) and xylazine (Rompun, Bayer) diluted in phosphate-buffered saline (PBS). The dosage used was 100 mg/kg of ketamine and 10 mg/kg of xylazine. For intrathecal administration, isoflurane vaporizer was used. Usually, 4% isoflurane (ISOFLO®, Ecuphar, Barcelona, Spain) was enough to induce a state of general anaesthesia, whereas 2-2.5% was used for maintenance. For electrophysiology, pentobarbital (Sigma-Aldrich) at 50 mg/kg dose was administrated by intraperitoneal injection.

Euthanasia of the mice was performed by different means, depending on subsequent use of mouse samples. Inhalation by ISOFLO® and decapitation was the procedure of choice to obtain fresh tissue samples. Then, organs were dissected, frozen into liquid nitrogen and preserved at -80°C. On the other hand, fixed tissue samples obtained by animal PFA perfusion required ketamine/xylazine anaesthesia. Briefly, the thoracic cavity was exposed, liver was cut, and 20 mL of 4% PFA-PBS was injected to the left cardiac ventricle.

**D-PBS 1x, pH 7.4:** 137 mM NaCl, 3 mM KCl, 10 mM Na<sub>2</sub>HPO<sub>4</sub> · 12 H<sub>2</sub>O, 1.7 mM KH<sub>2</sub>PO<sub>4</sub> (Panreac).

#### 4.2.2. INTRATHECAL ADMINISTRATION

Intrathecal injection enables to efficiently administrate viral vectors to CSF achieving widespread distribution along central and peripheral nervous system (**Fig. 57**).

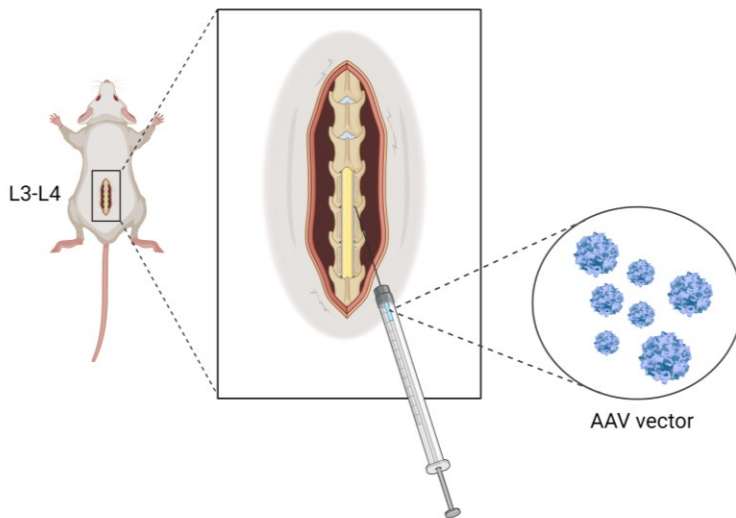


**Figure 57.** Schematic representation of intrathecal administration of viral vectors between L3-L4 vertebrae.

Under isoflurane anaesthesia, mouse reflexes were checked, lumbar region was shaved and the skin was cut to visualise the lumbar vertebral column. Under binocular loupe, the left epaxial muscles at L3 and L4 region were separated from vertebrae, cutting the fascia. Muscle dissection should allow to visualise the intervertebral foramen between L3 and L4, which is situated between the joints formed by the articular process of L3 and the transverse process of L4.

Ten to twenty  $\mu\text{L}$  of AAV vector were slowly delivered using a Hamilton syringe with a 3 cm long 33 Gauge needle (Sigma-Aldrich). The needle was placed longitudinal to the spine, with the tip directed

to the cranial part, and was carefully introduced into the foramen around 4-5 mm. The proper position of the needle allowed the piercing of the outer meninges (dura mater and arachnoid), which was confirmed by a tail flick reflex in most of the cases. The needle was removed 15 seconds after finishing vector delivery to favour spread through the CSF and avoid reflux to periphery.

The epaxial muscles were sutured using absorbable suture (Safil®, B.Braun, Rubí, Spain) and the skin was closed using Michel suture clips (Fine Science Tools, Heidelberg, Germany). Each mouse was monitored until they completely recovered from anaesthesia.

#### 4.3. FUNCTIONAL EVALUATION

##### 4.3.1. ELECTROPHYSIOLOGICAL TESTING

Nerve conduction tests were performed after 12, 17, 21 and 25 weeks of diabetes in collaboration with Dr. Xavier Navarro. Under anaesthesia with pentobarbital, the sciatic nerve was stimulated percutaneously through a pair of needle electrodes placed first at the sciatic notch and then at the ankle, delivering pulses of 0.05 ms up to 25% above the intensity that gave a maximal response. The compound muscle action potential was recorded from the third interosseus plantar muscle with microneedle electrodes. Similarly, the sensory compound nerve action potential was recorded by electrodes placed at the fourth toe near the digital nerves. CMAP and CNAP represent the summation of the action potentials of all the excited muscle fibres and sensory nerve fibres, respectively [232]. Evoked action potentials were amplified and displayed on a storage oscilloscope (Tektronix 420, Berkshire, UK). The nerve conduction velocity was calculated for each segment tested: MNCV for the

sciatic notch-ankle segment and SNCVd for the distal segment ankle-digit. In addition, CNAP from caudal nerves was also evaluated by stimulating at a distal site and recording with microneedles placed at the base of the tail. Also, tail sensory NCV was calculated for a 35 mm segment from the tail. During electrophysiological tests, the animals were placed over a warm flat steamer controlled by a hot water circulating pump, and the hind-paw skin temperature was maintained above 32°C [233].

#### 4.3.2. SWEATING TEST

Mice were immobilized in a plastic tube and sweating was stimulated by subcutaneous injection of pilocarpine nitrate (5 mg/kg, Sigma-Aldrich) into the back of the mice. This dose of pilocarpine induces a maximal and stable sweating response [234]. Sudomotor function was evaluated using the silicone imprint technique at 10 minutes after pilocarpine administration in collaboration with Dr. Jorge Vilches [235]. We determined the number of active sweat glands and the estimated sweat output per secreting gland by making an impression silicone mould of the plantar surface of the hindpaw (Silasoft Normal, Detax GmbH & Co., Etllingen, Germany). A mixture of 0.2 ml base material plus five drops of hardener from a 23-gauge needle was gently spread with a spatula over the sole. As the silicone hardened (3–5 min), it retained the impressions of sweat droplets as they emerged from the sweat ducts and pushed up into the mould. Droplet impressions were counted under a dissecting microscope (X20) using transmitted light. Total counts of sweat glands were made for each paw and for defined subdivisions of the paw [168; 235]. The diameter of each sweat impression in the third toe flat area was measured with a micrometer grid and used to



calculate the volume of sweat droplets (sweat output) considered to approximate a sphere (volume =  $(4/3) \pi r^3$ ) [236].

## 5. HISTOLOGICAL ANALYSIS

### 5.1. MORPHOMETRY OF TIBIAL NERVE

Tibial nerve segments taken above the ankle were fixed in glutaraldehyde (Sigma-Aldrich)-paraformaldehyde (3%:3%) in cacodylate buffer (0.1 M, pH 7.4) (Sigma-Aldrich) for 4–6h at 4°C. Then, in collaboration with Dr. Jesús Ruberte, tibial nerves were post-fixed with 1% OsO<sub>4</sub> (Sigma-Aldrich) + 0.8% FeCNK (Sigma-Aldrich) in saline phosphate buffer (0.1 M, pH 7.4), washed in distilled water, dehydrated with graded series of acetone, and embedded in SPURR resin (Sigma-Aldrich). Light microscopy images were acquired on 0.7 µm semithin sections stained with toluidine blue, under a Nikon ECLIPSE 80i microscope. Morphometrical evaluation, including nerve cross-sectional area, axonal counts, and myelinated axon and fibre perimeters and diameters, was made from images obtained using a Nikon Camera DXM1200F. Three to four fields, covering 200-300 myelinated fibres, were randomly selected for morphometrical analyses using ImageJ and ObjectJ plugin [233].

**Phosphate buffer (0.1 M, pH 7.4):** Prepared by equilibration of NaH<sub>2</sub>PO<sub>4</sub> and Na<sub>2</sub>HPO<sub>4</sub> (Panreac).

## 5.2. IMMUNOHISTOCHEMISTRY

### 5.2.1. DRG AND SCN

Anesthetized animals were perfused with 4% PFA-PBS buffer. DRG and sciatic nerves were cryoprotected with 30% sucrose and embedded in Tissue-Tek OCT compound (Sakura, Alphen aan den Rijn, The Netherlands). Ten  $\mu\text{m}$  thick sections of DRG and sciatic nerves were permeabilised with methanol (Panreac) and washed with TRIS 0.05M (Trizma® base, Sigma-Aldrich) + 0.3% Triton X-100 (Sigma-Aldrich) + 3% BSA (Sigma-Aldrich) + 5% FBS for 1h for tissue blocking. Then, tissue sections were incubated in primary antibodies overnight at 4°C and secondary antibodies for 1h (**Table 12**). Finally, samples were counterstained with Hoechst (Sigma-Aldrich) and mounted in Fluoromount™ Aqueous Mounting Medium (Sigma-Aldrich). Fluorescence signal was detected with a laser confocal microscope ZEISS LSM 700.

### 5.2.2. CUTANEOUS INNERVATION

Plantar pads D and C from euthanized mice were harvested, overnight fixed in 4% PBS-PFA and cryoprotected in 30% PBS-Sucrose (Sigma-Aldrich) for 48h. Fifty  $\mu\text{m}$  thick cryotome pad sections were washed free-floating in PBS with 0.3% Triton-X100 and 1.5% normal donkey serum (Sigma-Aldrich) for 1h, then incubated in primary rabbit antibody against PGP9.5. After washes, sections were incubated in secondary donkey antibody anti-rabbit labelled with Cy3 (**Table 12**). Once placed on a slide, footpad sections were dehydrated by immersing the slides through the following solutions: ethanol 50° 10', 70°C 10', 96°C 10' and 100° 10'. Cytoseal 60 (ProSciTech, Kirwan, Australia) was used as a mounting

medium. Intraepidermal nerve fibres were counted at the lateral side of the footpad as they crossed the basement membrane and expressed as number of fibres/mm length of the epidermis. Representative images from footpads were taken with a Nikon DXM1200F camera mounted on the Nikon Eclipse 90i microscope. To analyse sweat gland area and the percentage of immunoreactive sweat gland area, three sections from each sample were taken and analysed with ImageJ software. The perimeter of each individual sweat gland was defined for each image, and total acinar area as well as individual sweat gland area was automatically measured (in  $\mu\text{m}^2$ ) after background subtraction [237; 238].

**Table 12.** List of antibodies used for immunohistochemistry.

<b>Antibody</b>	<b>Host</b>	<b>Dilution</b>	<b>Source</b>
<b>Glutamine synthetase (G2781)</b>	Rabbit	1/500	Sigma-Aldrich
<b>MUP (sc-166429)</b>	Mouse	1/200	Santa Cruz Biotechnology
<b>P0 (ab31851)</b>	Rabbit	1/200	Abcam
<b>Collagen type IV (AB756P)</b>	Rabbit	1/80	Merck
<b>PGP9.5 (CL7756AP)</b>	Rabbit	1/500	Cedarlane, Southern Ontario, Canada
<b>S100 (Z0311)</b>	Rabbit	1/500	Dako (Agilent)
<b>Cy3-conjugated anti-rabbit (711-165-152)</b>	Donkey	1/800	Jackson ImmunoResearch, Philadelphia, PA, US
<b>Alexa Fluor 568 anti-mouse(A11004)</b>	Goat	1/200	ThermoFisher
<b>Alexa Fluor 488 anti-rabbit (A21206)</b>	Donkey	1/200	ThermoFisher

## 6. MOLECULAR TECHNIQUES

### 6.1. TMT-LC/MS/MS AND BIOINFORMATICS ANALYSIS

Proteomic study was performed independently with DRG and SCN at 15 weeks of diabetes by CSIC/UAB Proteomics Facility. Six pools were prepared using two samples in each pool, thus obtaining three pools for each condition (*Lepr<sup>db/db</sup>* and *Lepr<sup>+/+</sup>*). Eighty µg of protein in RIPA buffer was digested by FASP (filter aided sample preparation) method using 200mM triethylammonium bicarbonate buffer (Sigma-Aldrich) [239]. Each digested pool was labelled using different TMTsixplex™ reagents (ThermoFisher). Amine-reactive TMT™ Isobaric Mass Tagging reagents enable multiplex quantitation of proteins using tandem mass spectrometry. Sample fractionation using a SCX ion-exchange column was performed to reduce sample complexity. Samples were injected using a C18 HPLC column and an analytic column connected on-line to the high-resolution mass spectrometer LTQ-Orbitrap XL (ThermoFisher). Peptide identification was performed using the Proteome Discoverer v1.4 software (ThermoFisher) under 1% false discovery rate (FDR) criterion and using Uniprot 2017-10 database from *Mus musculus*. Protein quantification was done based on the intensity of reporter ions labelled with TMT and considering only the unique peptides. Characterisation of protein localization was done using WebGestalt platform [240], whereas functional enrichment analysis was performed by DAVID bioinformatics resources 6.8 [169]. Functional data was validated with String v11.0 [241] and GeneRanker (Genomatix, Munich, Germany) software.

## 6.2. REAL-TIME PCR

Lumbar DRG and SCN were homogenized separately with Tissue Lyser LT at 50 Hz using QIAzol (Qiagen, Hilden, Germany) to obtain total RNA. Messenger RNA was retrotranscribed using iScript™ cDNA Synthesis Kit, and the analysis of expression was performed by CFX96 Touch™ or CFX384 Touch™ Real-Time PCR Detection System with SYBR® Green Master Mix (Bio-Rad, Hercules, CA, US) and specific primers (ThermoFisher) (**Table 13**). Amplifications were as follows: heat activation (95°C, 3 min), followed by 39 cycles of 95°C (10 s) and 58°C (30 s). Fluorescence detection was performed at the end of the PCR extension, and PCR products were verified for a single amplification using melting curve analysis. Quantification relative to *Rplp0* and *Ywhaz* as housekeeping genes was calculated using the Pfaffl method [242].

**Table 13.** List of primers used for Real-Time PCR.

Gene	Fwd primer (5'- 3')	Rv primer (5'- 3')
<i>Rplp0</i>	ATGGGTACAAGCGCGT CCTG	AGCCGCAAATGCAGATGG ATC
<i>Ywhaz</i>	ACAAAGACAGCACGCT AATAATGC	TTGGAAGGCCGGTTAATT TTC
<i>Mup</i>	TATCCAATGCCAATCGC TGC	TGGTGGAGTCCTGGTGAG AA
<i>Nfe2l2</i>	TGGAATTGGAGTTGCC ACC	GCTCATAGTCCTTCTGTC GC
<i>Hmox1</i>	GAATCGAGCAGAACCA GCCTG	CTCAGCATTCTCGGCTT GGA
<i>Sod2</i>	AGGAGCAAGGTCGCTT ACAG	TGCTCCCACACGTCAATC C
<i>Cat</i>	AGAATTTCACTGACGTC CACCC	TCCCTTCGCAGCCATGTG AG
<i>Hspa5 (M)</i>	GGTATTGAAACTGTGG GAGGAGT	GGTCGTTACCTTCATAG ACCTT
<i>Hspa5 (R)</i>	GGTATTGAAACTGTGG GAGGTGT	GGTCGTTACCTTCGTA GACCTT
<i>Ddit3 (M)</i>	GAGCTGGAAGCCTGGT ATGA	CGCAGGGTCAAGAGTAG TGAA

<b><i>Ddit3</i> (R)</b>	GCAGGAGGTCCTGTCC TCAGAT	GAGGGCTTTGGGAGGTG CT
<b><i>s-KL</i></b>	TCATAATGGAAACCTTA AAAGCAA	CACTGGGTTTTGTCAAAG GA

### 6.3. *Xbp1* ALTERNATIVE SPLICING

*Xbp1* mRNA alternative splicing was assessed by conventional PCR with the following settings: heat activation (95°C, 5 min), followed by 30 cycles of 95°C (1 min), 62°C (30 s) and 72°C (30 s), and a final step of 72°C for 10 min. Primers used enabled the amplification of both transcript variants, unspliced *Xbp1* (*uXbp1*, 330 bp) and spliced *Xbp1* (*sXbp1*, 304 bp): Fwd, 5'-TGAGAACCAGGAGTTAAGA ACACGC-3'; Rv, 5'-TTCTGGGTAGACCTCTGGGAGTTCC-3'. PCR products were run into a 7% acrylamide gel for 3 hours and gel was finally stained with RedSafe™ (iNtRON, Burlington, MA, US).

### 6.4. WESTERN BLOT

Contralateral DRG and SCN were sonicated and homogenized in RIPA lysis buffer with Tergitol type NP-40 and Protease Inhibitor Cocktail (Merck). Protein concentration was determined by Pierce™ BCA Assay (ThermoFisher). After dilution in loading buffer and denaturing for 10 min at 95°C, ten to twenty µg were separated on 10-12% sodium dodecyl sulfate (SDS)-polyacrylamide gel electrophoresis, transferred to Amersham™ Hybond™ P 0.45 PVDF (polyvinylidene fluoride) blotting membrane (GE Healthcare, Chicago, IL, US) using a semidry electrotransfer system (Trans-Blot® Turbo™, Bio-Rad) and immunoblotted with primary and secondary antibodies (**Table 14**) after blocking with tris-buffered saline + tween-20 (TBS-T) + 5% BSA. Immunoreactive proteins were detected by ETA C Ultra 2.0 ECL (Cyanagen, Bologna, Italy) and the

ChemiDoc MP Imaging System (Bio-Rad). Protein bands were quantified by densitometry using ImageJ and the results were normalized by ACTIN or  $\beta$ -TUBULIN III as housekeeping proteins.

**RIPA lysis buffer:** 50 mM Tris-HCl pH 7.4, 150 mM NaCl, 1 mM EDTA (Affymetrix, Santa Clara, CA, USA), 1% Tergitol type NP-40, 0.25% sodium deoxycholate (Sigma-Aldrich), 50 mM sodium fluoride (Sigma-Aldrich), 1 mM sodium ortovanadate (Sigma-Aldrich), 10 mM  $\beta$ -glycerophosphate disodium salt hydrate (Sigma-Aldrich), 5 mM sodium pyrophosphate decahydrate (Sigma-Aldrich) and a protease inhibitor cocktail.

**6x Loading buffer:** 0.35 M Tris-HCl pH 6.8, 3.3% glycerol (Sigma-Aldrich), 10% SDS (Affymetrix), 0.015% bromophenol blue (Sigma-Aldrich), 0.6M DL-dithiothreitol (Sigma-Aldrich).

**Stacking gel:** 3.9% Acryl/Bis 29:1 40% w/v solution (VWR, Radnor, PA, Canada), 0.5 M Tris-HCl pH 6.8, 0.4% SDS. Gel polymerization: 25  $\mu$ L ammonium persulfate (VWR) and 5  $\mu$ L of TEMED (Sigma-Aldrich).

**Resolving gel:** 10-12% Acryl/Bis 29:1, 1.5 M Tris-HCl pH 8.8, 0.4% SDS. Gel polymerization: 60  $\mu$ L ammonium persulfate and 12  $\mu$ L of TEMED.

**Electrophoresis buffer:** 25 mM Tris, 192 mM Glycine (Sigma-Aldrich), 1% SDS.

**Transfer buffer:** 25 mM Tris, 192 mM Glycine, 20% methanol.

**TBS-T:** 50 mM Tris, 136 mM NaCl, 40 mM KCl, 0.1% Tween-20 (Sigma-Aldrich), pH 7.4.

**Table 14.** List of antibodies used for western blot.

<b>Antibody</b>	<b>Host</b>	<b>Dilution</b>	<b>Source</b>
<b>ATP6V1H (GTX110778)</b>	Rabbit	1/1000	Genetex, Alton Pkwy Irvine, CA, US
<b>GSTM5 (GTX108776)</b>	Rabbit	1/5000	Genetex
<b>HO-1 (ab13243)</b>	Rabbit	1/1000	Abcam
<b>MUP (sc-166429)</b>	Mouse	1/500	Santa Cruz Biotechnology
<b>C3 (sc-28294)</b>	Mouse	1/1000	Santa Cruz Biotechnology
<b>Actin (A-2066)</b>	Rabbit	1/5000	Sigma-Aldrich
<b>Tubulin <math>\beta</math>3 (Tuj) (T2200)</b>	Rabbit	1/1000	Sigma-Aldrich
<b>*HRP-coupled anti-rabbit (P0399)</b>	Swine	1/10000	Dako (Agilent)
<b>HRP-coupled anti-mouse (31430)</b>	Goat	1/10000	ThermoFisher

\* *Horseradish peroxidase*

## 7. STATISTICAL ANALYSIS

Data, expressed as mean  $\pm$  SEM, were analysed using Student's T test, one-way ANOVA followed by Tukey's post hoc test or two-way ANOVA followed by Bonferroni's post hoc test. For proteomic analysis, differentially expressed proteins were determined using DanteR software [243] performing one-way ANOVA test followed by Benjamini & Hochberg correction to control the FDR. Differences were considered significant when  $p < 0.05$ .





## ***REFERENCES***



- [1] Mavroudis, A.D., 2018. Diabetes Mellitus in ancient Greek medical writings Aretaeus of Cappadocia, "On the Causes and Symptoms of Acute and Chronic Diseases 2.2". *Hellenic Diabetological Chronicles*, pp. 63-65.
- [2] Eknayan, G., Nagy, J., 2005. A history of diabetes mellitus or how a disease of the kidneys evolved into a kidney disease. *Adv Chronic Kidney Dis* 12(2):223-229.
- [3] 2019. *IDF Diabetes Atlas, 9th edition. International Diabetes Federation*.
- [4] 2019. *Classification of diabetes mellitus*. Geneva: World Health Organization.
- [5] Zheng, Y., Ley, S.H., Hu, F.B., 2018. Global aetiology and epidemiology of type 2 diabetes mellitus and its complications. *Nat Rev Endocrinol* 14(2):88-98.
- [6] Langenberg, C., Lotta, L.A., 2018. Genomic insights into the causes of type 2 diabetes. *Lancet* 391(10138):2463-2474.
- [7] Mahajan, A., Taliun, D., Thurner, M., Robertson, N.R., Torres, J.M., Rayner, N.W., et al., 2018. Fine-mapping type 2 diabetes loci to single-variant resolution using high-density imputation and islet-specific epigenome maps. *Nat Genet* 50(11):1505-1513.
- [8] Ramlo-Halsted, B.A., Edelman, S.V., 1999. The natural history of type 2 diabetes. Implications for clinical practice. *Prim Care* 26(4):771-789.
- [9] Wang, Q.A., Tao, C., Gupta, R.K., Scherer, P.E., 2013. Tracking adipogenesis during white adipose tissue development, expansion and regeneration. *Nat Med* 19(10):1338-1344.
- [10] Ghaben, A.L., Scherer, P.E., 2019. Adipogenesis and metabolic health. *Nat Rev Mol Cell Biol* 20(4):242-258.

- [11] Taylor, R., Holman, R.R., 2015. Normal weight individuals who develop type 2 diabetes: the personal fat threshold. *Clin Sci (Lond)* 128(7):405-410.
- [12] Cotillard, A., Poitou, C., Torcivia, A., Bouillot, J.L., Dietrich, A., Klöting, N., et al., 2014. Adipocyte size threshold matters: link with risk of type 2 diabetes and improved insulin resistance after gastric bypass. *J Clin Endocrinol Metab* 99(8):E1466-1470.
- [13] Lönn, M., Mehlig, K., Bengtsson, C., Lissner, L., 2010. Adipocyte size predicts incidence of type 2 diabetes in women. *FASEB J* 24(1):326-331.
- [14] Weyer, C., Foley, J.E., Bogardus, C., Tataranni, P.A., Pratley, R.E., 2000. Enlarged subcutaneous abdominal adipocyte size, but not obesity itself, predicts type II diabetes independent of insulin resistance. *Diabetologia* 43(12):1498-1506.
- [15] Landgraf, K., Rockstroh, D., Wagner, I.V., Weise, S., Tauscher, R., Schwartz, J.T., et al., 2015. Evidence of early alterations in adipose tissue biology and function and its association with obesity-related inflammation and insulin resistance in children. *Diabetes* 64(4):1249-1261.
- [16] Petersen, M.C., Shulman, G.I., 2018. Mechanisms of Insulin Action and Insulin Resistance. *Physiol Rev* 98(4):2133-2223.
- [17] Wysham, C., Shubrook, J., 2020. Beta-cell failure in type 2 diabetes: mechanisms, markers, and clinical implications. *Postgrad Med* 132(8):676-686.
- [18] Araki, E., Oyadomari, S., Mori, M., 2003. Endoplasmic reticulum stress and diabetes mellitus. *Intern Med* 42(1):7-14.
- [19] Ihara, Y., Toyokuni, S., Uchida, K., Odaka, H., Tanaka, T., Ikeda, H., et al., 1999. Hyperglycemia causes oxidative stress in pancreatic beta-cells of GK rats, a model of type 2 diabetes. *Diabetes* 48(4):927-932.

- [20] Maedler, K., Spinas, G.A., Dyntar, D., Moritz, W., Kaiser, N., Donath, M.Y., 2001. Distinct effects of saturated and monounsaturated fatty acids on beta-cell turnover and function. *Diabetes* 50(1):69-76.
- [21] 2017. Recommendations For Managing Type 2 Diabetes In Primary Care. International Diabetes Federation.
- [22] Forbes, J.M., Cooper, M.E., 2013. Mechanisms of diabetic complications. *Physiol Rev* 93(1):137-188.
- [23] Bican, O., Minagar, A., Pruitt, A.A., 2013. The spinal cord: a review of functional neuroanatomy. *Neurol Clin* 31(1):1-18.
- [24] Davis, M.C., Griessenauer, C.J., Bosmia, A.N., Tubbs, R.S., Shoja, M.M., 2014. The naming of the cranial nerves: a historical review. *Clin Anat* 27(1):14-19.
- [25] Goldstein, B., 2001. Anatomy of the peripheral nervous system. *Phys Med Rehabil Clin N Am* 12(2):207-236.
- [26] Sanvictores, T., Tadi, P., 2021. Neuroanatomy, Autonomic Nervous System Visceral Afferent Fibers and Pain. StatPearls Publishing, Treasure Island (FL).
- [27] Haberberger, R.V., Barry, C., Dominguez, N., Matusica, D., 2019. Human Dorsal Root Ganglia. *Front Cell Neurosci* 13:271.
- [28] Hanani, M., 2005. Satellite glial cells in sensory ganglia: from form to function. *Brain Res Brain Res Rev* 48(3):457-476.
- [29] Hanani, M., Spray, D.C., 2020. Emerging importance of satellite glia in nervous system function and dysfunction. *Nat Rev Neurosci* 21(9):485-498.
- [30] Dyck, P.J., Thomas, P.K., editors, 2005. Peripheral neuropathy. 4th ed.
- [31] Brosius Lutz, A., Chung, W.S., Sloan, S.A., Carson, G.A., Zhou, L., Lovelett, E., et al., 2017. Schwann cells use TAM receptor-mediated phagocytosis in addition to autophagy to clear myelin in a

mouse model of nerve injury. *Proc Natl Acad Sci U S A* 114(38):E8072-E8080.

[32] De Hert, S., De Baerdemaeker, L., De Maeseneer, M., 2014. What the phlebologist should know about local anesthetics. *Phlebology* 29(7):428-441.

[33] Hu, Y., Converse, C., Lyons, M.C., Hsu, W.H., 2018. Neural control of sweat secretion: a review. *Br J Dermatol* 178(6):1246-1256.

[34] Wilke, K., Martin, A., Terstegen, L., Biel, S.S., 2009. Neurobiology of Skin Appendages: Eccrine, Apocrine, and Apoeccrine Sweat Glands. In: Granstein, R.D., Luger, T.A., editors. *Neuroimmunology of the Skin*.

[35] Hodge, B.D., Sanvictores, T., Brodell, R.T., 2021. *Anatomy, Skin Sweat Glands*. StatPearls Publishing, Treasure Island (FL).

[36] Lindsay, S.L., Holmes, S., Corbett, A.D., Harker, M., Bovell, D.L., 2008. Innervation and receptor profiles of the human apocrine (epitrichial) sweat gland: routes for intervention in bromhidrosis. *Br J Dermatol* 159(3):653-660.

[37] Kerassidis, S., 1994. Is palmar and plantar sweating thermoregulatory? *Acta Physiol Scand* 152(3):259-263.

[38] Sato, K., Kang, W.H., Saga, K., Sato, K.T., 1989. Biology of sweat glands and their disorders. II. Disorders of sweat gland function. *J Am Acad Dermatol* 20(5 Pt 1):713-726.

[39] Dyck, P.J., Sherman, W.R., Hallcher, L.M., Service, F.J., O'Brien, P.C., Grina, L.A., et al., 1980. Human diabetic endoneurial sorbitol, fructose, and myo-inositol related to sural nerve morphometry. *Ann Neurol* 8(6):590-596.

[40] Valls-Canals, J., Povedano, M., Montero, J., Pradas, J., 2002. Diabetic polyneuropathy. Axonal or demyelinating? *Electromyogr Clin Neurophysiol* 42(1):3-6.

- [41] Malik, R.A., Tesfaye, S., Newrick, P.G., Walker, D., Rajbhandari, S.M., Siddique, I., et al., 2005. Sural nerve pathology in diabetic patients with minimal but progressive neuropathy. *Diabetologia* 48(3):578-585.
- [42] Said, G., Slama, G., Selva, J., 1983. Progressive centripetal degeneration of axons in small fibre diabetic polyneuropathy. *Brain* 106 ( Pt 4):791-807.
- [43] Sveen, K.A., Karimé, B., Jørum, E., Mellgren, S.I., Fagerland, M.W., Monnier, V.M., et al., 2013. Small- and large-fiber neuropathy after 40 years of type 1 diabetes: associations with glycemic control and advanced protein glycation: the Oslo Study. *Diabetes Care* 36(11):3712-3717.
- [44] Dyck, P.J., Lais, A., Karnes, J.L., O'Brien, P., Rizza, R., 1986. Fiber loss is primary and multifocal in sural nerves in diabetic polyneuropathy. *Ann Neurol* 19(5):425-439.
- [45] Llewelyn, J.G., Gilbey, S.G., Thomas, P.K., King, R.H., Muddle, J.R., Watkins, P.J., 1991. Sural nerve morphometry in diabetic autonomic and painful sensory neuropathy. A clinicopathological study. *Brain* 114 ( Pt 2):867-892.
- [46] Pascoe, M.K., Low, P.A., Windebank, A.J., Litchy, W.J., 1997. Subacute diabetic proximal neuropathy. *Mayo Clin Proc* 72(12):1123-1132.
- [47] Kennedy, W.R., Navarro, X., 1989. Sympathetic sudomotor function in diabetic neuropathy. *Arch Neurol* 46(11):1182-1186.
- [48] Freeman, R., 2014. Diabetic autonomic neuropathy. *Handb Clin Neurol* 126:63-79.
- [49] Pop-Busui, R., Boulton, A.J., Feldman, E.L., Bril, V., Freeman, R., Malik, R.A., et al., 2017. Diabetic Neuropathy: A Position Statement by the American Diabetes Association. *Diabetes Care* 40(1):136-154.



- [50] Giannini, C., Dyck, P.J., 1995. Basement membrane reduplication and pericyte degeneration precede development of diabetic polyneuropathy and are associated with its severity. *Ann Neurol* 37(4):498-504.
- [51] Tuck, R.R., Schmelzer, J.D., Low, P.A., 1984. Endoneurial blood flow and oxygen tension in the sciatic nerves of rats with experimental diabetic neuropathy. *Brain* 107 ( Pt 3):935-950.
- [52] Magnani, P., Cherian, P.V., Gould, G.W., Greene, D.A., Sima, A.A., Brosius, F.C., 1996. Glucose transporters in rat peripheral nerve: paranodal expression of GLUT1 and GLUT3. *Metabolism* 45(12):1466-1473.
- [53] Brownlee, M., 2001. Biochemistry and molecular cell biology of diabetic complications. *Nature* 414(6865):813-820.
- [54] Pisoschi, A.M., Pop, A., 2015. The role of antioxidants in the chemistry of oxidative stress: A review. *Eur J Med Chem* 97:55-74.
- [55] Snezhkina, A.V., Kudryavtseva, A.V., Kardymon, O.L., Savvateeva, M.V., Melnikova, N.V., Krasnov, G.S., et al., 2019. ROS Generation and Antioxidant Defense Systems in Normal and Malignant Cells. *Oxid Med Cell Longev* 2019:6175804.
- [56] Jiang, Y., Calcutt, N.A., Ramos, K.M., Rames, K.M., Mizisin, A.P., 2006. Novel sites of aldose reductase immunolocalization in normal and streptozotocin-diabetic rats. *J Peripher Nerv Syst* 11(4):274-285.
- [57] Nowotny, K., Jung, T., Höhn, A., Weber, D., Grune, T., 2015. Advanced glycation end products and oxidative stress in type 2 diabetes mellitus. *Biomolecules* 5(1):194-222.
- [58] Vlassara, H., Brownlee, M., Cerami, A., 1983. Excessive nonenzymatic glycosylation of peripheral and central nervous system myelin components in diabetic rats. *Diabetes* 32(7):670-674.

- [59] Ryle, C., Leow, C.K., Donaghy, M., 1997. Nonenzymatic glycation of peripheral and central nervous system proteins in experimental diabetes mellitus. *Muscle Nerve* 20(5):577-584.
- [60] Duran-Jimenez, B., Dobler, D., Moffatt, S., Rabbani, N., Streuli, C.H., Thornalley, P.J., et al., 2009. Advanced glycation end products in extracellular matrix proteins contribute to the failure of sensory nerve regeneration in diabetes. *Diabetes* 58(12):2893-2903.
- [61] Vincent, A.M., Perrone, L., Sullivan, K.A., Backus, C., Sastry, A.M., Lastoskie, C., et al., 2007. Receptor for advanced glycation end products activation injures primary sensory neurons via oxidative stress. *Endocrinology* 148(2):548-558.
- [62] Muronetz, V.I., Melnikova, A.K., Barinova, K.V., Schmalhausen, E.V., 2019. Inhibitors of Glyceraldehyde 3-Phosphate Dehydrogenase and Unexpected Effects of Its Reduced Activity. *Biochemistry (Mosc)* 84(11):1268-1279.
- [63] Du, X.L., Edelstein, D., Rossetti, L., Fantus, I.G., Goldberg, H., Ziyadeh, F., et al., 2000. Hyperglycemia-induced mitochondrial superoxide overproduction activates the hexosamine pathway and induces plasminogen activator inhibitor-1 expression by increasing Sp1 glycosylation. *Proc Natl Acad Sci U S A* 97(22):12222-12226.
- [64] Mizukami, H., Osonoi, S., Takaku, S., Yamagishi, S.I., Ogasawara, S., Sango, K., et al., 2020. Role of glucosamine in development of diabetic neuropathy independent of the aldose reductase pathway. *Brain Commun* 2(2):fcaa168.
- [65] Zherebitskaya, E., Akude, E., Smith, D.R., Fernyhough, P., 2009. Development of selective axonopathy in adult sensory neurons isolated from diabetic rats: role of glucose-induced oxidative stress. *Diabetes* 58(6):1356-1364.

- [66] Guéraud, F., Atalay, M., Bresgen, N., Cipak, A., Eckl, P.M., Huc, L., et al., 2010. Chemistry and biochemistry of lipid peroxidation products. *Free Radic Res* 44(10):1098-1124.
- [67] Suzuki, T., Kamiya, H., 2017. Mutations induced by 8-hydroxyguanine (8-oxo-7,8-dihydroguanine), a representative oxidized base, in mammalian cells. *Genes Environ* 39:2.
- [68] Berlett, B.S., Stadtman, E.R., 1997. Protein oxidation in aging, disease, and oxidative stress. *J Biol Chem* 272(33):20313-20316.
- [69] Chowdhury, S.K., Zherebitskaya, E., Smith, D.R., Akude, E., Chattopadhyay, S., Jolival, C.G., et al., 2010. Mitochondrial respiratory chain dysfunction in dorsal root ganglia of streptozotocin-induced diabetic rats and its correction by insulin treatment. *Diabetes* 59(4):1082-1091.
- [70] Ma, J., Farmer, K.L., Pan, P., Urban, M.J., Zhao, H., Blagg, B.S., et al., 2014. Heat shock protein 70 is necessary to improve mitochondrial bioenergetics and reverse diabetic sensory neuropathy following KU-32 therapy. *J Pharmacol Exp Ther* 348(2):281-292.
- [71] Akude, E., Zherebitskaya, E., Chowdhury, S.K., Smith, D.R., Dobrowsky, R.T., Fernyhough, P., 2011. Diminished superoxide generation is associated with respiratory chain dysfunction and changes in the mitochondrial proteome of sensory neurons from diabetic rats. *Diabetes* 60(1):288-297.
- [72] Hinder, L.M., Vivekanandan-Giri, A., McLean, L.L., Pennathur, S., Feldman, E.L., 2013. Decreased glycolytic and tricarboxylic acid cycle intermediates coincide with peripheral nervous system oxidative stress in a murine model of type 2 diabetes. *J Endocrinol* 216(1):1-11.

- [73] Callaghan, B.C., Gallagher, G., Fridman, V., Feldman, E.L., 2020. Diabetic neuropathy: what does the future hold? *Diabetologia* 63(5):891-897.
- [74] Callaghan, B.C., Xia, R., Reynolds, E., Banerjee, M., Rothberg, A.E., Burant, C.F., et al., 2016. Association Between Metabolic Syndrome Components and Polyneuropathy in an Obese Population. *JAMA Neurol* 73(12):1468-1476.
- [75] McCall, K.D., Holliday, D., Dickerson, E., Wallace, B., Schwartz, A.L., Schwartz, C., et al., 2010. Phenylmethimazole blocks palmitate-mediated induction of inflammatory cytokine pathways in 3T3L1 adipocytes and RAW 264.7 macrophages. *J Endocrinol* 207(3):343-353.
- [76] O'Brien, P.D., Guo, K., Eid, S.A., Rumora, A.E., Hinder, L.M., Hayes, J.M., et al., 2020. Integrated lipidomic and transcriptomic analyses identify altered nerve triglycerides in mouse models of prediabetes and type 2 diabetes. *Dis Model Mech* 13(2).
- [77] Li, Y., Ge, M., Ciani, L., Kuriakose, G., Westover, E.J., Dura, M., et al., 2004. Enrichment of endoplasmic reticulum with cholesterol inhibits sarcoplasmic-endoplasmic reticulum calcium ATPase-2b activity in parallel with increased order of membrane lipids: implications for depletion of endoplasmic reticulum calcium stores and apoptosis in cholesterol-loaded macrophages. *J Biol Chem* 279(35):37030-37039.
- [78] Rumora, A.E., LoGrasso, G., Hayes, J.M., Mendelson, F.E., Tabbey, M.A., Haidar, J.A., et al., 2019. The Divergent Roles of Dietary Saturated and Monounsaturated Fatty Acids on Nerve Function in Murine Models of Obesity. *J Neurosci* 39(19):3770-3781.
- [79] Rumora, A.E., Lentz, S.I., Hinder, L.M., Jackson, S.W., Valesano, A., Levinson, G.E., et al., 2018. Dyslipidemia impairs

mitochondrial trafficking and function in sensory neurons. *FASEB J* 32(1):195-207.

[80] Wang, X., Winter, D., Ashrafi, G., Schlehe, J., Wong, Y.L., Selkoe, D., et al., 2011. PINK1 and Parkin target Miro for phosphorylation and degradation to arrest mitochondrial motility. *Cell* 147(4):893-906.

[81] Saotome, M., Safiulina, D., Szabadkai, G., Das, S., Fransson, A., Aspenstrom, P., et al., 2008. Bidirectional Ca<sup>2+</sup>-dependent control of mitochondrial dynamics by the Miro GTPase. *Proc Natl Acad Sci U S A* 105(52):20728-20733.

[82] Cai, Q., Sheng, Z.H., 2009. Moving or stopping mitochondria: Miro as a traffic cop by sensing calcium. *Neuron* 61(4):493-496.

[83] Padilla, A., Descorbeth, M., Almeyda, A.L., Payne, K., De Leon, M., 2011. Hyperglycemia magnifies Schwann cell dysfunction and cell death triggered by PA-induced lipotoxicity. *Brain Res* 1370:64-79.

[84] Sajic, M., Rumora, A.E., Kanhai, A.A., Dentoni, G., Varatharajah, S., Casey, C., et al., 2021. High Dietary Fat Consumption Impairs Axonal Mitochondrial Function. *J Neurosci* 41(19):4321-4334.

[85] Peng, G., Li, L., Liu, Y., Pu, J., Zhang, S., Yu, J., et al., 2011. Oleate blocks palmitate-induced abnormal lipid distribution, endoplasmic reticulum expansion and stress, and insulin resistance in skeletal muscle. *Endocrinology* 152(6):2206-2218.

[86] Salas-Salvadó, J., Bulló, M., Babio, N., Martínez-González, M., Ibarrola-Jurado, N., Basora, J., et al., 2011. Reduction in the incidence of type 2 diabetes with the Mediterranean diet: results of the PREDIMED-Reus nutrition intervention randomized trial. *Diabetes Care* 34(1):14-19.

- [87] Estruch, R., Ros, E., Salas-Salvadó, J., Covas, M.I., Corella, D., Arós, F., et al., 2018. Primary Prevention of Cardiovascular Disease with a Mediterranean Diet Supplemented with Extra-Virgin Olive Oil or Nuts. *N Engl J Med* 378(25):e34.
- [88] Sun, L., Ishida, T., Yasuda, T., Kojima, Y., Honjo, T., Yamamoto, Y., et al., 2009. RAGE mediates oxidized LDL-induced pro-inflammatory effects and atherosclerosis in non-diabetic LDL receptor-deficient mice. *Cardiovasc Res* 82(2):371-381.
- [89] Vincent, A.M., Hayes, J.M., McLean, L.L., Vivekanandan-Giri, A., Pennathur, S., Feldman, E.L., 2009. Dyslipidemia-induced neuropathy in mice: the role of oxLDL/LOX-1. *Diabetes* 58(10):2376-2385.
- [90] Nowicki, M., Müller, K., Serke, H., Kosacka, J., Vilser, C., Ricken, A., et al., 2010. Oxidized low-density lipoprotein (oxLDL)-induced cell death in dorsal root ganglion cell cultures depends not on the lectin-like oxLDL receptor-1 but on the toll-like receptor-4. *J Neurosci Res* 88(2):403-412.
- [91] Jang, E.R., Lee, C.S., 2011. 7-ketocholesterol induces apoptosis in differentiated PC12 cells via reactive oxygen species-dependent activation of NF- $\kappa$ B and Akt pathways. *Neurochem Int* 58(1):52-59.
- [92] Yu, S.B., Pekkurnaz, G., 2018. Mechanisms Orchestrating Mitochondrial Dynamics for Energy Homeostasis. *J Mol Biol* 430(21):3922-3941.
- [93] Ribeiro-da-Silva, A., Kenigsberg, R.L., Cuello, A.C., 1991. Light and electron microscopic distribution of nerve growth factor receptor-like immunoreactivity in the skin of the rat lower lip. *Neuroscience* 43(2-3):631-646.
- [94] Orfanos, C.E., Mahrle, G., 1973. Ultrastructure and cytochemistry of human cutaneous nerves. With special reference to

the ultrastructural localization of the specific and nonspecific cholinesterases in human skin. *J Invest Dermatol* 61(2):108-120.

[95] Sheng, Z.H., 2014. Mitochondrial trafficking and anchoring in neurons: New insight and implications. *J Cell Biol* 204(7):1087-1098.

[96] Tilokani, L., Nagashima, S., Paupe, V., Prudent, J., 2018. Mitochondrial dynamics: overview of molecular mechanisms. *Essays Biochem* 62(3):341-360.

[97] Kalichman, M.W., Powell, H.C., Mizisin, A.P., 1998. Reactive, degenerative, and proliferative Schwann cell responses in experimental galactose and human diabetic neuropathy. *Acta Neuropathol* 95(1):47-56.

[98] Mizisin, A.P., Nelson, R.W., Sturges, B.K., Vernau, K.M., Lecouteur, R.A., Williams, D.C., et al., 2007. Comparable myelinated nerve pathology in feline and human diabetes mellitus. *Acta Neuropathol* 113(4):431-442.

[99] Edwards, J.L., Quattrini, A., Lentz, S.I., Figueroa-Romero, C., Cerri, F., Backus, C., et al., 2010. Diabetes regulates mitochondrial biogenesis and fission in mouse neurons. *Diabetologia* 53(1):160-169.

[100] Schmidt, R.E., Green, K.G., Snipes, L.L., Feng, D., 2009. Neuritic dystrophy and neuronopathy in Akita (Ins2(Akita)) diabetic mouse sympathetic ganglia. *Exp Neurol* 216(1):207-218.

[101] Vincent, A.M., Edwards, J.L., McLean, L.L., Hong, Y., Cerri, F., Lopez, I., et al., 2010. Mitochondrial biogenesis and fission in axons in cell culture and animal models of diabetic neuropathy. *Acta Neuropathol* 120(4):477-489.

[102] Cnop, M., Foufelle, F., Velloso, L.A., 2012. Endoplasmic reticulum stress, obesity and diabetes. *Trends Mol Med* 18(1):59-68.

[103] Higa, A., Chevet, E., 2012. Redox signaling loops in the unfolded protein response. *Cell Signal* 24(8):1548-1555.

- [104] Sugimoto, K., Murakawa, Y., Sima, A.A., 2002. Expression and localization of insulin receptor in rat dorsal root ganglion and spinal cord. *J Peripher Nerv Syst* 7(1):44-53.
- [105] Craner, M.J., Klein, J.P., Black, J.A., Waxman, S.G., 2002. Preferential expression of IGF-I in small DRG neurons and down-regulation following injury. *Neuroreport* 13(13):1649-1652.
- [106] Cheng, H.L., Randolph, A., Yee, D., Delafontaine, P., Tennekoon, G., Feldman, E.L., 1996. Characterization of insulin-like growth factor-I and its receptor and binding proteins in transected nerves and cultured Schwann cells. *J Neurochem* 66(2):525-536.
- [107] Fernyhough, P., Willars, G.B., Lindsay, R.M., Tomlinson, D.R., 1993. Insulin and insulin-like growth factor I enhance regeneration in cultured adult rat sensory neurones. *Brain Res* 607(1-2):117-124.
- [108] Guo, G., Kan, M., Martinez, J.A., Zochodne, D.W., 2011. Local insulin and the rapid regrowth of diabetic epidermal axons. *Neurobiol Dis* 43(2):414-421.
- [109] Gao, W.Q., Shinsky, N., Ingle, G., Beck, K., Elias, K.A., Powell-Braxton, L., 1999. IGF-I deficient mice show reduced peripheral nerve conduction velocities and decreased axonal diameters and respond to exogenous IGF-I treatment. *J Neurobiol* 39(1):142-152.
- [110] Russell, J.W., Cheng, H.L., Golovoy, D., 2000. Insulin-like growth factor-I promotes myelination of peripheral sensory axons. *J Neuropathol Exp Neurol* 59(7):575-584.
- [111] Liang, G., Cline, G.W., Macica, C.M., 2007. IGF-1 stimulates de novo fatty acid biosynthesis by Schwann cells during myelination. *Glia* 55(6):632-641.
- [112] Homs, J., Pagès, G., Ariza, L., Casas, C., Chillón, M., Navarro, X., et al., 2014. Intrathecal administration of IGF-I by



AAVrh10 improves sensory and motor deficits in a mouse model of diabetic neuropathy. *Mol Ther Methods Clin Dev* 1:7.

[113] Kim, B., McLean, L.L., Philip, S.S., Feldman, E.L., 2011. Hyperinsulinemia induces insulin resistance in dorsal root ganglion neurons. *Endocrinology* 152(10):3638-3647.

[114] Grote, C.W., Groover, A.L., Ryals, J.M., Geiger, P.C., Feldman, E.L., Wright, D.E., 2013. Peripheral nervous system insulin resistance in ob/ob mice. *Acta Neuropathol Commun* 1:15.

[115] Wang, H., Storlien, L.H., Huang, X.F., 2002. Effects of dietary fat types on body fatness, leptin, and ARC leptin receptor, NPY, and AgRP mRNA expression. *Am J Physiol Endocrinol Metab* 282(6):E1352-1359.

[116] Coppey, L., Lu, B., Gerard, C., Yorek, M.A., 2012. Effect of Inhibition of Angiotensin-Converting Enzyme and/or Neutral Endopeptidase on Neuropathy in High-Fat-Fed C57Bl/6J Mice. *J Obes* 2012:326806.

[117] Coleman, D.L., 1978. Obese and diabetes: two mutant genes causing diabetes-obesity syndromes in mice. *Diabetologia* 14(3):141-148.

[118] Zhang, Y., Proenca, R., Maffei, M., Barone, M., Leopold, L., Friedman, J.M., 1994. Positional cloning of the mouse obese gene and its human homologue. *Nature* 372(6505):425-432.

[119] Halaas, J.L., Gajiwala, K.S., Maffei, M., Cohen, S.L., Chait, B.T., Rabinowitz, D., et al., 1995. Weight-reducing effects of the plasma protein encoded by the obese gene. *Science* 269(5223):543-546.

[120] Sullivan, K.A., Hayes, J.M., Wiggin, T.D., Backus, C., Su Oh, S., Lentz, S.I., et al., 2007. Mouse models of diabetic neuropathy. *Neurobiol Dis* 28(3):276-285.

- [121] Sima, A.A., Robertson, D.M., 1978. Peripheral neuropathy in mutant diabetic mouse [C57BL/Ks (db/db)]. *Acta Neuropathol* 41(2):85-89.
- [122] O'Brien, P.D., Sakowski, S.A., Feldman, E.L., 2014. Mouse models of diabetic neuropathy. *ILAR J* 54(3):259-272.
- [123] Kosacka, J., Woidt, K., Toyka, K.V., Paeschke, S., Klötting, N., Bechmann, I., et al., 2019. The role of dietary non-heme iron load and peripheral nerve inflammation in the development of peripheral neuropathy (PN) in obese non-diabetic leptin-deficient ob/ob mice. *Neurol Res* 41(4):341-353.
- [124] Ernst, A., Sharma, A.N., Elased, K.M., Guest, P.C., Rahmoune, H., Bahn, S., 2013. Diabetic db/db mice exhibit central nervous system and peripheral molecular alterations as seen in neurological disorders. *Transl Psychiatry* 3:e263.
- [125] Smith, A.G., Russell, J., Feldman, E.L., Goldstein, J., Peltier, A., Smith, S., et al., 2006. Lifestyle intervention for pre-diabetic neuropathy. *Diabetes Care* 29(6):1294-1299.
- [126] Kluding, P.M., Pasnoor, M., Singh, R., Jernigan, S., Farmer, K., Rucker, J., et al., 2012. The effect of exercise on neuropathic symptoms, nerve function, and cutaneous innervation in people with diabetic peripheral neuropathy. *J Diabetes Complications* 26(5):424-429.
- [127] Balducci, S., Iacobellis, G., Parisi, L., Di Biase, N., Calandriello, E., Leonetti, F., et al., 2006. Exercise training can modify the natural history of diabetic peripheral neuropathy. *J Diabetes Complications* 20(4):216-223.
- [128] Callaghan, B.C., Little, A.A., Feldman, E.L., Hughes, R.A., 2012. Enhanced glucose control for preventing and treating diabetic neuropathy. *Cochrane Database Syst Rev*(6):CD007543.

- [129] Miller, R.G., Orchard, T.J., 2020. Understanding Metabolic Memory: A Tale of Two Studies. *Diabetes* 69(3):291-299.
- [130] Navarro, X., Sutherland, D.E., Kennedy, W.R., 1997. Long-term effects of pancreatic transplantation on diabetic neuropathy. *Ann Neurol* 42(5):727-736.
- [131] Papanas, N., Ziegler, D., 2014. Efficacy of  $\alpha$ -lipoic acid in diabetic neuropathy. *Expert Opin Pharmacother* 15(18):2721-2731.
- [132] Stracke, H., Gaus, W., Achenbach, U., Federlin, K., Bretzel, R.G., 2008. Benfotiamine in diabetic polyneuropathy (BENDIP): results of a randomised, double blind, placebo-controlled clinical study. *Exp Clin Endocrinol Diabetes* 116(10):600-605.
- [133] Feldman, E.L., Callaghan, B.C., Pop-Busui, R., Zochodne, D.W., Wright, D.E., Bennett, D.L., et al., 2019. Diabetic neuropathy. *Nat Rev Dis Primers* 5(1):41.
- [134] High, K.A., Roncarolo, M.G., 2019. Gene Therapy. *N Engl J Med* 381(5):455-464.
- [135] Geoffroy, M.C., Salvetti, A., 2005. Helper functions required for wild type and recombinant adeno-associated virus growth. *Curr Gene Ther* 5(3):265-271.
- [136] Zengel, J., Carette, J.E., 2020. Structural and cellular biology of adeno-associated virus attachment and entry. *Adv Virus Res* 106:39-84.
- [137] Wagner, H.J., Weber, W., Fussenegger, M., 2021. Synthetic Biology: Emerging Concepts to Design and Advance Adeno-Associated Viral Vectors for Gene Therapy. *Adv Sci (Weinh)* 8(9):2004018.
- [138] Riyad, J.M., Weber, T., 2021. Intracellular trafficking of adeno-associated virus (AAV) vectors: challenges and future directions. *Gene Ther.*

- [139] Calcedo, R., Vandenberghe, L.H., Gao, G., Lin, J., Wilson, J.M., 2009. Worldwide epidemiology of neutralizing antibodies to adeno-associated viruses. *J Infect Dis* 199(3):381-390.
- [140] Wilson, J.M., Flotte, T.R., 2020. Moving Forward After Two Deaths in a Gene Therapy Trial of Myotubular Myopathy. *Hum Gene Ther* 31(13-14):695-696.
- [141] 2020. High-dose AAV gene therapy deaths. *Nat Biotechnol* 38(8):910.
- [142] Ronzitti, G., Gross, D.A., Mingozzi, F., 2020. Human Immune Responses to Adeno-Associated Virus (AAV) Vectors. *Front Immunol* 11:670.
- [143] Van Alstyne, M., Tattoli, I., Delestrée, N., Recinos, Y., Workman, E., Shihabuddin, L.S., et al., 2021. Gain of toxic function by long-term AAV9-mediated SMN overexpression in the sensorimotor circuit. *Nat Neurosci* 24(7):930-940.
- [144] Monteys, A.M., Hundley, A.A., Ranum, P.T., Tecedor, L., Muehlmann, A., Lim, E., et al., 2021. Regulated control of gene therapies by drug-induced splicing. *Nature* 596(7871):291-295.
- [145] Homs, J., Ariza, L., Pagès, G., Udina, E., Navarro, X., Chillón, M., et al., 2011. Schwann cell targeting via intrasciatic injection of AAV8 as gene therapy strategy for peripheral nerve regeneration. *Gene Ther* 18(6):622-630.
- [146] Glatzel, M., Flechsig, E., Navarro, B., Klein, M.A., Paterna, J.C., Büeler, H., et al., 2000. Adenoviral and adeno-associated viral transfer of genes to the peripheral nervous system. *Proc Natl Acad Sci U S A* 97(1):442-447.
- [147] Pleticha, J., Maus, T.P., Christner, J.A., Marsh, M.P., Lee, K.H., Hooten, W.M., et al., 2014. Minimally invasive convection-enhanced delivery of biologics into dorsal root ganglia: validation in

the pig model and prospective modeling in humans. Technical note. *J Neurosurg* 121(4):851-858.

[148] Sargiannidou, I., Kagiava, A., Kleopa, K.A., 2020. Gene therapy approaches targeting Schwann cells for demyelinating neuropathies. *Brain Res* 1728:146572.

[149] Yang, B., Li, S., Wang, H., Guo, Y., Gessler, D.J., Cao, C., et al., 2014. Global CNS transduction of adult mice by intravenously delivered rAAVrh.8 and rAAVrh.10 and nonhuman primates by rAAVrh.10. *Mol Ther* 22(7):1299-1309.

[150] Fu, H., Dirosario, J., Killedar, S., Zaraspe, K., McCarty, D.M., 2011. Correction of neurological disease of mucopolysaccharidosis IIIB in adult mice by rAAV9 trans-blood-brain barrier gene delivery. *Mol Ther* 19(6):1025-1033.

[151] Chan, K.Y., Jang, M.J., Yoo, B.B., Greenbaum, A., Ravi, N., Wu, W.L., et al., 2017. Engineered AAVs for efficient noninvasive gene delivery to the central and peripheral nervous systems. *Nat Neurosci* 20(8):1172-1179.

[152] Foust, K.D., Nurre, E., Montgomery, C.L., Hernandez, A., Chan, C.M., Kaspar, B.K., 2009. Intravascular AAV9 preferentially targets neonatal neurons and adult astrocytes. *Nat Biotechnol* 27(1):59-65.

[153] Gray, S.J., Matagne, V., Bachaboina, L., Yadav, S., Ojeda, S.R., Samulski, R.J., 2011. Preclinical differences of intravascular AAV9 delivery to neurons and glia: a comparative study of adult mice and nonhuman primates. *Mol Ther* 19(6):1058-1069.

[154] Schuster, D.J., Dykstra, J.A., Riedl, M.S., Kitto, K.F., Belur, L.R., Mclvor, R.S., et al., 2014. Biodistribution of adeno-associated virus serotype 9 (AAV9) vector after intrathecal and intravenous delivery in mouse. *Front Neuroanat* 8:42.

- [155] Gray, S.J., Nagabhushan Kalburgi, S., McCown, T.J., Jude Samulski, R., 2013. Global CNS gene delivery and evasion of anti-AAV-neutralizing antibodies by intrathecal AAV administration in non-human primates. *Gene Ther* 20(4):450-459.
- [156] Park, S.H., Eber, M.R., Tsuzuki, S., Booker, M.E., Sunil, A.G., Widner, D.B., et al., 2017. Adeno-associated virus serotype rh10 is a useful gene transfer vector for sensory nerves that innervate bone in immunodeficient mice. *Sci Rep* 7(1):17428.
- [157] Gong, Y., Berenson, A., Laheji, F., Gao, G., Wang, D., Ng, C., et al., 2019. Intrathecal Adeno-Associated Viral Vector-Mediated Gene Delivery for Adrenomyeloneuropathy. *Hum Gene Ther* 30(5):544-555.
- [158] Hordeaux, J., Hinderer, C., Buza, E.L., Louboutin, J.P., Jahan, T., Bell, P., et al., 2019. Safe and Sustained Expression of Human Iduronidase After Intrathecal Administration of Adeno-Associated Virus Serotype 9 in Infant Rhesus Monkeys. *Hum Gene Ther* 30(8):957-966.
- [159] Bey, K., Deniaud, J., Dubreil, L., Joussemet, B., Cristini, J., Ciron, C., et al., 2020. Intra-CSF AAV9 and AAVrh10 Administration in Nonhuman Primates: Promising Routes and Vectors for Which Neurological Diseases? *Mol Ther Methods Clin Dev* 17:771-784.
- [160] Theurl, M., Lener, D., Albrecht-Schgoer, K., Beer, A., Schgoer, W., Liu, Y., et al., 2018. Gene therapy with the angiogenic neuropeptide secretoneurin ameliorates experimental diabetic neuropathy. *FASEB J* 32(9):4815-4823.
- [161] Pradat, P.F., Kennel, P., Naimi-Sadaoui, S., Finiels, F., Orsini, C., Revah, F., et al., 2001. Continuous delivery of neurotrophin 3 by gene therapy has a neuroprotective effect in experimental models of diabetic and acrylamide neuropathies. *Hum Gene Ther* 12(18):2237-2249.

- [162] Walwyn, W.M., Matsuka, Y., Arai, D., Bloom, D.C., Lam, H., Tran, C., et al., 2006. HSV-1-mediated NGF delivery delays nociceptive deficits in a genetic model of diabetic neuropathy. *Exp Neurol* 198(1):260-270.
- [163] Kessler, J.A., Shaibani, A., Sang, C.N., Christiansen, M., Kudrow, D., Vinik, A., et al., 2021. Gene therapy for diabetic peripheral neuropathy: A randomized, placebo-controlled phase III study of VM202, a plasmid DNA encoding human hepatocyte growth factor. *Clin Transl Sci* 14(3):1176-1184.
- [164] Pande, M., Hur, J., Hong, Y., Backus, C., Hayes, J.M., Oh, S.S., et al., 2011. Transcriptional profiling of diabetic neuropathy in the BKS db/db mouse: a model of type 2 diabetes. *Diabetes* 60(7):1981-1989.
- [165] Hur, J., Sullivan, K.A., Pande, M., Hong, Y., Sima, A.A., Jagadish, H.V., et al., 2011. The identification of gene expression profiles associated with progression of human diabetic neuropathy. *Brain* 134(Pt 11):3222-3235.
- [166] Nie, L., Wu, G., Culley, D.E., Scholten, J.C., Zhang, W., 2007. Integrative analysis of transcriptomic and proteomic data: challenges, solutions and applications. *Crit Rev Biotechnol* 27(2):63-75.
- [167] Fan, B., Liu, X.S., Szalad, A., Wang, L., Zhang, R., Chopp, M., et al., 2018. Influence of Sex on Cognition and Peripheral Neurovascular Function in Diabetic Mice. *Front Neurosci* 12:795.
- [168] Kennedy, W.R., Sakuta, M., Quick, D.C., 1984. Rodent eccrine sweat glands: a case of multiple efferent innervation. *Neuroscience* 11(3):741-749.
- [169] Huang, d.W., Sherman, B.T., Lempicki, R.A., 2009. Systematic and integrative analysis of large gene lists using DAVID bioinformatics resources. *Nat Protoc* 4(1):44-57.

- [170] Jo, S.H., Son, M.K., Koh, H.J., Lee, S.M., Song, I.H., Kim, Y.O., et al., 2001. Control of mitochondrial redox balance and cellular defense against oxidative damage by mitochondrial NADP<sup>+</sup>-dependent isocitrate dehydrogenase. *J Biol Chem* 276(19):16168-16176.
- [171] Gabay, C., Kushner, I., 1999. Acute-phase proteins and other systemic responses to inflammation. *N Engl J Med* 340(6):448-454.
- [172] Schlattner, U., Tokarska-Schlattner, M., Wallimann, T., 2006. Mitochondrial creatine kinase in human health and disease. *Biochim Biophys Acta* 1762(2):164-180.
- [173] Maxson, M.E., Grinstein, S., 2014. The vacuolar-type H<sup>+</sup>-ATPase at a glance - more than a proton pump. *J Cell Sci* 127(Pt 23):4987-4993.
- [174] Zhou, Y., Rui, L., 2010. Major urinary protein regulation of chemical communication and nutrient metabolism. *Vitam Horm* 83:151-163.
- [175] Hocheleid, T., Berger, F.G., Baumann, H., Libert, C., 2003. Alpha(1)-acid glycoprotein: an acute phase protein with inflammatory and immunomodulating properties. *Cytokine Growth Factor Rev* 14(1):25-34.
- [176] de Jonge, R.R., van Schaik, I.N., Vreijling, J.P., Troost, D., Baas, F., 2004. Expression of complement components in the peripheral nervous system. *Hum Mol Genet* 13(3):295-302.
- [177] Camborieux, L., Bertrand, N., Swerts, J.P., 1998. Changes in expression and localization of hemopexin and its transcripts in injured nervous system: a comparison of central and peripheral tissues. *Neuroscience* 82(4):1039-1052.
- [178] Lee, Y.S., Choi, J.W., Hwang, I., Lee, J.W., Lee, J.H., Kim, A.Y., et al., 2010. Adipocytokine orosomucoid integrates inflammatory and metabolic signals to preserve energy homeostasis



by resolving immoderate inflammation. *J Biol Chem* 285(29):22174-22185.

[179] Kuro-o, M., Matsumura, Y., Aizawa, H., Kawaguchi, H., Suga, T., Utsugi, T., et al., 1997. Mutation of the mouse *klotho* gene leads to a syndrome resembling ageing. *Nature* 390(6655):45-51.

[180] Massó, A., Sánchez, A., Gimenez-Llort, L., Lizcano, J.M., Cañete, M., García, B., et al., 2015. Secreted and Transmembrane  $\alpha$ Klotho Isoforms Have Different Spatio-Temporal Profiles in the Brain during Aging and Alzheimer's Disease Progression. *PLoS One* 10(11):e0143623.

[181] Kurosu, H., Yamamoto, M., Clark, J.D., Pastor, J.V., Nandi, A., Gurnani, P., et al., 2005. Suppression of aging in mice by the hormone Klotho. *Science* 309(5742):1829-1833.

[182] Yamamoto, M., Clark, J.D., Pastor, J.V., Gurnani, P., Nandi, A., Kurosu, H., et al., 2005. Regulation of oxidative stress by the anti-aging hormone *klotho*. *J Biol Chem* 280(45):38029-38034.

[183] Maltese, G., Psefteli, P.M., Rizzo, B., Srivastava, S., Gnudi, L., Mann, G.E., et al., 2017. The anti-ageing hormone *klotho* induces Nrf2-mediated antioxidant defences in human aortic smooth muscle cells. *J Cell Mol Med* 21(3):621-627.

[184] Ravikumar, P., Ye, J., Zhang, J., Pinch, S.N., Hu, M.C., Kuro-o, M., et al., 2014.  $\alpha$ -Klotho protects against oxidative damage in pulmonary epithelia. *Am J Physiol Lung Cell Mol Physiol* 307(7):L566-575.

[185] Banerjee, S., Zhao, Y., Sarkar, P.S., Rosenblatt, K.P., Tilton, R.G., Choudhary, S., 2013. Klotho ameliorates chemically induced endoplasmic reticulum (ER) stress signaling. *Cell Physiol Biochem* 31(4-5):659-672.

[186] Chen, C.D., Sloane, J.A., Li, H., Aytan, N., Giannaris, E.L., Zeldich, E., et al., 2013. The antiaging protein Klotho enhances

oligodendrocyte maturation and myelination of the CNS. *J Neurosci* 33(5):1927-1939.

[187] Robertson, D.M., Sima, A.A., 1980. Diabetic neuropathy in the mutant mouse [C57BL/ks(db/db)]: a morphometric study. *Diabetes* 29(1):60-67.

[188] Campero, M., Ezquer, M., Ezquer, F., 2015. Nerve excitability and structural changes in myelinated axons from diabetic mice. *Exp Clin Endocrinol Diabetes* 123(8):485-491.

[189] Liu, Y., Sebastian, B., Liu, B., Zhang, Y., Fissel, J.A., Pan, B., et al., 2017. Sensory and autonomic function and structure in footpads of a diabetic mouse model. *Sci Rep* 7:41401.

[190] Dalbøge, L.S., Almholt, D.L., Neerup, T.S., Vassiliadis, E., Vrang, N., Pedersen, L., et al., 2013. Characterisation of age-dependent beta cell dynamics in the male db/db mice. *PLoS One* 8(12):e82813.

[191] Sataranatarajan, K., Ikeno, Y., Bokov, A., Feliars, D., Yalamanchili, H., Lee, H.J., et al., 2016. Rapamycin Increases Mortality in db/db Mice, a Mouse Model of Type 2 Diabetes. *J Gerontol A Biol Sci Med Sci* 71(7):850-857.

[192] Junien, J.L., Chomette, G., Guillaume, M., Wajcman, H., Sterne, J., 1981. [Effect of long-term metformin treatment on the development of diabetes in genetically diabetic mice (DBM) (author's transl)]. *Diabete Metab* 7(4):251-258.

[193] Maessen, D.E., Stehouwer, C.D., Schalkwijk, C.G., 2015. The role of methylglyoxal and the glyoxalase system in diabetes and other age-related diseases. *Clin Sci (Lond)* 128(12):839-861.

[194] Horáková, L., Strosova, M.K., Spickett, C.M., Blaskovic, D., 2013. Impairment of calcium ATPases by high glucose and potential pharmacological protection. *Free Radic Res* 47 Suppl 1:81-92.

- [195] Egnatchik, R.A., Leamy, A.K., Jacobson, D.A., Shiota, M., Young, J.D., 2014. ER calcium release promotes mitochondrial dysfunction and hepatic cell lipotoxicity in response to palmitate overload. *Mol Metab* 3(5):544-553.
- [196] Lupachyk, S., Watcho, P., Obrosova, A.A., Stavniichuk, R., Obrosova, I.G., 2013. Endoplasmic reticulum stress contributes to prediabetic peripheral neuropathy. *Exp Neurol* 247:342-348.
- [197] Gardner, P.R., Fridovich, I., 1992. Inactivation-reeactivation of aconitase in *Escherichia coli*. A sensitive measure of superoxide radical. *J Biol Chem* 267(13):8757-8763.
- [198] Tretter, L., Adam-Vizi, V., 2000. Inhibition of Krebs cycle enzymes by hydrogen peroxide: A key role of [alpha]-ketoglutarate dehydrogenase in limiting NADH production under oxidative stress. *J Neurosci* 20(24):8972-8979.
- [199] Brand, M.D., Pakay, J.L., Ocloo, A., Kokoszka, J., Wallace, D.C., Brookes, P.S., et al., 2005. The basal proton conductance of mitochondria depends on adenine nucleotide translocase content. *Biochem J* 392(Pt 2):353-362.
- [200] Cadenas, S., 2018. Mitochondrial uncoupling, ROS generation and cardioprotection. *Biochim Biophys Acta Bioenerg* 1859(9):940-950.
- [201] Lu, H., Yang, Y., Allister, E.M., Wijesekara, N., Wheeler, M.B., 2008. The identification of potential factors associated with the development of type 2 diabetes: a quantitative proteomics approach. *Mol Cell Proteomics* 7(8):1434-1451.
- [202] Sas, K.M., Kayampilly, P., Byun, J., Nair, V., Hinder, L.M., Hur, J., et al., 2016. Tissue-specific metabolic reprogramming drives nutrient flux in diabetic complications. *JCI Insight* 1(15):e86976.

- [203] Ashford, A.J., Pain, V.M., 1986. Effect of diabetes on the rates of synthesis and degradation of ribosomes in rat muscle and liver in vivo. *J Biol Chem* 261(9):4059-4065.
- [204] Miller, M., Bower, E., Levitt, P., Li, D., Chantler, P.D., 1992. Myosin II distribution in neurons is consistent with a role in growth cone motility but not synaptic vesicle mobilization. *Neuron* 8(1):25-44.
- [205] Roisen, F.J., Wilson, F.J., Yorke, G., Inczedy-Marcsek, M., Hirabayashi, T., 1983. Immunohistochemical localization of troponin-C in cultured neurons. *J Muscle Res Cell Motil* 4(2):163-175.
- [206] Komori, N., Takemori, N., Kim, H.K., Singh, A., Hwang, S.H., Foreman, R.D., et al., 2007. Proteomics study of neuropathic and nonneuropathic dorsal root ganglia: altered protein regulation following segmental spinal nerve ligation injury. *Physiol Genomics* 29(2):215-230.
- [207] Zhao, X., Song, S., Sun, G., Strong, R., Zhang, J., Grotta, J.C., et al., 2009. Neuroprotective role of haptoglobin after intracerebral hemorrhage. *J Neurosci* 29(50):15819-15827.
- [208] McMillan, D.E., 1989. Increased levels of acute-phase serum proteins in diabetes. *Metabolism* 38(11):1042-1046.
- [209] Hur, J., Dauch, J.R., Hinder, L.M., Hayes, J.M., Backus, C., Pennathur, S., et al., 2015. The Metabolic Syndrome and Microvascular Complications in a Murine Model of Type 2 Diabetes. *Diabetes* 64(9):3294-3304.
- [210] Rosoklija, G.B., Dwork, A.J., Younger, D.S., Karlikaya, G., Latov, N., Hays, A.P., 2000. Local activation of the complement system in endoneurial microvessels of diabetic neuropathy. *Acta Neuropathol* 99(1):55-62.

- [211] Lim, S.Y., Raftery, M.J., Goyette, J., Hsu, K., Geczy, C.L., 2009. Oxidative modifications of S100 proteins: functional regulation by redox. *J Leukoc Biol* 86(3):577-587.
- [212] Vogl, T., Tenbrock, K., Ludwig, S., Leukert, N., Ehrhardt, C., van Zoelen, M.A., et al., 2007. Mrp8 and Mrp14 are endogenous activators of Toll-like receptor 4, promoting lethal, endotoxin-induced shock. *Nat Med* 13(9):1042-1049.
- [213] Leclerc, E., Fritz, G., Vetter, S.W., Heizmann, C.W., 2009. Binding of S100 proteins to RAGE: an update. *Biochim Biophys Acta* 1793(6):993-1007.
- [214] Jin, Y., Sharma, A., Carey, C., Hopkins, D., Wang, X., Robertson, D.G., et al., 2013. The expression of inflammatory genes is upregulated in peripheral blood of patients with type 1 diabetes. *Diabetes Care* 36(9):2794-2802.
- [215] Hui, X., Zhu, W., Wang, Y., Lam, K.S., Zhang, J., Wu, D., et al., 2009. Major urinary protein-1 increases energy expenditure and improves glucose intolerance through enhancing mitochondrial function in skeletal muscle of diabetic mice. *J Biol Chem* 284(21):14050-14057.
- [216] Zhou, Y., Jiang, L., Rui, L., 2009. Identification of MUP1 as a regulator for glucose and lipid metabolism in mice. *J Biol Chem* 284(17):11152-11159.
- [217] Baur, J.A., Pearson, K.J., Price, N.L., Jamieson, H.A., Lerin, C., Kalra, A., et al., 2006. Resveratrol improves health and survival of mice on a high-calorie diet. *Nature* 444(7117):337-342.
- [218] Kleinert, M., Parker, B.L., Jensen, T.E., Raun, S.H., Pham, P., Han, X., et al., 2018. Quantitative proteomic characterization of cellular pathways associated with altered insulin sensitivity in skeletal muscle following high-fat diet feeding and exercise training. *Sci Rep* 8(1):10723.

- [219] Charkoftaki, G., Wang, Y., McAndrews, M., Bruford, E.A., Thompson, D.C., Vasiliou, V., et al., 2019. Update on the human and mouse lipocalin (LCN) gene family, including evidence the mouse Mup cluster is result of an "evolutionary bloom". *Hum Genomics* 13(1):11.
- [220] Hinder, L.M., Murdock, B.J., Park, M., Bender, D.E., O'Brien, P.D., Rumora, A.E., et al., 2018. Transcriptional networks of progressive diabetic peripheral neuropathy in the db/db mouse model of type 2 diabetes: An inflammatory story. *Exp Neurol* 305:33-43.
- [221] McGregor, B.A., Eid, S., Rumora, A.E., Murdock, B., Guo, K., de Anda-Jáuregui, G., et al., 2018. Conserved Transcriptional Signatures in Human and Murine Diabetic Peripheral Neuropathy. *Sci Rep* 8(1):17678.
- [222] Rojas, D.R., Kuner, R., Agarwal, N., 2019. Metabolomic signature of type 1 diabetes-induced sensory loss and nerve damage in diabetic neuropathy. *J Mol Med (Berl)* 97(6):845-854.
- [223] Sahu, A., Mamiya, H., Shinde, S.N., Cheikhi, A., Winter, L.L., Vo, N.V., et al., 2018. Age-related declines in  $\alpha$ -Klotho drive progenitor cell mitochondrial dysfunction and impaired muscle regeneration. *Nat Commun* 9(1):4859.
- [224] Cashman, N.R., Durham, H.D., Blusztajn, J.K., Oda, K., Tabira, T., Shaw, I.T., et al., 1992. Neuroblastoma x spinal cord (NSC) hybrid cell lines resemble developing motor neurons. *Dev Dyn* 194(3):209-221.
- [225] Doran, C., Chetrit, J., Holley, M.C., Grundy, D., Nassar, M.A., 2015. Mouse DRG Cell Line with Properties of Nociceptors. *PLoS One* 10(6):e0128670.

- [226] Wood, J.N., Bevan, S.J., Coote, P.R., Dunn, P.M., Harmar, A., Hogan, P., et al., 1990. Novel cell lines display properties of nociceptive sensory neurons. *Proc Biol Sci* 241(1302):187-194.
- [227] Piedra, J., Ontiveros, M., Miravet, S., Penalva, C., Monfar, M., Chillón, M., 2015. Development of a rapid, robust, and universal picogreen-based method to titer adeno-associated vectors. *Hum Gene Ther Methods* 26(1):35-42.
- [228] Niwa, H., Yamamura, K., Miyazaki, J., 1991. Efficient selection for high-expression transfectants with a novel eukaryotic vector. *Gene* 108(2):193-199.
- [229] Miyazaki, J., Takaki, S., Araki, K., Tashiro, F., Tominaga, A., Takatsu, K., et al., 1989. Expression vector system based on the chicken beta-actin promoter directs efficient production of interleukin-5. *Gene* 79(2):269-277.
- [230] Yuan, J., Wang, X., Zhang, Y., Hu, X., Fei, J., Li, N., 2006. Mammalian Pol III promoter H1 can transcribe shRNA inducing RNAi in chicken cells. *Mol Biol Rep* 33(1):33-41.
- [231] Loeb, J.E., Cordier, W.S., Harris, M.E., Weitzman, M.D., Hope, T.J., 1999. Enhanced expression of transgenes from adeno-associated virus vectors with the woodchuck hepatitis virus posttranscriptional regulatory element: implications for gene therapy. *Hum Gene Ther* 10(14):2295-2305.
- [232] Raghavan, M., Fee, D., Barkhaus, P.E., 2019. Generation and propagation of the action potential. *Handb Clin Neurol* 160:3-22.
- [233] Homs, J., Ariza, L., Pagès, G., Verdú, E., Casals, L., Udina, E., et al., 2011. Comparative study of peripheral neuropathy and nerve regeneration in NOD and ICR diabetic mice. *J Peripher Nerv Syst* 16(3):213-227.

- [234] Vilches, J.J., Navarro, X., Verdú, E., 1995. Functional sudomotor responses to cholinergic agonists and antagonists in the mouse. *J Auton Nerv Syst* 55(1-2):105-111.
- [235] Kennedy, W.R., Sakuta, M., 1984. Collateral reinnervation of sweat glands. *Ann Neurol* 15(1):73-78.
- [236] Kennedy, W.R., Sakuta, M., Sutherland, D., Goetz, F.C., 1984. Quantitation of the sweating deficiency in diabetes mellitus. *Ann Neurol* 15(5):482-488.
- [237] Vilches, J.J., Ceballos, D., Verdú, E., Navarro, X., 2002. Changes in mouse sudomotor function and sweat gland innervation with ageing. *Auton Neurosci* 95(1-2):80-87.
- [238] Vilches, J.J., Wynick, D., Kofler, B., Lang, R., Navarro, X., 2012. Sudomotor function and sweat gland innervation in galanin knockout mice. *Neuropeptides* 46(4):151-155.
- [239] Wiśniewski, J.R., Zougman, A., Nagaraj, N., Mann, M., 2009. Universal sample preparation method for proteome analysis. *Nat Methods* 6(5):359-362.
- [240] Liao, Y., Wang, J., Jaehnig, E.J., Shi, Z., Zhang, B., 2019. WebGestalt 2019: gene set analysis toolkit with revamped UIs and APIs. *Nucleic Acids Res* 47(W1):W199-W205.
- [241] Szklarczyk, D., Gable, A.L., Lyon, D., Junge, A., Wyder, S., Huerta-Cepas, J., et al., 2019. STRING v11: protein-protein association networks with increased coverage, supporting functional discovery in genome-wide experimental datasets. *Nucleic Acids Res* 47(D1):D607-D613.
- [242] Pfaffl, M.W., 2001. A new mathematical model for relative quantification in real-time RT-PCR. *Nucleic Acids Res* 29(9):e45.
- [243] Polpitiya, A.D., Qian, W.J., Jaitly, N., Petyuk, V.A., Adkins, J.N., Camp, D.G., et al., 2008. DAnTE: a statistical tool for



quantitative analysis of -omics data. *Bioinformatics* 24(13):1556-1558.

Artistic figures in this thesis have been created or adapted using BioRender. Adapted pre-made templates (Insulin production pathway, Insulin pathway, Organization of the sympathetic and parasympathetic nervous system, Electron transport chain, UPR Signaling (ATF6, PERK, IRE1), Adeno-associated virus (AAV) genome and AAV vector infection, 2021) have been retrieved from <https://app.biorender.com/biorender-templates>.

***ANNEX***



**Annexed table 1.** List of differentially expressed proteins (p-value < 0.05) in DRG from *db/db* compared to lean mice obtain by TMT-LC/MS/MS. Proteins with a fold change ratio above 1.2 and below 0.8 are highlighted in red and green, respectively.

Protein ID	Gene name	Ratio	P-value	Protein ID	Gene name	Ratio	P-value
B2RY26	Myh7	6,23	1,5E-04	Q61838	Pzp	1,23	4,3E-17
Q61646	Hp	2,23	1,7E-09	P08551	Nefl	1,22	7,0E-71
A2A6J2	Tnnt3	2,22	2,8E-02	F6ZTG3	Glod4	1,21	7,7E-07
Q5SX39	Myh4	2,13	1,5E-15	Q60675	Lama2	1,21	3,7E-04
P05977	Myl1	1,95	1,3E-10	Q8CAZ9	Prelp	1,21	2,4E-14
P11404	Fabp3	1,94	6,9E-14	Q92111	Trf	1,21	4,2E-67
P58774	Tpm2	1,91	2,0E-02	F8VQJ3	Lamc1	1,21	1,4E-03
A0A075B5P3	Ighg2b	1,84	8,4E-10	Q99KC8	Vva5a	1,21	3,4E-11
P01837	Igkc	1,79	1,7E-05	P68368	Tuba4a	1,21	1,4E-12
P58771	Tpm1	1,71	1,7E-07	P60202-2	Plp1	1,21	9,6E-03
P01027	C3	1,68	2,0E-66	D3YWF6	Otub1	1,20	4,7E-04
P97457	Mylpf	1,68	1,2E-05	P19246	Nefh	1,20	6,2E-27
Q8R429	Atp2a1	1,67	1,2E-02	F7BNZ5	Bcas1	1,20	2,5E-03
A0A0R4J1N1	Itih4	1,64	4,8E-03	O55103-2	Prx	1,20	6,3E-03
Q91X72	Hpx	1,63	2,0E-43	P62806	Hist1h4a	1,20	2,3E-34
Q8VCM7	Fgg	1,55	1,9E-03	D3YYN7	Atp1a2	1,19	3,4E-05
Q61613	Orm1	1,52	1,8E-02	Q05816	Fabp5	1,19	2,4E-03
P97315	Csrp1	1,45	1,6E-04	A1L0U3	Hist1h3e	1,19	3,9E-03
F6XC15	Flna	1,41	2,7E-02	Q99JY0	Hadhb	1,19	1,3E-02
Q60784	Fbn1	1,41	1,3E-02	P10493	Nid1	1,19	3,4E-07
P68134	Acta1	1,39	2,2E-07	P63054	Pcp4	1,19	3,5E-02
P04117	Fabp4	1,38	4,4E-08	Q80TB8	Vat1l	1,19	8,4E-10
A0A1L1STN8	Tagln	1,37	3,4E-03	E9QK82	Mpz	1,19	1,9E-29
E9PV63	Gstm5	1,37	2,1E-04	P97447	Fhl1	1,19	8,1E-03
O08677-2	Kng1	1,37	3,6E-33	P68372	Tubb4b	1,18	3,9E-02
P54071	ldh4	1,35	4,4E-08	Q9D6F9	Tubb4a	1,18	1,7E-04
P06728	Apoa4	1,35	9,4E-03	Q8BGR9-2	Ublcp1	1,18	3,9E-02
Q6NXH9	Krt73	1,34	1,9E-02	Q8VDN2	Atp1a1	1,18	1,5E-07
P31725	S100a9	1,34	9,7E-06	P18760	Cfl1	1,18	2,1E-31
Q62426	Cstb	1,34	5,1E-05	B0R1E3	Hint1	1,17	4,3E-05
P10649	Gstm1	1,32	3,3E-06	Q3KQ4	Serpina1a	1,17	3,7E-02
P23927	Cryab	1,32	9,2E-04	A0A0R4J036	Nefm	1,17	3,5E-29
P16330	Cnp	1,32	1,0E-60	P16015	Ca3	1,17	2,9E-15
P27005	S100a8	1,32	2,5E-03	Q9R0P5	Dstn	1,17	3,3E-05
E9QQ57	Prx	1,31	7,3E-27	A0A0A6YW07	Impa1	1,17	2,1E-02
Q04857	Col6a1	1,30	8,4E-04	Q62000	Ogn	1,16	4,1E-06
Q8R2X0	Ehd2	1,30	2,8E-02	Q3TFQ8	Pygb	1,16	1,3E-17
Q9DCT2	Ndufs3	1,30	3,4E-02	Q9ERD7	Tubb3	1,16	3,0E-12
Q05AA6	Drp2	1,30	1,5E-03	P58389	Ptpa	1,16	3,7E-02
P24472	Gsta4	1,29	2,1E-07	P62962	Pfn1	1,16	1,5E-08
P20065-2	Tmsb4x	1,29	1,5E-03	K9JA74	Gstp2	1,16	8,5E-06
A0A087WS16	Col6a3	1,28	9,2E-08	P13634	Car1	1,15	7,1E-04
Q3TWW0	Vim	1,26	1,1E-02	Q64727	Vcl	1,15	2,9E-07
P14069	S100a6	1,25	8,4E-10	D3Z0E6	Bpnt1	1,15	1,9E-02
Q05CE2	Synm	1,25	2,0E-03	P50543	S100a11	1,15	2,9E-03
P46660	Ina	1,25	1,8E-02	P17742	Ppia	1,15	2,3E-39
Q922W7	Myl12a	1,25	4,5E-03	D9IF74		1,15	8,0E-04
P99024	Tubb5	1,25	5,5E-09	Q9WVA4	Tagln2	1,14	5,7E-05
B8JJ84	Stxbp6	1,25	3,1E-02	A0A1W2P6G5	Myl6	1,14	1,0E-06
Q8R3P0	Aspa	1,24	7,2E-03	G3X9T8	Cp	1,14	2,2E-04
B7STB7	Anxa1	1,24	1,3E-03	Q6PIC6	Atp1a3	1,14	3,3E-02
P00493	Hprt1	1,24	7,8E-04	P63028	Tpt1	1,13	1,3E-03
Q7TMM9	Tubb2a	1,24	1,2E-19	Q9DBJ1	Pgam1	1,13	4,1E-04
P26039	Tln1	1,24	5,3E-09	Q3ZB60	Mag	1,13	1,1E-02
Q02788	Col6a2	1,24	1,2E-02	P08228	Sod1	1,13	8,4E-10
O54724	Cavin1	1,23	5,7E-05	Q8BP47	Nars	1,13	2,2E-02

Protein ID	Gene name	Ratio	P-value	Protein ID	Gene name	Ratio	P-value
Q3TJX0	Lcp1	1,13	1,2E-02	P50396	Gdi1	1,08	3,9E-03
Q6S388	Plec	1,13	2,8E-12	P50247	Ahcy	1,08	3,8E-03
Q3TN61	Rhoa	1,13	9,6E-03	P10922	H1f0	1,08	2,1E-02
P70296	Pebp1	1,13	9,1E-05	Q3UNN1	Sept7	1,07	1,3E-02
Q9JJV2-3	Pfn2	1,13	1,3E-02	E9Q616	Ahnak	1,07	8,4E-04
A0JLV3	Hist1h2bj	1,12	2,4E-18	P16546	Sptan1	1,07	1,2E-13
Q9CPU0	Glo1	1,12	3,4E-16	P14152	Mdh1	1,07	6,5E-08
Q00897	Serpina1d	1,12	7,0E-03	G3UX26	Vdac2	1,07	3,7E-02
P68369	Tuba1a	1,12	2,9E-30	P47754	Cappa2	1,07	3,9E-02
Q3U3L3	Serpinb6a	1,12	1,5E-07	G5E846	Prph	1,06	2,6E-07
Q5RJV4	Pgm2	1,12	1,9E-03	P61205	Arf3	1,06	2,6E-03
P29758	Oat	1,12	3,9E-02	Q61598-2	Gdi2	1,06	8,6E-03
P60335	Pcbp1	1,12	3,8E-02	P16125	Ldhd	1,06	3,4E-06
P17182	Eno1	1,12	2,3E-11	P99029-2	Prdx5	1,06	8,5E-04
A0A1W2P7Z3	Ube2n	1,12	9,5E-03	Q02053	Uba1	1,06	1,8E-02
P48678-2	Lmna	1,11	1,0E-06	Q04447	Ckb	1,05	3,4E-05
Q9Z1W9	Stk39	1,11	8,5E-04	P63101	Ywhaz	1,05	1,3E-03
D3Z0Y2	Prdx6	1,11	1,1E-05	P48036	Anxa5	0,97	1,5E-02
P07356	Anxa2	1,11	1,2E-13	P05064	Aldoa	0,96	1,3E-02
B2KF55	Ube2v2	1,11	4,9E-02	Q01853	Vcp	0,96	1,9E-03
E9Q3V6	Sept2	1,11	3,5E-02	P50114	S100b	0,95	2,8E-02
O55222	Ilk	1,11	3,9E-02	Q9JHU4	Dync1h1	0,95	2,9E-04
O88844	Idh1	1,11	9,7E-03	P20029	Grp78	0,95	2,8E-02
P40142	Tkt	1,11	1,5E-15	P68510	Ywhah	0,93	9,5E-03
B7ZWC0	Ndrp1	1,11	3,0E-03	P63325	Rps10	0,93	1,3E-02
C5H0E8	Rap1a	1,11	1,8E-09	P62631	Eef1a2	0,93	1,9E-05
Q8BMS1	Hadha	1,11	4,3E-05	F8WIR1	Ctsd	0,92	6,8E-04
A0AUV1	Hist1h2ah	1,10	1,6E-04	P63017	Hspa8	0,91	5,2E-33
P62897	Cyca	1,10	1,9E-02	Q9D6R2-2	Idh3a	0,91	3,5E-02
D3YX76	Gstm2	1,10	4,1E-02	Q3TGW8	Stt3	0,91	7,6E-03
A0A0G2JEU1	Aldh2	1,10	1,1E-02	A0A0G2JDJ5	Fdps	0,91	4,5E-02
P16045	Lgals1	1,10	5,2E-04	Q3TED3	Acly	0,91	1,9E-03
Q3UKH3	Acaa2	1,10	3,7E-02	P68254-2	Ywhaq	0,91	5,2E-05
Q3TE06	Wdr1	1,10	4,0E-02	P07724	Alb	0,91	8,9E-29
P20152	Vim	1,09	6,5E-03	P29699	Ahsg	0,91	4,4E-02
P60766	Cdc42	1,09	7,9E-03	P27773	Pdia3	0,91	2,9E-07
F7CVJ5	Ahnak2	1,09	1,2E-02	Q922Q8	Lrrc59	0,91	2,7E-02
Q8BTU5	Psm1	1,09	2,1E-02	P42669	Pura	0,90	4,2E-02
Q3TCL2	Akr1b3	1,09	2,1E-02	Q8CGC7	Eprs	0,90	2,4E-02
P17183	Eno2	1,09	1,4E-04	Q9DC49	Rps2	0,90	3,3E-02
Q9R0P9	Uchl1	1,09	1,2E-11	P51880	Fabp7	0,90	1,4E-02
O08553	Dpysl2	1,09	9,2E-11	P08113	Grp94	0,89	6,9E-06
P52480-2	Pkm	1,09	8,0E-29	P99027	Rplp2	0,89	8,1E-03
P26041	Msn	1,09	4,3E-04	P63038	Hspd1	0,89	2,2E-07
G3XA25	Acat2	1,09	1,1E-02	D3YVM5	Rplp0	0,89	3,4E-03
Q9Z0F7	Snca	1,09	8,8E-05	Q3UAZ3	Rars	0,89	4,4E-02
Q9Z140	Cpne6	1,09	9,9E-04	P07310	Ckm	0,88	5,3E-04
Q8VDD5	Myh9	1,09	4,7E-03	Q3U3D3	Vars	0,88	2,5E-02
A5JUZ1	Ubc	1,09	6,6E-03	P47963	Rpl13	0,88	9,0E-03
P14873	Map1b	1,08	1,5E-03	D3YUT3	Rps19	0,88	1,1E-04
Q9EQ06	Hsd17b11	1,08	3,9E-02	F7APP3	Nmt2	0,88	4,4E-02
P06745	Gpi1	1,08	1,0E-09	P14148	Rpl7	0,88	1,4E-03
Q3TT92	Dpysl3	1,08	5,1E-03	P68040	Rack1	0,88	2,2E-06
Q62261	Sptbn1	1,08	6,2E-11	Q3UWP8	Calr	0,88	1,5E-05
P08752	Gnai2	1,08	3,4E-02	P62908	Rps3	0,87	4,4E-08
P35700	Prdx1	1,08	3,4E-07	Q3TQP6	Me1	0,87	1,2E-02

Protein ID	Gene name	Ratio	P-value	Protein ID	Gene name	Ratio	P-value
P57722-2	Pcbp3	0,87	4,4E-02	Q00623	Apoa1	0,65	2,3E-31
Q9JJI8	Rpl38	0,87	4,6E-02	P04247	Mb	0,64	9,7E-38
P12970	Rpl7a	0,87	4,0E-02	Q91VB8	Hba-a2	0,64	4,7E-232
Q3THQ5	Stip1	0,86	1,8E-04	A0A0R4J011	Serpina3k	0,58	7,8E-80
Q64433	Hspe1	0,86	1,4E-02	Q00898	Serpina1e	0,55	6,5E-05
P14131	Rps16	0,86	3,6E-04	L7MUC7	Mup7	0,24	1,5E-20
Q8C7K6	Pcyox1l	0,86	4,4E-02				
P35564	Canx	0,86	2,2E-07				
Q497D7	Rpl30	0,86	3,0E-02				
Q6ZWZ6	Rps12	0,85	5,8E-05				
Q3TL58	Skp1a	0,85	3,7E-02				
P10630	Eif4a2	0,85	6,5E-03				
Q8BH80	Vapb	0,85	5,4E-10				
Q9D8N0	Eef1g	0,84	1,0E-14				
A0A1L1SQA8	Rps25	0,84	2,7E-04				
P28663	Napb	0,84	1,3E-03				
P00920	Car2	0,84	5,3E-07				
E9Q3T0	Gm10073	0,83	3,6E-03				
Q6ZQ38	Cand1	0,83	1,1E-04				
P51881	Slc25a5	0,83	3,7E-09				
Q9D8E6	Rpl4	0,83	2,6E-03				
Q545F8	Rps4x	0,82	1,6E-04				
P11499	Hsp90ab1	0,82	1,3E-14				
Q6PHZ1	Rpl17	0,82	4,5E-03				
O55142	Rpl35a	0,82	3,7E-02				
P62911	Rpl32	0,82	1,7E-02				
A0A0U1RNG0	Calca	0,82	1,0E-02				
P07901	Hsp90aa1	0,81	3,6E-19				
Q8ROM2	Ugp2	0,81	6,3E-04				
E0CXN5	Gpd1	0,81	2,0E-02				
Q3TDZ5	Tgfb1	0,80	3,8E-03				
Q3U931	G3bp2	0,80	1,1E-02				
P28650	Adssl1	0,80	1,8E-02				
F6SVV1	Gm9493	0,79	3,3E-02				
A0A0A6YXL3	Rpl31	0,79	4,7E-02				
Q54AH9	Hbb-b2	0,79	2,4E-25				
Q921R2	Rps13	0,79	4,4E-09				
P21550	Eno3	0,79	3,5E-09				
Q3U561	Rpl10a	0,79	2,1E-07				
O70569	rps14	0,79	1,0E-03				
Q9D1R9	Rpl34	0,78	3,3E-02				
G5E839	Cct4	0,77	1,2E-08				
Q99M71	Epdr1	0,77	6,0E-04				
A0A0R4J0X5	Serpina1c	0,76	2,9E-03				
O70250	Pgam2	0,76	9,1E-04				
Q9CSR6	Hsd17b12	0,76	8,9E-03				
O09167	Rpl21	0,75	5,1E-03				
P42703-2	Lifr	0,74	4,8E-03				
P19096	Fasn	0,74	1,0E-13				
P48962	Slc25a4	0,73	4,3E-25				
P62754	Rps6	0,73	4,2E-02				
D3YYM6	Rps5	0,70	7,3E-24				
Q8BQS5	Adipor2	0,69	1,8E-02				
A8DUK4	Hbb-bs	0,68	4,7E-142				
P28665	Mug1	0,67	1,1E-09				
A0A0A6YWP6	Atp6v1h	0,67	1,9E-03				

**Annexed table 2.** List of all differentially expressed proteins (p-value < 0.05) in SCN from *db/db* compared to lean mice obtain by TMT-LC/MS/MS. Proteins with a fold change ratio above 1.2 and below 0.8 are highlighted in red and green, respectively.

Protein ID	Gene name	Ratio	P-value	Protein ID	Gene name	Ratio	P-value
P07361	Orm2	4,30	3,3E-03	Q62165	Dag1	1,32	7,8E-15
Q9CYN2	Spcc2	2,42	7,0E-04	Q00612	G6pdx	1,32	1,2E-03
P01837	Igkc	1,89	2,2E-12	P68433	Hist1h3a	1,31	4,0E-03
P01867	Igh-3	1,89	3,0E-05	P14873	Map1b	1,31	8,8E-35
O88935	Syn1	1,85	6,1E-03	O88662	Emp2	1,31	7,4E-03
Q61646	Hp	1,81	7,5E-07	P08752	Gnai2	1,30	8,5E-03
P63054	Pcp4	1,79	4,1E-05	P02469	Lamb1	1,30	1,9E-09
P13634	Car1	1,77	2,8E-05	Q9WV92	Epb41f3	1,30	1,3E-18
P42125	Eci1	1,76	7,5E-03	P20917	Mag	1,30	1,0E-07
Q7TMM9	Tubb2a	1,74	9,1E-10	Q9Z0F7	Sncg	1,29	1,5E-20
Q9DB16	Cab39l	1,73	7,9E-03	P68369	Tuba1a	1,29	6,1E-33
P01863	Ighg	1,71	8,5E-06	P63213	Gng2	1,29	1,9E-04
Q9JKC6	Cend1	1,60	5,9E-08	Q9JLV1	Bag3	1,28	1,9E-06
P01027	C3	1,59	1,4E-24	Q9DBX3	Susd2	1,28	8,2E-10
P68368	Tuba4a	1,56	8,0E-41	P14094	Atp1b1	1,27	9,4E-14
P62082	Rps7	1,55	9,5E-04	P10922	H1f0	1,27	1,5E-13
Q6ZWY8	Tmsb10	1,53	1,6E-04	Q9JJV2	Pfn2	1,27	3,2E-06
P97427	Crmp1	1,52	2,8E-04	P23506	Pcmt1	1,27	2,2E-04
O35678	Mgll	1,52	3,3E-03	P11983	Tcp1	1,27	2,6E-03
Q60590	Orm1	1,51	6,4E-05	P15331	Prph	1,26	1,7E-47
P16330	Cnp	1,49	1,7E-116	P39053	Dnm1	1,26	1,7E-04
P01868	Ighg1	1,46	3,6E-02	Q9CPU0	Glo1	1,26	7,8E-23
A6X935	Itih4	1,44	8,5E-03	Q9JII6	Akr1a1	1,26	4,9E-04
P27573	Mpz	1,44	2,4E-308	O55042	Snca	1,26	1,9E-03
Q5U405	Tmprss13	1,42	4,6E-03	Q9R1Q8	Tagln3	1,26	4,8E-03
Q9CPV4	Glod4	1,42	2,6E-15	P62827	Ran	1,26	7,6E-05
Q9Z140	Cpne6	1,42	2,8E-14	Q9CQV6	Map1lc3b	1,26	4,1E-03
Q80YN3	Bcas1	1,41	6,7E-15	Q9R0P9	Uchl1	1,25	1,6E-32
Q9JKM7	Rab37	1,41	4,3E-02	P26638	Sars	1,25	1,4E-02
Q91X72	Hpx	1,41	4,7E-23	Q02053	Uba1	1,25	1,8E-09
P51642	Cntf	1,41	4,1E-04	P99024	Tubb5	1,25	1,2E-11
Q9EQF6	Dpysl5	1,40	2,3E-02	Q62188	Dpysl3	1,25	3,5E-13
Q99KC8	Vwa5a	1,40	7,7E-18	P01942	Hba-a1	1,25	2,3E-19
Q05816	Fabp5	1,38	8,4E-04	Q91VJ2	Cavin3	1,25	2,0E-03
Q9DBP5	Cmpk1	1,38	7,1E-03	Q61206	Pafah1b2	1,25	5,1E-07
P18760	Cfl1	1,36	1,2E-25	P50396	Gdi1	1,25	1,3E-07
P51910	Apod	1,36	2,0E-02	P99029	Prdx5	1,23	7,8E-23
P43274	Hist1h1e	1,36	9,3E-07	Q9ERD7	Tubb3	1,23	1,4E-08
P68372	Tubb4b	1,36	8,2E-04	Q61739	Itga6	1,23	4,1E-12
Q06138	Cab39	1,36	5,7E-04	P54227	Stmn1	1,23	1,8E-05
Q9Z130	Hnrnpdl	1,36	2,3E-03	P43277	Hist1h1d	1,23	3,0E-05
Q9JK54	Msgn1	1,35	6,2E-03	Q9D394	Rufy3	1,23	1,7E-03
Q70IV5	Synn	1,35	1,6E-07	Q8R3T5	Sbxp6	1,23	4,0E-03
P30275	Ckmt1	1,35	9,3E-03	Q6PIC6	Atp1a3	1,23	3,3E-03
P31725	S100a9	1,35	1,1E-02	Q6ZQ38	Cand1	1,22	3,6E-02
Q3UX10	Tubal3	1,35	3,6E-02	P02468	Lamc1	1,22	1,5E-22
P15864	Hist1h1c	1,34	4,2E-02	P10639	Txn1	1,22	9,0E-12
P24549	Aldh1a1	1,34	2,8E-07	P04117	Fabp4	1,22	6,6E-05
O55103	Prx	1,34	3,2E-153	Q62095	Ddx3y	1,22	1,3E-03
P11404	Fabp3	1,34	6,7E-03	O08599	Sbxp1	1,22	1,9E-05
P18242	Ctsd	1,34	9,5E-07	Q9CQI3	Gmfb	1,22	2,4E-04
P60202	Plp1	1,34	5,5E-03	Q8BH64	Ehd2	1,21	1,9E-03
Q9WTX5	Skp1a	1,33	1,4E-03	Q922F4	Tubb6	1,21	7,6E-03
Q8VDN2	Atp1a1	1,32	1,6E-10	Q62426	Cstb	1,21	4,2E-02
Q921C1	Gjc3	1,32	1,4E-02	P26041	Msn	1,21	9,1E-10
O88398	Avil	1,32	2,1E-02	Q99N28	Cadm3	1,21	2,2E-05

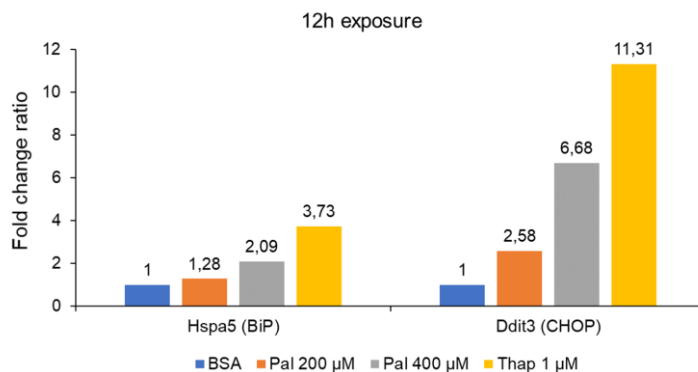
Protein ID	Gene name	Ratio	P-value	Protein ID	Gene name	Ratio	P-value
P09405	Ncl	1,20	8,5E-04	Q9D2M8	Ube2v2	1,13	3,3E-02
P14069	S100a6	1,20	4,4E-04	Q923T9	Camk2g	1,13	2,7E-02
O35206	Col15a1	1,20	2,4E-05	Q9DBG3	Ap2b1	1,13	5,4E-03
O08709	Prdx6	1,20	9,0E-12	P17183	Eno2	1,12	7,9E-04
Q8BHN3	Ganab	1,20	3,7E-02	P60766	Cdc42	1,12	4,3E-04
O08677	Kng1	1,20	3,2E-10	P61205	Arf3	1,12	4,7E-02
Q9QXS1	Plec	1,20	2,1E-33	Q01853	Vcp	1,12	1,0E-03
P63005	Pafah1b1	1,20	1,2E-02	P13020	Gsn	1,12	4,7E-05
P09813	Apoa2	1,20	1,2E-02	Q61207	Psap	1,12	3,9E-02
Q9QYR6	Map1a	1,19	2,5E-03	P40124	Cap1	1,12	1,2E-03
P56399	Usp5	1,19	2,1E-03	P14824	Anxa6	1,12	2,5E-16
Q60675	Lama2	1,19	2,4E-19	Q61147	Cp	1,12	6,4E-03
Q9QUH0	Glrx	1,19	1,7E-02	Q60930	Vdac2	1,12	2,4E-02
Q9R0Q7	Ptges3	1,19	3,3E-02	Q00897	Serpina1d	1,12	2,9E-08
Q8K0U4	Hspa12a	1,18	2,5E-07	P20444	Prkca	1,11	9,4E-03
Q8CI94	Pygb	1,18	2,2E-07	P08551	Nefl	1,11	8,2E-49
P23927	Cryab	1,18	1,7E-10	Q04447	Ckb	1,11	6,7E-07
Q8BWT1	Acaa2	1,18	1,1E-03	P19246	Nefh	1,11	1,5E-15
P10493	Nid1	1,18	4,8E-18	Q60854	Spi3	1,11	2,2E-06
Q9DBJ1	Pgam1	1,18	2,4E-04	Q92111	Trf	1,11	1,7E-15
P32261	Serpinc1	1,18	3,4E-03	P00920	Car2	1,10	1,1E-02
Q9D6F9	Tubb4a	1,18	9,1E-04	P63321	Rala	1,10	9,5E-03
P24472	Gsta4	1,18	5,5E-04	P58389	Ptpa	1,10	9,5E-03
Q07076	Anxa7	1,17	5,7E-03	P51150	Rab7	1,10	1,2E-02
P16546	Sptan1	1,17	2,2E-64	Q62261	Sptbn1	1,10	9,1E-11
P68510	Ywhah	1,17	1,8E-03	O54724	Cavin1	1,10	4,5E-03
Q9QU10	Rhoa	1,17	2,6E-06	P61979	Hnrnpk	1,10	3,2E-03
P08228	Sod1	1,17	9,4E-04	P63101	Ywhaz	1,10	1,0E-06
P63028	Tpt1	1,17	1,0E-02	Q61598	Gdi2	1,09	1,7E-02
Q91V12	Acot7	1,17	2,8E-09	O88844	Idh1	1,09	1,7E-03
P10637	Mapt	1,17	1,8E-03	Q60864	Stip1	1,09	3,0E-03
P70349	Hint1	1,17	2,6E-07	Q61171	Prdx2	1,09	5,3E-04
P34884	Mif	1,16	3,3E-03	Q62048	Pea15	1,09	2,4E-02
P04370	Mbp	1,16	2,2E-176	P14602	Hspb1	1,09	2,8E-04
Q91LJ2	Aldh9a1	1,16	2,7E-02	P62962	Pfn1	1,09	3,3E-03
P46460	Nsf	1,16	2,0E-02	Q05AA6	Drp2	1,08	2,9E-02
Q9WU78	Pdcc6ip	1,16	7,2E-03	P16045	Lgals1	1,08	7,8E-03
P0CG49	Ubb	1,16	2,4E-05	O08529	Capn2	1,08	1,5E-02
P17182	Eno1	1,16	9,1E-11	P27546	Map4	1,08	1,2E-03
P16125	Ldhb	1,16	2,5E-13	Q9CWS0	Ddah1	1,08	3,2E-02
Q62000	Ogn	1,16	2,4E-04	Q61838	Pzp	1,07	1,6E-02
Q8CGP6	Hist1h2ah	1,15	4,6E-03	P70168	Kpnb1	1,07	2,6E-02
A2A863	Itgb4	1,15	1,1E-04	P63001	Rac1	1,07	2,3E-02
P17742	Ppia	1,15	1,3E-16	O70318	Epb41l2	1,07	7,4E-04
P05202	Got2	1,15	4,3E-04	P35700	Prdx1	1,06	1,1E-04
P08553	Nefm	1,14	2,7E-47	P48036	Anxa5	1,06	3,1E-03
O08997	Atox1	1,14	2,7E-02	P63017	Hspa8	1,06	1,1E-03
O08553	Dpysl2	1,14	1,9E-07	Q9CRB6	Tppp3	1,05	8,5E-03
Q61553	Fscn1	1,14	1,5E-02	P14152	Mdh1	1,03	2,9E-02
Q80UW2	Fbxo2	1,14	7,2E-03	P02088	Hbb-b1	0,97	4,0E-02
Q7TQI3	Otub1	1,14	4,3E-04	P56480	Atp5b	0,97	3,3E-02
P50247	Ahcy	1,14	3,0E-05	P20152	Vim	0,96	3,5E-08
Q8BGY2	Eif5a2	1,14	6,4E-08	P0DP26	Calml1	0,94	1,5E-02
O55131	Sept7	1,13	3,2E-04	P24526	Pmp2	0,93	2,7E-02
P61982	Ywhag	1,13	1,3E-09	P09103	P4hb	0,93	1,9E-03
Q61292	Lamb2	1,13	1,4E-03	Q62425	Ndufa4	0,92	4,6E-02



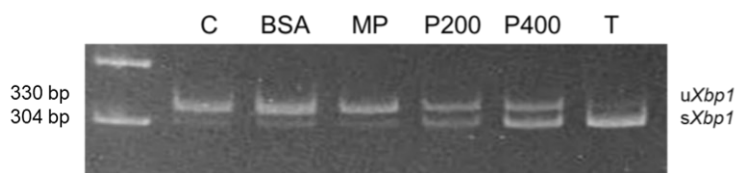
Protein ID	Gene name	Ratio	P-value	Protein ID	Gene name	Ratio	P-value
Q02788	Col6a2	0,91	6,4E-04	Q9QZJ6	Mfap5	0,68	1,6E-04
P60710	Actb	0,91	1,1E-02	P06801	Me1	0,68	3,3E-05
P27773	Pdia3	0,91	2,8E-03	P20801	Tnnc2	0,66	2,3E-02
P10126	Eef1a1	0,90	1,8E-04	Q91ZJ5	Ugp2	0,66	6,8E-03
P47738	Aldh2	0,90	1,9E-02	Q9WUB3	Pygm	0,66	3,5E-22
P08207	S100a10	0,90	1,4E-03	P58771	Tpm1	0,66	4,6E-05
P54071	Idh2	0,90	6,1E-03	P28665	Mug1	0,65	2,3E-35
P29699	Ahsg	0,89	2,1E-04	A2ASS6	Ttn	0,65	1,4E-02
P97315	Csrp1	0,89	2,3E-02	P16015	Ca3	0,63	2,7E-65
Q99K10	Aco2	0,89	2,0E-04	Q8R429	Atp2a1	0,63	1,8E-05
Q9CZ13	Uqcrc1	0,88	2,9E-02	Q5SX40	Myh1	0,62	1,9E-08
P20029	Grp78	0,88	1,8E-05	P13412	Tnni2	0,60	4,3E-04
P11499	Hsp90ab1	0,88	1,5E-03	P97457	Mylpf	0,56	6,0E-20
Q04857	Col6a1	0,87	3,5E-04	O08638	Myh11	0,55	5,6E-04
P47857	Pfkm	0,87	1,3E-03	O70250	Pgam2	0,54	6,7E-18
Q01768	Nme2	0,86	9,0E-03	P05977	Myl1	0,54	1,2E-25
P09411	Pgk1	0,86	2,7E-09	P58774	Tpm2	0,52	2,9E-05
Q35639	Anxa3	0,85	1,5E-02	Q5SX39	Myh4	0,51	1,4E-37
P45376	Aldr1	0,85	2,2E-11	P19096	Fasn	0,50	4,0E-44
P35762	Cd81	0,85	9,1E-03	Q9J191	Actn2	0,48	3,8E-02
Q6P5H2	Nes	0,85	1,4E-02	P04247	Mb	0,47	1,5E-26
P16858	Gapdh	0,85	6,5E-26	Q9QZ47	Tnnt3	0,47	6,6E-06
Q8OX19	Col14a1	0,84	1,4E-03	P21550	Eno3	0,46	9,2E-72
P51885	Lum	0,84	7,7E-27	P07759	Serpina3k	0,45	1,0E-121
P17751	Tpi1	0,83	1,5E-20	P32848	Pvalb	0,44	1,7E-11
Q9DCN2	Cyb5r3	0,83	4,1E-03	P68033	Actc1	0,40	1,0E-05
P20918	Plg	0,83	2,3E-02	P07310	Ckm	0,39	1,4E-169
Q9D0F9	Pgm1	0,82	7,0E-07	P37804	Tagln	0,36	6,1E-33
P28654	Dcn	0,82	8,5E-24	P68134	Acta1	0,34	6,4E-07
P06745	Gpi1	0,81	6,1E-13	Q91Z83	Myh7	0,34	1,7E-06
Q00623	Apoa1	0,81	4,3E-08	B5X0G2	Mup17	0,31	2,0E-07
P21107	Tpm3	0,80	4,6E-02	Q00898	Serpina1e	0,20	3,2E-13
P62301	Rps13	0,79	4,5E-03				
P19324	Serpinh1	0,79	4,0E-02				
Q60605	Myl6	0,79	2,7E-05				
P06151	Ldha	0,78	5,0E-11				
Q8BH61	F13a1	0,76	4,1E-05				
P82198	Tgfb1	0,76	6,9E-06				
Q8BTM8	Flna	0,76	4,2E-08				
Q8CGN5	Plin1	0,76	2,4E-02				
Q8VDQ8	Sirt2	0,76	2,3E-02				
Q5XKE0	Mybpc2	0,75	4,9E-02				
P07724	Alb	0,75	0,0E+00				
Q61554	Fbn1	0,74	1,6E-30				
Q9D8N0	Eef1g	0,73	3,2E-06				
P48962	Slc25a4	0,73	9,3E-04				
Q99MQ4	Aspn	0,73	4,4E-04				
Q9D2G2	Dlst	0,72	2,6E-03				
P05064	Aldoa	0,71	7,7E-55				
P55264	Adk	0,70	3,3E-03				
P13707	Gpd1	0,70	1,4E-08				
O88990	Actn3	0,70	1,7E-03				
P07758	Serpina1a	0,69	1,4E-28				
Q9R0Y5	Ak1	0,69	1,9E-08				
P15626	Gstm2	0,69	1,2E-03				
Q8VCT4	Ces1d	0,68	3,3E-03				

## IN VITRO PILOT STUDY OF UPR UPON PALMITATE EXPOSURE

### A ND7/23

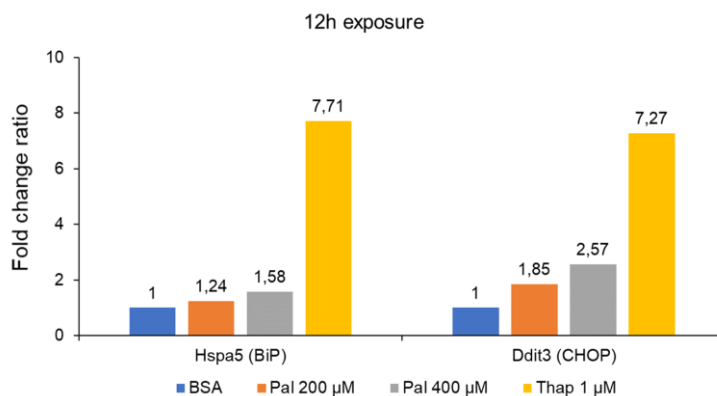


### B

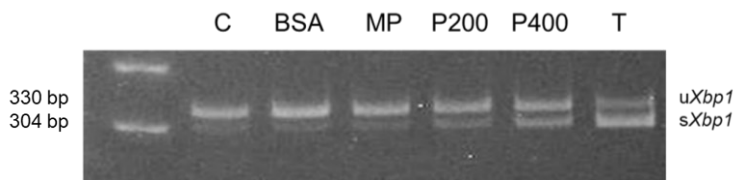


**Annexed figure 1.** Characterisation of unfolded protein response in ND7/23 cell line. **(A)** Quantification of *Hspa5* (BiP) and *Ddit3* (CHOP) expression by qPCR upon 200  $\mu$ M and 400  $\mu$ M palmitate exposure (12 hours). Thapsigargin 1  $\mu$ M was used as a positive control, and BSA as a negative control. Fold change ratio was normalised to BSA. **(B)** Analysis of *Xbp1* alternative splicing upon palmitate exposure (12 hours). Unfolded protein response triggers the switch from unspliced *Xbp1* (330 bp) towards spliced *Xbp1* (304 bp). Thapsigargin was used as a positive control, whereas BSA, along with culture medium (C) and methyl palmitate (MP), as negative controls.

## A NSC-34



## B



**Annexed figure 2.** Characterisation of unfolded protein response in NSC-34 cell line. **(A)** Quantification of *Hspa5* (BiP) and *Ddit3* (CHOP) expression by qPCR upon 200  $\mu$ M and 400  $\mu$ M palmitate exposure (12 hours). Thapsigargin 1  $\mu$ M was used as a positive control, and BSA as a negative control. Fold change ratio was normalised to BSA. **(B)** Analysis of *Xbp1* alternative splicing upon palmitate exposure (12 hours). Unfolded protein response triggers the switch from unspliced *Xbp1* (330 bp) towards spliced *Xbp1* (304 bp). Thapsigargin was used as a positive control, whereas BSA, along with culture medium (C) and methyl palmitate (MP), as negative controls.